UiT
THE ARCTIC
UNIVERSITY
OF NORWAY

Faculty of Science and Technology
Department of Geosciences

Evolution of a rock slope failure at Skredkallen, Vannøya

Martin Mikkelsen

GEO-3900 Master's thesis in Geology, November 2019

UNIVERSITY OF TROMSØ

Abstract

Rock slope failures are known major contributors to landscape evolution in alpine Norway, and also pose a threat to people and infrastructure in the present day. By examining the history of rock slope failures at active rockslide sites an understanding of recurrence intervals and triggering mechanisms can be achieved. The focus of this study is to form a complete picture of the evolution of an area of Vannøya, Troms, where an unstable slope sits above large failure deposits indicative of a sequenced failure history. The deformation of the URS, geomorphology of the area and geochronology of the deposits has been examined to provide a context and timing for the failure evolution of the slope and the larger area.

Skredkallen is a 1.1 Mm^3 actively deforming unstable rock slope (URS) located on the steep E-facing slope of Laukvikfjellet on Vannøya. Sitting at the base of the unstable slope is a c. 13 Mm^3 rock avalanche deposit, stretching to 1.4 km from the unstable area, and consisting of blocks ranging in size up to c. 1000 m^3. Morphostructural mapping suggests a biplanar compound slide (dominated by more than one sliding surface) formed by a step-path geometry between the gently-dipping foliation and steep joint sets. A prominent column (Kallen), controlled by orthogonal joints, formts the outer boundary of the URS and is toppling at c. $\leq$12 mm a^{-1} towards the E.

Deglaciation of the area occurred 15 – 13 ka, followed by isostatic rebound and relative sea-level changes, resulting in three prominent shorelines. The failure deposits are characterized by 3 domains (inner, middle and outer) by geometry and runout distance. The two outermost domains show evidence of marine erosion and deposition at elevations consistent with the Main and Tapes shorelines. ^{14}C dating of a lake sediments on top of the inner domain revealed an age of 1642 cal. yr BP.

These relative timing constraints suggest a rock avalanche or series of avalanches occurring between the formation of the marine limit and Main shoreline (deglaciation at 15-13 ka and Younger Dryas glacial advance at 11-10 ka). The age difference between the relative dating and the age of the sediments on top of the deposits suggests that one or multiple failures may have occurred following the emplacement of the main rock avalanche event, after which the (dated) lake formed.

Acknowledgements

This thesis is the end of a long era as a geology student at the University of Tromsø (UiT). I appreciate the opportunity to work on such an exciting site as Skredkaillen.

First of all, I would like to extend my sincere gratitude to my supervisor Louise Vick (UiT) for all guidance and feedback throughout this project. I really appreciate all the time and effort you have put in this project.

I would like to thank my co-supervisor Sofia Kjellman (UiT) for great feedback and help during lab- and fieldwork. I would also like to thank my co-supervisors Geoffrey Corner (UiT) and Steffen Bergh (UiT) for sharing their knowledge and for help fieldwork. I would also like to thank Lis Allaart (UiT) for kindly helping me during fieldwork.

I would like to thank co-student Leif Trønnes for great teamwork, valuable discussions and many laughs during fieldwork and in the office. Thanks to all fellow students at UiT for an unforgettable time in Tromsø. The highs, lows, smiles and laughs will never be forgotten.

Finally, I would like to thank my family for supporting me throughout my studies.

Tromsø, November 2019

Martin Mikkelsen

Table of Contents

Abbrevations

RSF	Rock slope failure
GIS	Geographical Information System
DEM	Digital elevation model
InSAR	Interferometric Synthetic Aperture Radar
ka	Thousand years
Ma	Million years
BP	Before present
LOS	Line of sight (InSAR)
ML	Marine limit
YD	Younger Dryas
LGM	Last Glacial Maximum
NGU	Geological Survey of Norway
URS	Unstable Rock Slope
WTBC	West Troms Basement Complex
VVFC	Vestfjorden Vannøya Fault Complex

1 Introduction

Paraglacial rock slope failure is a known major contributor to landscape evolution in alpine Norway (Blikra et al., 2006, Jarman, 2006). Rock slope failure has occurred throughout the Quaternary as a response to ice retreat (Ballantyne, 2002), seismic activity and climate (Blikra et al., 2006). Understanding the recurrence interval of rock slope failures is important to predict future events. Landslides from rock slope failure, as well as secondary hazards such as landslide-triggered displacement waves (fjord tsunamis), represent one of the most serious geohazards in Norway (Blikra et al., 2006). Understanding and characterizing rock slopes prior to catastrophic failure (Hermanns and Longva, 2012), and predicting the timing of future events, is vital to the reduction of risk to lives and infrastructure in Norway. Multiple landslide types and mechanisms are observed in Troms, where over 130 URS are mapped (NGU, 2019c). However, a complete inventory of URSs and pre-historic landslides is not yet available (Bunkholt et al., 2013b), and their evolution and timing is not well constrained (Hermanns and Longva, 2012).

1.1 Objective of the work

The intention of this project is to form a complete picture of the evolution of the unstable rock slope at Skredkallen on Vannøya, northern Norway. The main objective for this project is to define the geomorphology of the slope failure area, by examining both the structural elements of the active area and the geomorphology of the previous avalanche deposits.

The specific aims for this study are to:

- Provide a geomorphological overview of the area by means of historical, stereoscopic, orthographic, satellite and drone imagery, and field mapping;
- Provide a morpho-structural interpretation of the active area;
- Develop an interpretation of the evolution of the unstable area by examining the characteristics of the rock avalanche deposit(s).
- Provide insights into the timing of previous avalanche event(s) by dating lake sediments within the deposits; determine the number of events that may have occurred, determine the characteristics of the events including volume and runout.

1.2 Setting of the study area

The island of Vannøya is situated in the northern part of Troms County, Northern Norway (Figure 1 A + B). The island comprises a glacially formed landscape with steep mountain slopes, U-shaped valleys and deep fjords. The shoreline along the E part of the island is occur as a rim of low land surrounded by small islands and peninsulas, typically characterized as a "strandflat" (Reusch, 1894, Olesen et al., 2013). The unstable area Skredkallen is situated on a N-S-trending ridge located on the E side of the island (Figure 1 C). The ridge stretches from Vannvåg in the south to Slettnes in the north. The west-face of the mountain ridge display a gentle slope, with a relatively flat top. The E-facing slope of the ridge is significantly steeper, and close to vertical on the upper areas. Skredkallen is in the northern section of the ridge known as Laukvikfjellet, close to the village Slettnes. The unstable area lies on the E facing slope and covers approximately 200 m × 50 m at an elevation of between 270 and 470 m asl. Within the unstable area are multiple subsided terraces, cracks and three columns. Previous rock avalanches have resulted in a lobe-shaped body of deposits at the toe of the mountain. The body of deposits is locally named "Skrea" (Figure 2). The extent of these deposits are up to 1.4 km from the active area, and up to 500 m wide. The rock avalanche deposits are partly covered in vegetation. Surrounding the deposits is a mostly flat, boggy peat area and some sandy pits. The coastline is about 150 – 200 meters from the extent of the avalanche deposits with mostly sandy beaches.

The most recent rock avalanche occurred in the early 1950's, as reported by local residents. A large column of rock ("Kjærringa") collapsed as a result of the failure. The failure has been described by witnesses as "a cloud of sparks moving down the mountain side". Local residents ('Slettnes på Vannøya' facebook group, 2018, pers. comms.) have reported that in the past people were able to jump to a tall rock column known as "Kallen" (Figure 2). The grandmother of Signy Karlsen, Mathilde (b. 1880), was able to jump the distance as a child. Today the same distance would require a jump of at least 10 m.

The rockslide is still active today, as observed in satellite interferometry (InSAR; NGU, 2019a). Several cabins exist at the toe of the slope, which is a popular hiking area for local residents. The cabins are mostly unoccupied throughout the year. However, there is still a risk posed to people within them by future rock avalanche events from Skredkallen during popular hiking and camping periods.

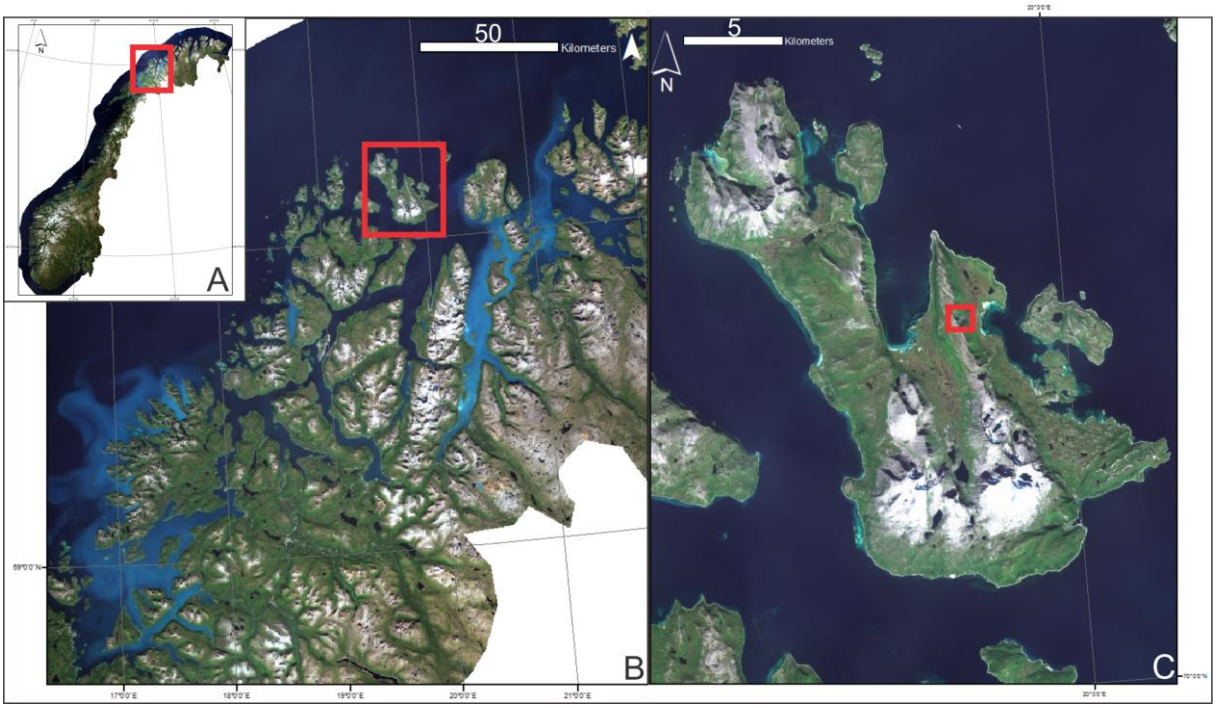

Figure 1: Location of the study area. A: Map of Norway with Troms County marked within the red square. B: A zoom-in of Troms County with Vannøya marked within the red square. C: Map of Vannøya with Skredkallen marked within the red square. Orthophotos obtained from Kartverket (2019).

Figure 2: Drone photograph from August 2018 giving an overview of the study area. The avalanche-dammed lakes and the column "Kallen" are marked with arrows, while the rock avalanche deposits ("Skrea") are marked within the black stippled line.

1.3 Previous work

Detailed studies of rock slope failures in Troms have been conducted for the last two decades, (e.g. Braathen et al., 2004, Blikra et al., 2006, Bunkholt et al., 2011, Bunkholt et al., 2012, Bunkholt et al., 2013a, Bunkholt et al., 2013b). A number of master projects have also been written about local geohazards (e.g. Husby, 2011, Rasmussen, 2011, Hannus, 2012, Eriksen, 2013, Skrede, 2013, Hernes, 2014, Bakkhaug, 2015, Nopper, 2015, Bredal, 2016, Bjørklid, 2017, Sandnes, 2017, Sikveland, 2019, Trønnes, 2019, Vik, 2019). The main objective for these projects has been correlation of field investigations of unstable rock slopes to the regional geology.

The bedrock geology of Vannøya was first described by Pettersen (1887), who stated that most of the island consists of Precambrian gneisses, overlain by Caledonian metasediments along the southern shores. Over 100 years later, the island was remapped by Binns et al. (1981) with a focus on the stratigraphy and depositional environment of the metasediments on the southern part of the island. They also stated that the Caledonian "schistose rocks" around Skipsfjord were actually highly sheared basement orthogneisses. More recent studies of the bedrock geology of Vannøya has been done by (Opheim and Andresen, 1989, Bergh et al., 2007, Bergh et al., 2010) with a focus on understanding the evolution of the WTBC.

Andersen (1968) made an interpretation of the Quarternary geology of Vannøya from aerial photographs. His interpretation was mainly based on correlating moraine ridges on Vannøya to Island 2 phase ridges in Troms, where the avalanche deposits below Skredkallen ("Skrea") was mapped as moraines.

Studies of raised coastal basins and changes in sea-level were conducted by Corner and Haugane (1993). Their study on Vannøya identifed and dated isolation and ingression contacts in sediment cores retrieved from coastal lakes on Vannareid and Skipsfjorddal. Also worth mentioning is the recent (2019) masters project focusing on Skredkallen by Leif Trønnes, titled "Structural analysis and characterization of the rock slope failure at Skredkallen, Vannøya".

1.4 Geological setting

In terms of the regional geological setting, the island of Vannøya is the northernmost exposure of the West Troms Basement Complex (WTBC; Figure 3), which consists of Neoarchean tonalitic and granitoid gneisses, and Palaeoproterozoic mafic, igneous and volcano-sedimentary cover rocks (Zwaan, 1995, Bergh et al., 2010). These rocks have a variably oriented, mostly steep NW-SE-striking foliation and multiple/complex folds and ductile shear zone architectures (Bergh et al., 2010). The basement rocks are overlain to the east by Caledonian nappe rocks (Opheim and Andresen, 1989). On Vannøya, Neoarchean basement gneisses are overlain by a sedimentary unit, the low grade Vannøya Group meta-sandstones and mudstones (Binns et al., 1981), which was affected by Svecofennian (1.8 - 1.75 Ga) orogenic fold-thrust belt deformation (Bergh et al., 2007).

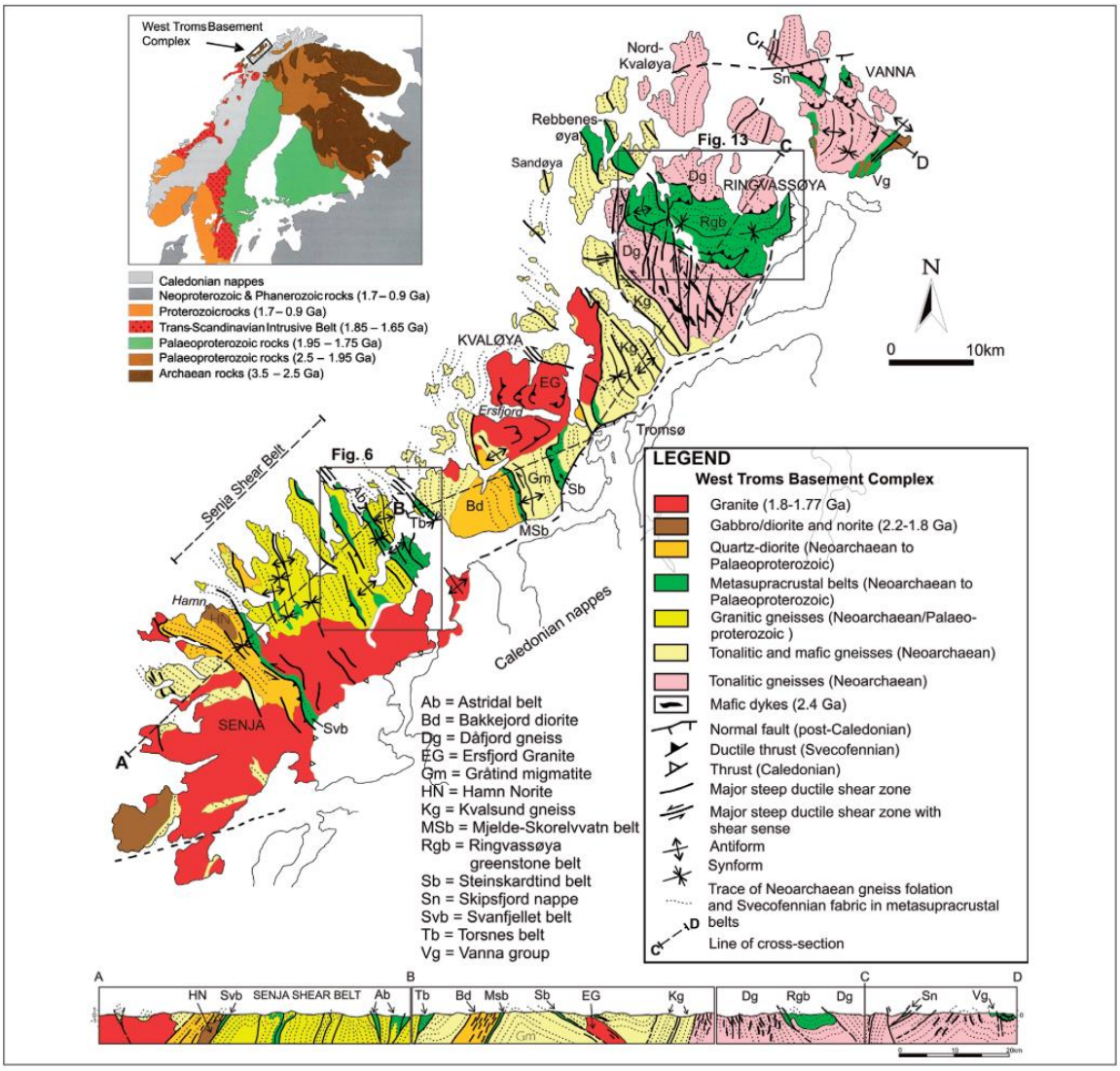

Figure 3: Regional geologic-tectonic map and cross section of the West Troms Basement Complex (Bergh et al., 2010).

The URS failure at Skredkallen is located in a preserved remnant of the Skipsfjord nappe (Figure 4). The Skipsfjord nappe was previously thought to be Caledonian in age but now known as pre-Cambrian WTBC (Opheim and Andresen, 1989). The lower boundary of the Skipsfjord nappe can be seen as a distinct topographical change across Olkeidet in the W and Laukvik in the E (Figure 4), a couple of km's S of Skredkallen (Opheim and Andresen, 1989). The base of the nappe is marked by an appearance of a fine-grained mylonite. The lithologies within the Skipsfjord nappe are mainly intensely mylonitized tonalitic orthogneisses, alternating with mylonitized metasedimentary sequences, both units containing lenses and layers of mafic material (Opheim and Andresen, 1989). Skredkallen is located in the basement of the Skipsfjord nappe, near to the boundary with the upper part of the nappe (Figure 5). The Skipsfjord nappe was subdivided into three lithotectonic units by Opheim and Andresen (1989), based on the metasedimentary lithologies. The three units are referred to as the lower mylonite-gneiss sheet, the Kvalkjeften group and the upper mylonite-gneiss sheet. At the base of the Skipsfjord nappe is the lower mylonite-gneiss sheet. The lowermost part of the gneiss sheet consists of protomylonitic to mylonitic tonalite orthogneiss interlayed with a very fine-grained, equigranular quartz-rich schistose rock, presumably of metasedimentary origin (Opheim and Andresen, 1989). The upper part of the gneiss sheet is more intensely strained and shows a relatively homogenous mylonite gneiss character. A number of mafic dykes are present in the gneiss-sheet and are likely to be pre-tectonic as they share the same deformation as the tonalite (Opheim and Andresen, 1989). The boundary against the overlying Kvalkjeften group is marked by the appearance of a mylonitic medium-grained quartzite (Figure 5).

The Kvalkjeften group has been interpreted by Opheim and Andresen (1989) as the depositional cover of the lower gneiss sheet. It is separated from the underlying gneiss sheet and the overlying thrust sheet by sharp boundaries. The Kvalkjeften group can be subdivided into two formation based on lithological differences (Geitdalen and Brattfjell formations). The Geitdalen formation is the lowest-lying of the two formations and is mainly composed of metapsammites. The overlying Brattfjell formation mainly consists of metapelite with layers of metapsammite in the upper part. Two types of intrusives (metadolerites and metadiorites) are found in the upper part of Brattfjell formation.

The uppermost unit of the Skipsfjord nappe is referred to as the upper mylonite-gneiss sheet. The composition of this gneiss-sheet is identical to the lower mylonite-gneiss sheet, although the texture is slightly more fine-grained in the upper sheet (Opheim and Andresen, 1989).

Some mafic dykes also occur in the upper gneiss sheet. These dykes share the same composition as those in the lower gneiss-sheet (Opheim and Andresen, 1989).

Outide of the Skipsfjord Nappe, to the south, the bedrock is predominantly massive tonalitic orthogneisses of the autochthonous basement.

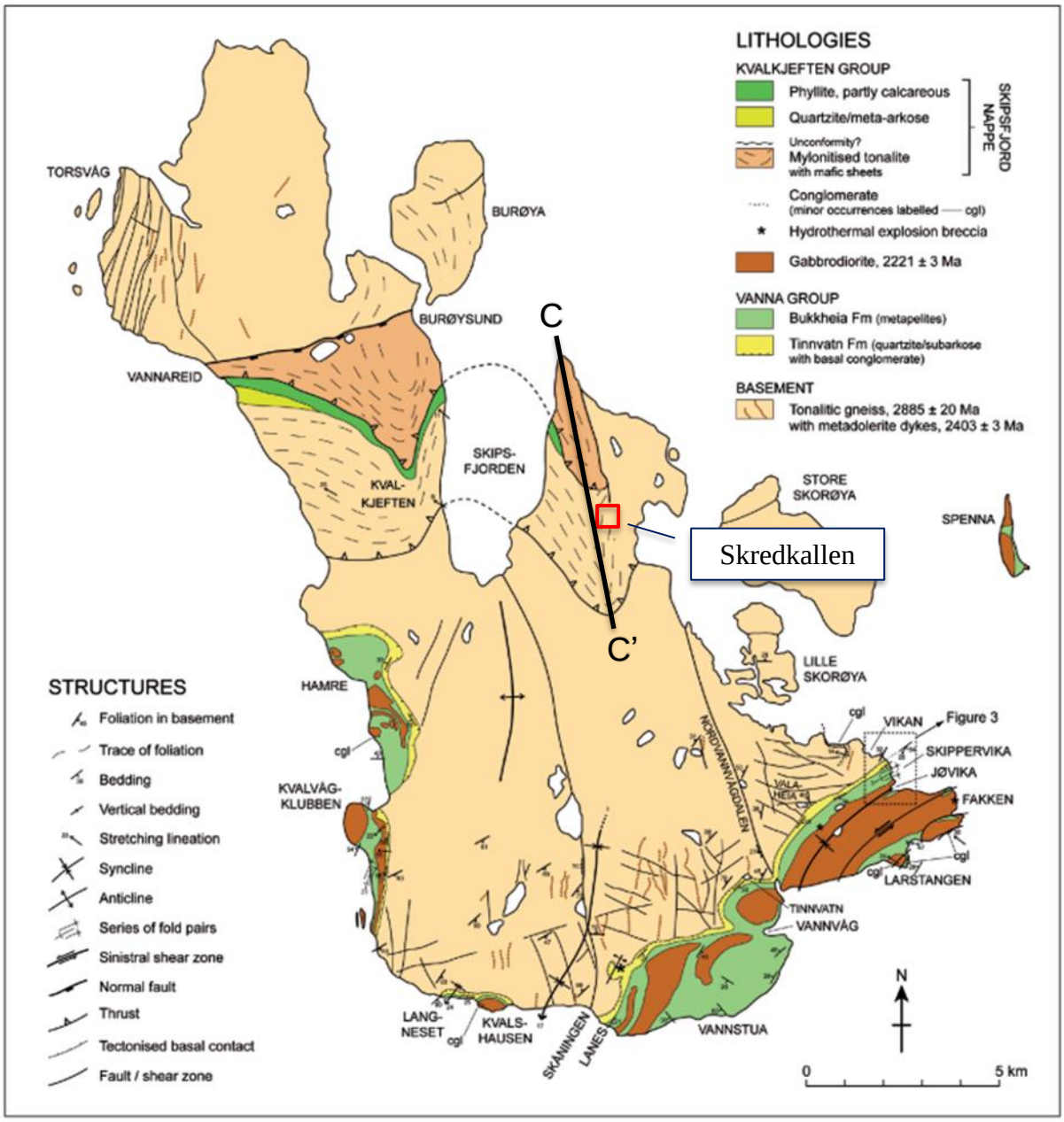

Figure 4: Geological and tectonic map of Vannøya (modified after Bergh et al. 2007).

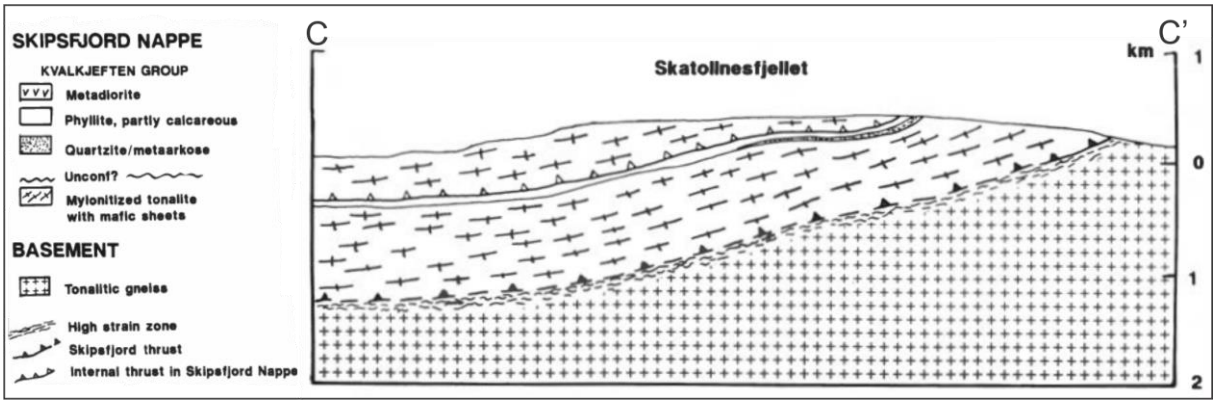

Figure 5: Geological cross-section across Skatollnesfjellet. Location of profile line are shown in Figure 4. Modified after (Opheim and Andresen, 1989).

1.4.1 Post Caledonian Structures

The island of Vannøya comprises some Paleozoic-Mesozoic brittle normal faults and fracture sets striking formed during the rifting and opening of the North Atlantic and Barents Sea margins. These fault/fracture sets are widespread and provide zones of weakness in the bed rock throughout western Troms (Indrevær et al., 2013).

The continental margin off central/mid Norway was subjected to multiple rift events in the Palaeozoic through to Early Cenozoic times as a part of the break-up of the Atlantic Ocean (Bergh et al., 2007). As a result, a network of onshore and offshore faults were formed. Along the West Troms margin, onshore brittle faults are mostly oriented in a NNE-SSW and ENE-WSW orientation (Figure 6) within both the Caledonian and WTBC terranes (Indrevær et al., 2013). On Vannøya these manifest as lineaments striking NE-SW, NNE-SSW and NW-SE Bergh et al., 2007) forminga zig-zag pattern (Figure 6).

The WTBC is flanked is by normal faults in the south (Blystad, 1995, Bergh et al., 2007, Hansen and Bergh, 2012, Indrevær et al., 2013). In the north, it is flanked by the Vestfjord-Vannøya Fault Complex (VVFC; Andresen and Forslund, 1987, Forslund, 1988, Opheim and Andresen, 1989, Olesen et al., 1997, Roberts and Lippard, 2005, Indrevær et al., 2013). The fault zones along the VVFC in general show down-to-southeast normal displacement in the order of 1-3 km relative to the Caledonian nappes (Indrevær et al., 2013). No clear boundary-fault has been mapped on the seaward side of the of the WTBC, instead some less prevalent fault zones exist (Indrevær et al., 2013). The western fault zones are characterized by NE-SW to N-S-trending fault segments showing red staining of host-rock granites, comprising mostly cataclastic fault rocks and hydrothermal alteration zones. The fault zones have a normal to oblique-normal, down-to-the-SE fault movement. It is suggested by Indrevær et al. (2013)

that the fault zones may link up to an en-echelon, right-stepping, fault segment that run parallel to the VVFC. The fault zones do not define the northwestern limit of the WTBC horst, but rather described as a transfer zone that runs NW-SE from the mainland near Nord-Fugløya, located just NE of Vannøya (Indrevær et al., 2013).

Dating using $^{40}Ar/^{39}Ar$ and apatite fission-track have been done to indicate that faulting in western Troms mainly occurred during Permian to Early Triassic rifting phase (Indrevær et al., 2013).

Several major fault zones are present within in the interior parts of WTBC, including the Vannareid-Burøysund Fault on Vannøya (Figure 6). The ENE-WSW-trending and c. 60° dipping fault downdrops the Skipsfjord Nappe by at least 3 km (Opheim and Andresen, 1989, Indrevær et al., 2013). The fault zone is shown in the topography as an ENE-WSW-trending valley in the northern parts of Vannøya, with a minimum 20 m-wide cataclastic zone of cataclasites. Slickensided surfaces indicate a pure dip-slip, down-to-the-SSE displacement along the fault (Indrevær et al., 2013).

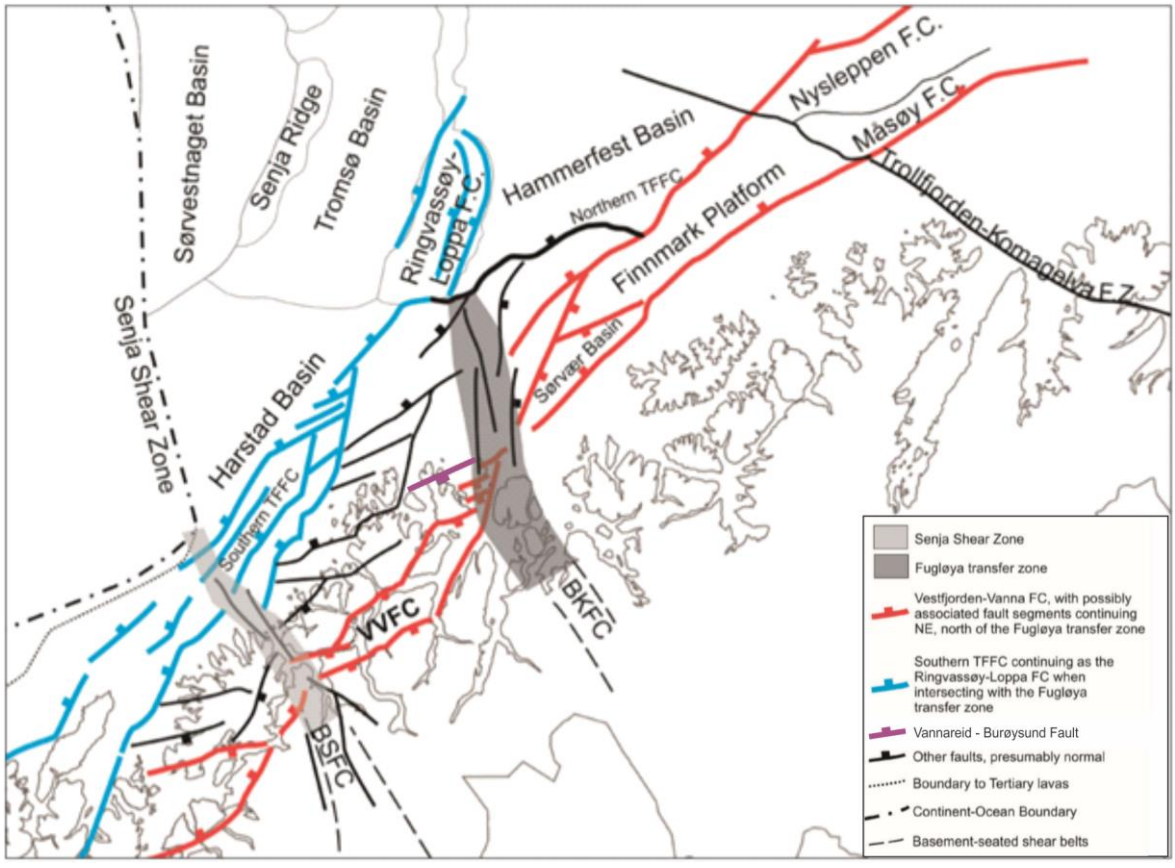

Figure 6: Simplified tectonic map of the coastal areas of Troms and Finnmark. The map illustrates the NNE-SSW and ENE-WSW trending fault complexes onshore and offshore. The Fugløya transfer zone is located just east of Vannøya (Modified after Indrevær et al. (2013)).

1.5 Climate and permafrost at Vannøya

The western and northern coast of Norway in general is classified as a storm-wave environment (Corner, 2005). Vannøya is no exception as it is facing the Norwegian Sea, and is therefore frequently facing high waves (>4 m height) and strong winds. As a result of this, the island is mostly treeless, with low-lying vegetation.

Skredkallen lies within the subarctic climate zone. The zone is characterized by long cold winters, and short cool to mild summers. Climate information is available for the whole of northern Norway (Figure 7), and more specifically from the Torsvåg weather station, about 10 km north of Skredkallen on Vannøya (Figure 8, location shown on Figure 4). The average temperature on Torsvåg from April 2018 – April 2019 was 5.1 ℃. The temperatures recorded in this period show variations from 25.7 ℃ at the warmest to -10.4 ℃ at the coldest (Figure 8). The average temperature is some degrees warmer compared to the average for northern Norway, which is slightly below freezing point (Figure 7). As Skredkallen is situated about 450 m above Torsvåg, it is estimated to be c. 2.9 ℃ colder than at Torsvåg by using a standard lapse rate of -0.65 ℃/100 m. There are no rainfall records from Torsvåg as the station does not contain a rain gauge. However the total yearly rainfall in Tromsø is typically between 800-1000 mm (Klimaservicesenter, 2019).

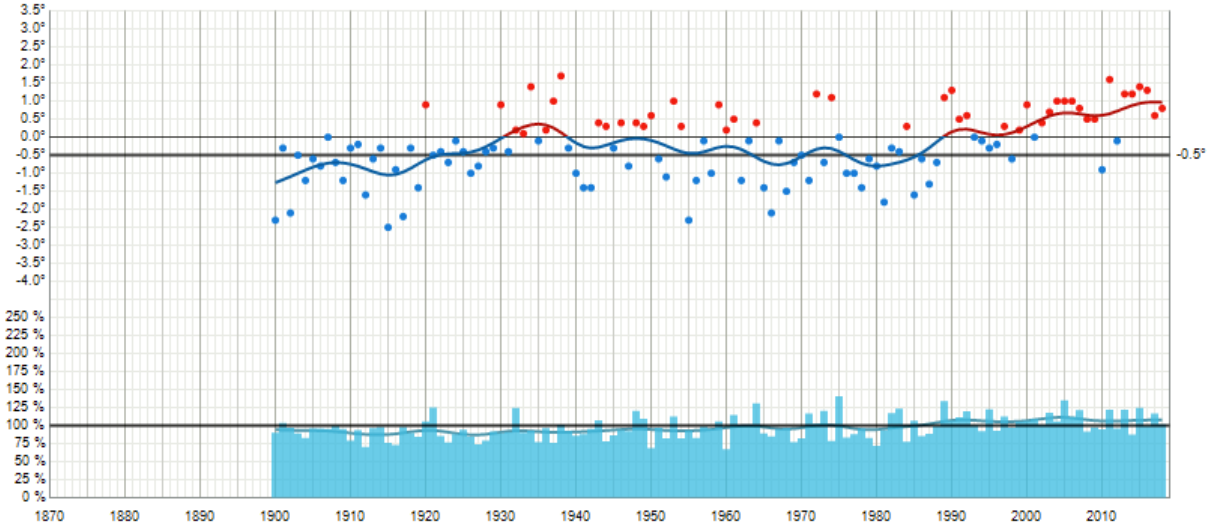

Figure 7: Long term statics for yearly temperature and precipitation for northern Norway. Points indicate yearly temperature. The trend line is a 10 year Gaussian distribution. The average is drawn as a thick horizontal line. Precipitation is presented by blue bars at the bottom overlaid with the average, which is drawn as a thick line. The average is based on a 30 year period (1961 - 1990; Yr, 2019).

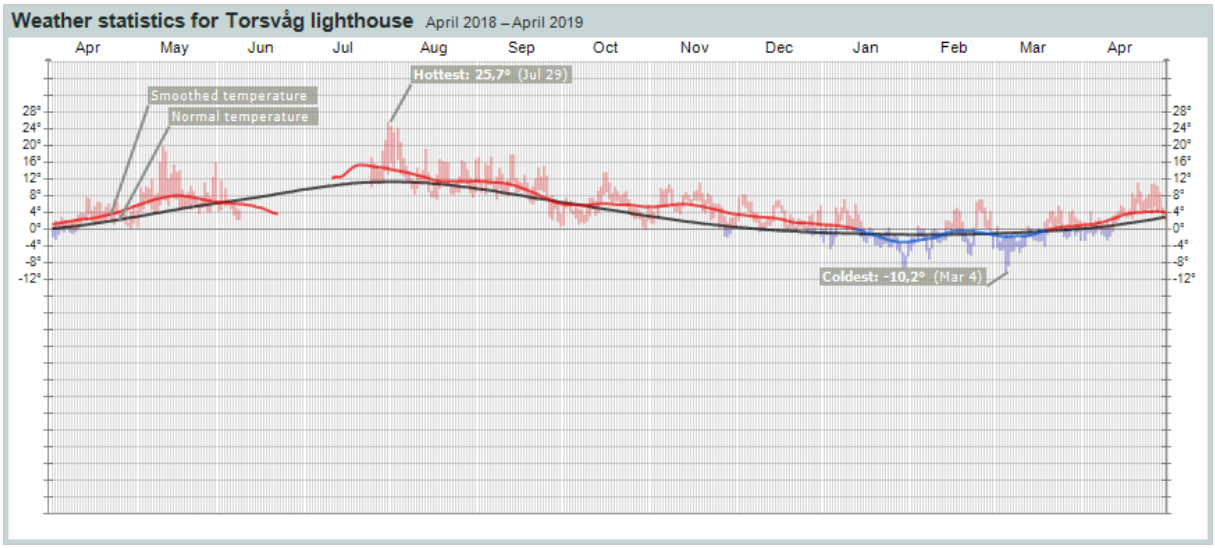

Figure 8: Weather statics for one year, measured at a weather station 10 km from Skredkallen at an elevation of 21 m asl. Some data records are missing in this figure (Yr, 2019).

Continuous and discontinuous permafrost exists in the mountainous and continental areas of Scandinavia (Figure 9). Isolated patches of permafrost outside the discontinuous permafrost zone, known as sporadic permafrost (Figure 10; King, 1986), might in some places be found close to sea-level (Kjellman et al., 2018). Large parts of the permafrost are at 0°C, and a few degrees below freezing point in the highest mountain parts (Christiansen et al., 2010). The permafrost at freezing point is sensitive to climate changes, and several unstable rock slope areas are associated with warm and presumably degrading permafrost (Christiansen et al., 2010). The lower limit for mountain permafrost in Troms is found to be at 800 - 900 m asl in the outermost coastal areas of Troms (Christiansen et al., 2010). As the elevation of the unstable rock slope at Skredkallen is several hundred meters below this, it is by definition outside of the permafrost zone. However, sporadic permafrost might exist closer to sea level in deep-seated rockslide terrain (Blikra and Christiansen, 2014). The fracture topography of rockslides in periglacial environments allows significant cold air accumulation to occur in wide and deep open cracks. The resulting ventilation effect lowers the air temperature within the fractures. This enables ice rich permafrost to develop in open fractures and also along parts of the active sliding planes (Blikra and Christiansen, 2014).

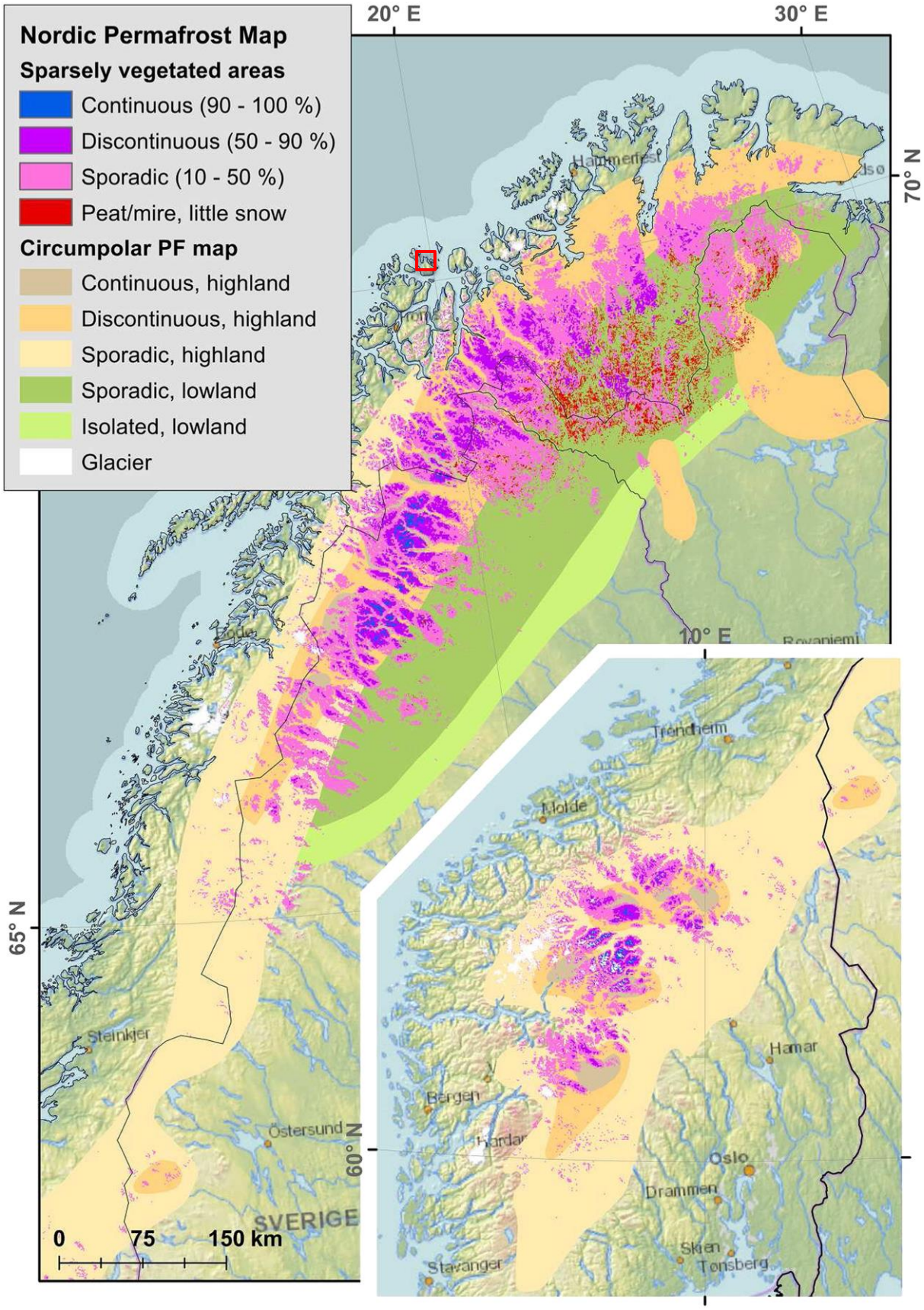

Figure 9: Permafrost map of the Scandinavian Peninsula showing the permafrost mapped by Gisnås et al. (2017) and the Circumpolar map by Brown et al. (1997). The study site is marked within the red rectangle. Modified after Gisnås et al. (2017).

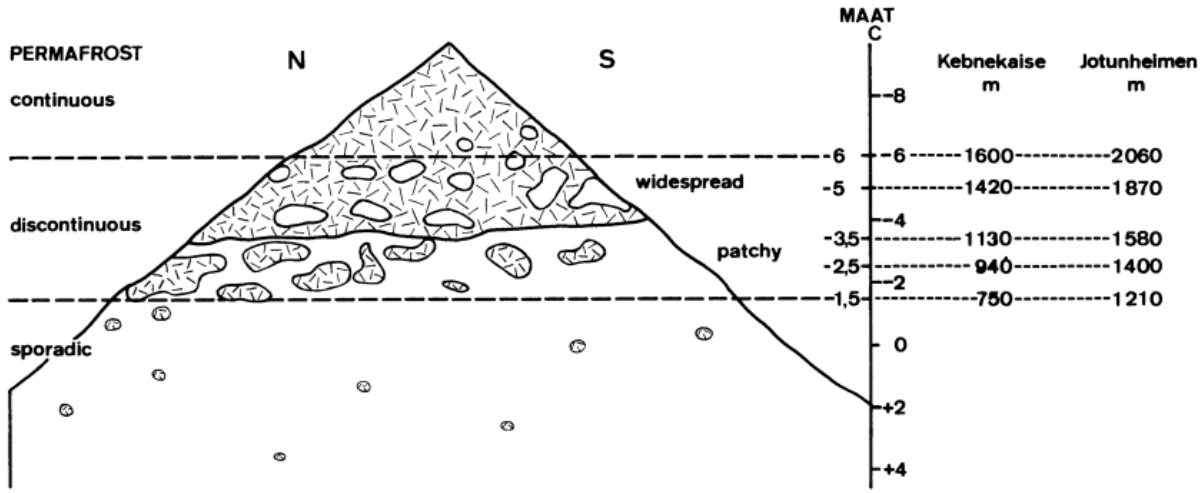

Figure 10: Illustration of different types of permafrost and their relation to altitude in mountainous areas (King, 1986).

1.6 Rock slope failures in Troms

In this thesis, RSFs are differentiated from URS's as they are deposits of failed rock masses, whilst URSs are currently unstable rock masses that are yet to fail.

RSF deposits are common geological features in certain regions of Norway. Geological mapping on land and in fjords of northern and western Norway has revealed a high frequency of RSFs throughout the last 10,000 years (Blikra et al., 2006). In Troms county, the most common features are large rock avalanches and rock glaciers of rock-avalanche origin (Blikra et al., 2006). Over 150 such features were mapped by Blikra et al. (2006). The geographic distribution of RSF events show a clustering in specific areas (Figure 11). The largest cluster is located east of the Lyngen peninsula in the northeastern part of Troms County. This is attributed to the lithology- most of the slope failures have formed in Caledonide metasedimentary rocks rather that metavolcanics (Bunkholt et al., 2012). The former are generally known to be of a lower strength than the latter (Mair am Tinkhof 2010). Skredkallen is located within the red square on Figure 11, and was not mapped at the time of the study.

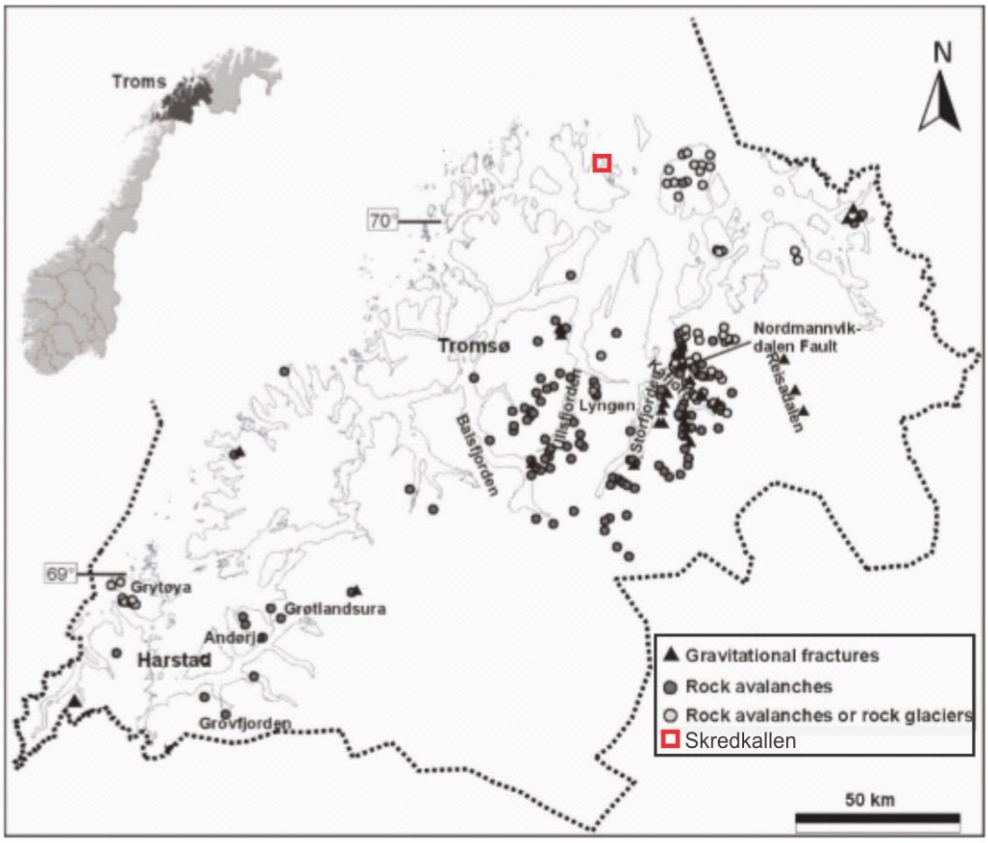

Figure 11: Map showing the location of gravitational fractures, rock avalanches and rock glaciers in Troms County, Northern Norway. Skredkallen is marked within the red cube. Modified after Blikra et al. (2006).

Rock glaciers are lobate landforms consisting of rock debris and either an ice core or an ice-cemented matrix (Giardino et al., 1987). Several rock glaciers in Troms were dated by Blikra et al. (2006) and found to have formed between 11 – 10.5 ka, likely by rock avalanche activity. Deposits are found either outside of the YD moraine margin, or on inferred nunataks within the YD ice margin. Active rock glaciers are still found in Troms today, within the permafrost zone (Eriksen et al., 2018).

1.6.1 Trigger mechanisms of a rock slope failure

Important trigger mechanisms for rock slope failures are related to seismic activity, creep processes and glacial unloading (debutressing) during deglaciation. It is suggested that the peak of rock slope failure activity occurred after deglaciation (Cruden and Hu, 1993, Ballantyne et al., 2014, Hermanns et al., 2017). Radiocarbon dated events by Blikra et al. (2006) show that previous events mostly occurred 11,000 to 10,500 calendar years BP, less than 1000 years after deglaciation, indicating that the most important mechanisms are related to glacial unloading. Several rock slope failures in western Norway dated by Blikra et al. (2006) show a high activity in the past 5,000 years, with a peak activity around 3,000 years, indicating that other possible triggering mechanisms may have been at play, for example

seismic activity (from isostatic rebound) and permafrost thaw during climate warming events and periods of increased precipitation.

1.6.1.1 Glacial debutressing

Ice downwastage and retreat results in debuttressing of rockwalls, causing fluctuations in the state of stress within the rock mass (Ballantyne, 2002). Three possible modes of response are described by Ballantyne (2002), initiated as a result of alternating states of stress:

1. Large-scale, catastrophic rock slope failure as major rockslides or rock avalanches.
2. Large-scale rock mass deformation as progressive slow movements, which could ultimately lead to catastrophic failure.
3. Rapid adjustment of rock faces by frequent discrete rockfall events, resulting in an accumulation of talus debris at the slope foot.

Glaciation and deglaciation may affect rock mass stability in two ways (Augustinus, 1996, Ballantyne, 2002). The first is glacial erosion, as it steepens rock slopes, especially in mountainous areas where ice flow is concentrated in glacial troughs. This type of slope-steepening increases overburden, and thereby the shear stresses acting on the rock. Deepening of troughs by glacial erosion also increases the height of rock faces, leading to an additional increase in shear stress (Radbruch-Hall et al., 1976, Ballantyne, 2002). Because of these effects, tensile stress conditions might occur at the head of the slope and promote failure along pre-existing joint planes or other zones of weakness during or after ice retreat.

The second way stability of rock masses may be affected is by glacial unloading and consequent stress-release (Ballantyne, 2002). In troughs occupied by valley glaciers, the weight of the ice increases stress levels on the valley floor and within the valley walls. In most rock types, part of the rock mass deformation caused by ice-load is elastic and stored within the rock mass as residual strain energy (Wyrwoll, 1977, Ballantyne, 2002). As the ice sheet retreats, the strain energy is released as a result of the unloading. The result is a "rebound" or stress-release within the rock. The magnitude of rebound is dependent on the amount of residual strain energy and bedrock characteristics of the slope (Ballantyne, 2002). The relaxation of internal stresses within a rock mass may lead to immediate or delayed rock slope failure due to propagation of internal joint systems, loss of cohesion along joint planes and reduction of internal locking stresses. The timing of the failure in dependent on the dissipation of residual stresses within the rock mass (Wyrwoll, 1977, Ballantyne, 2002).

Additional destabilizing effects may also play an important role in reducing rock mass stability during/after glaciation. Glacially formed valleys within tectonic systems (e.g. orogenic belts) may have additional redistribution of stresses within the rock mass adjacent to a free face (Augustinus, 1995, Ballantyne, 2002). Propagation of internal joint sets due to stress release may lead to enhanced joint-water pressures that ultimately facilitate failure, especially in areas that are subject to seasonal freezing (Ballantyne, 2002). Chemical weathering along joints, especially in carbonates, may reduce the long-term shear strength along potential failure planes (Ballantyne, 2002). In tectonically active regions, seismic shocks could trigger failure of rockwalls where the state of stability is critical by one or more of the previous mentioned processes (Ballantyne, 2002).

1.7 Quaternary geology

The Quaternary period (the last 2.6 million years) is characterized by frequent climate changes, leading to glaciation- and interglacial events as a result of cyclic variations in solar radiation due to orbital changes (Milankovitch cycles; Nesje et al., 2012). The last glacial period recorded in Northern Europe is known as the Weichselian (c.115 ka – 10 ka). During the Last Glacial Maximum (LGM; c. 28 – 20 ka) the ice sheet covered the Norwegian continental shelf (Figure 12; Mangerud et al., 2011, Nesje et al., 2012).

Deposits from previous interglacial times are only found in a few locations as the Weichselian ice sheet removed most of the older material. Two sets of moraines can be found in Troms as a result of periods of colder climate and glacial advances. The youngest and most distinct deposits are from a glacial advance in the YD, known as the Tromsø-Lyngen advance (11 ka – 10 ka; Figure 13 A). The other set of moraines are deposits from the Skarpnes event (12.5 – 12 ka; Figure 13 B). These moraines are smaller and less distinct, and they are usually not as continuous as the Tromsø-Lyngen moraines (Andersen, 1968). The Skarpnes moraines are found 4-6 km outside the Tromsø-Lyngen end moraines (Andersen, 1968). Even though the Skarpnes glaciers were slightly larger than the glaciers of the following Tromsø-Lyngen event, it is assumed that the climate was similar during these two events (Andersen, 1968).

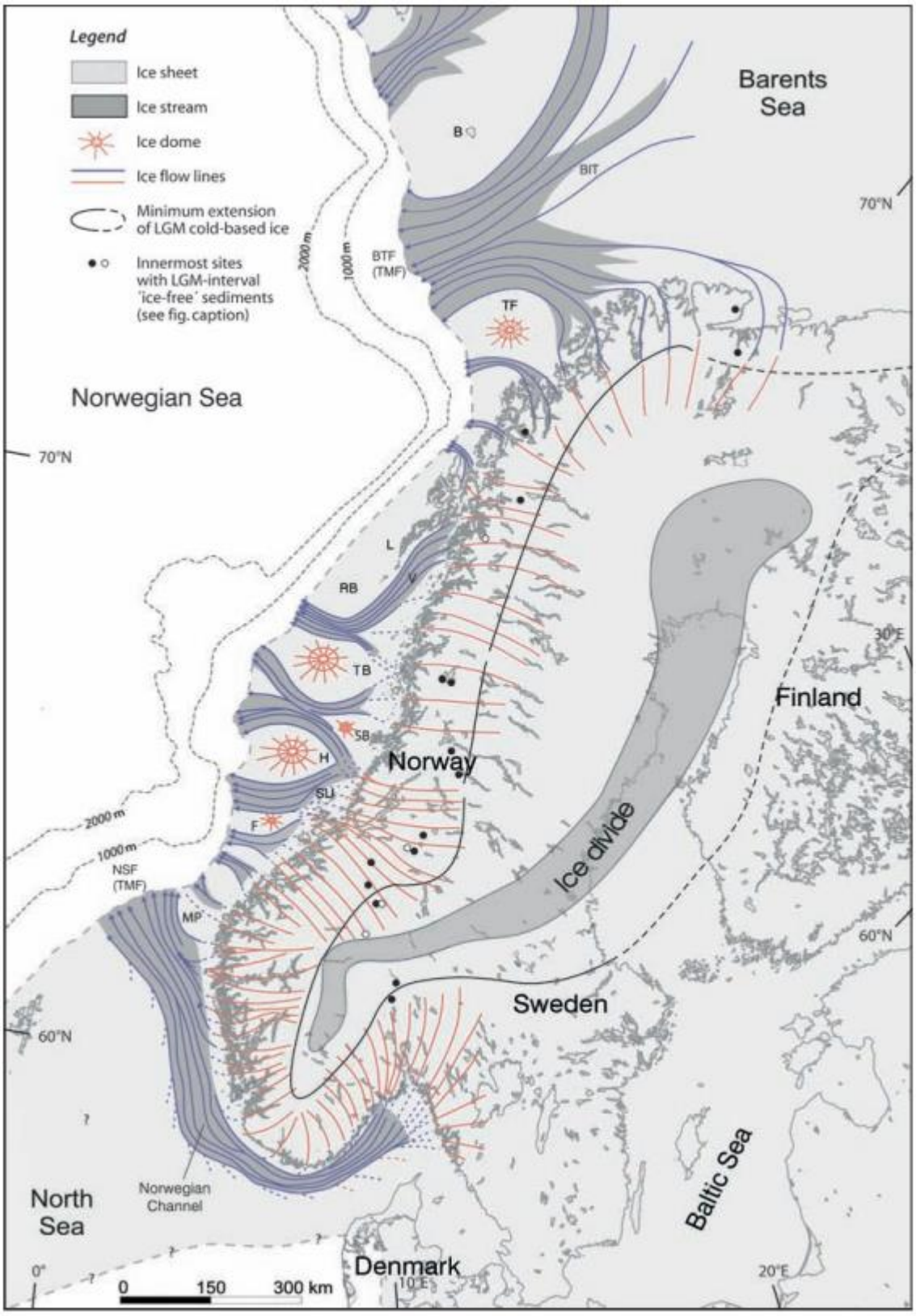

Figure 12: Extent of the ice sheet during LGM with assumed ice-flowing patterns (Ottesen et al., 2005).

Glacially formed valleys with associated end-moraines were mapped by Andersen (1968). These moraines were mapped as four separate Island-phases (Island I – IV), where Island I represent the youngest moraines and Island IV the oldest. Moraines outside the Tromsø-Lyngen moraines in western Troms were mapped as Island II phase by Andersen (1968). These moraines are usually the most distinct local moraines along the coast. The moraines represent several glacial phases where the glacial conditions were very similar. The youngest Island II moraines are the most dominant and are situated just outside the Tromsø-Lyngen end moraines (Andersen, 1968). Andersen (1968) calculated the Island II regional glaciation limit on Southern Vannøya to be at 465 m asl. His calculations are based on observations from aerial photographs.

Vannøya is situated between the assumed limit of the Weichselian ice sheet and the Tromsø-Lyngen (YD) end moraine (Andersen, 1968), and is assumed to have been deglaciated between 13,000 and 15,000 yrs BP (Corner and Haugane, 1993). Although the Tromsø – Lyngen ice sheet did not cover the island of Vannøya (Figure 13 A), some local glaciers (Island II phase) might have been present at the time (Corner and Haugane, 1993).

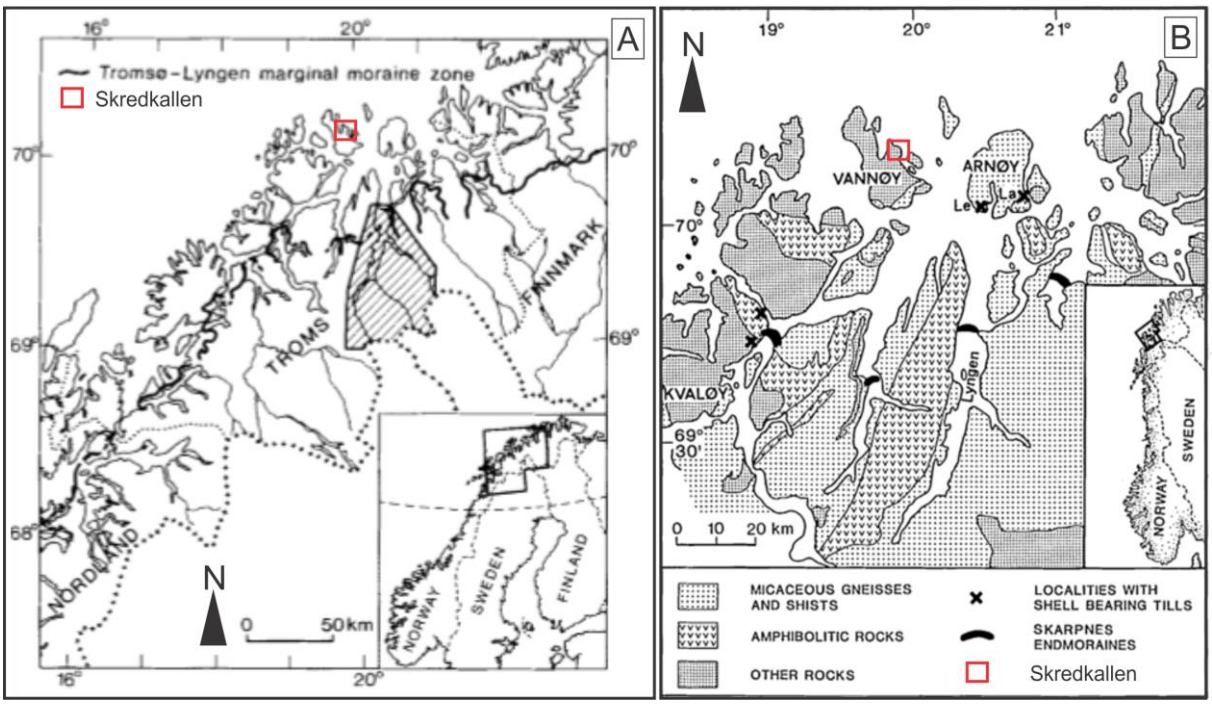

Figure 13 A: Map showing the extent of the Tromsø – Lyngen marginal moraine (according to Andersen (1968)). Modified after Corner (1980). B: Geological map of northern Troms showing the extent of the Skarpnes moraines. Modified after Andreassen et al. (1985).

1.7.1 Isostatic uplift

When the continental crust is suppressed by a great gravitational force, e.g. a continental ice sheet, it depresses as a response to the additional weight. The crust starts to rebound to its original state once the additional weight disappears. As the crust is depressed or rebounded, it deforms by two components: an elastic deformation of the crust and a plastic deformation of the underlying mantle (Jørgensen et al., 1997). The elastic deformation has a quick response time, and is responsible for the isostatic uplift within the first 3,000 years after deglaciation (Jørgensen et al., 1997). The plastic deformation in the mantle happens by mass movements within the layer or by mineral changes at greater depths. These are significantly slower processes and have been the main contributor to isostatic uplift for the last 5,000 years (Jørgensen et al., 1997).

Glacio-isostatic uplift in Fennoscandia started during the last glaciation (Dehls et al., 2000). Unloading of the crust from deglaciation resulted in differential glacio-isostatic adjustment, meaning the uplift was greatest where the ice sheet was thickest (Jørgensen et al., 1997, Ballantyne, 2003), and is therefore low along the NW coast of Norway. The coast of Troms County is currently being uplifted by a rate of 1 – 1.5 mm a^{-1} (Figure 14) compared with a rate of 8 mm a^{-1} in eastern Sweden where the ice sheet was thickest (Dehls et al., 2000). Differential rebound is known to have reactivated inherited faults which have accommodated the stress distribution of the crustal deformation, and this will likely have triggered earthquakes (Ballantyne, 2003).

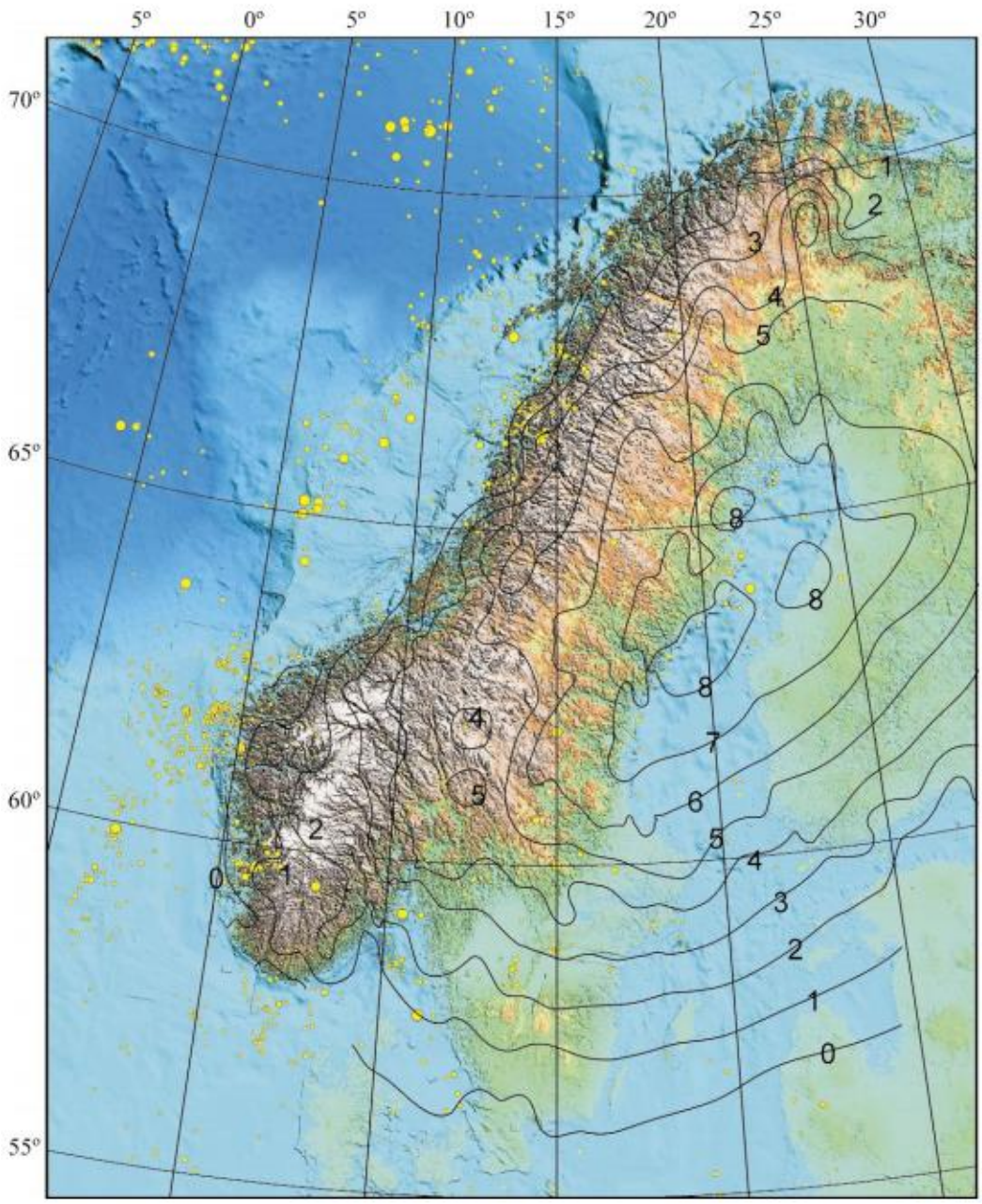

Figure 14: Map of Fennoscandia showing the current uplift rates (in mm a^{-1}) and earthquakes with magnitudes greater than 3.0 (Dehls et al., 2000).

1.7.2 Marine limit and raised shorelines

A Marine Limit (ML) is defined as the uppermost post-glacial sea-level recorded (Jørgensen et al., 1997, Høgaas et al., 2012). The eustatic sea-level has risen by 120 m since the last glaciation (Nesje et al., 2012). However, local MLs vary due to differential uplift (Figure 14). A study by Corner and Haugane (1993) suggests the ML was formed at the time of deglaciation, and lies at approximately 47 m asl in Skipsfjorden (Figure 15 A and B).

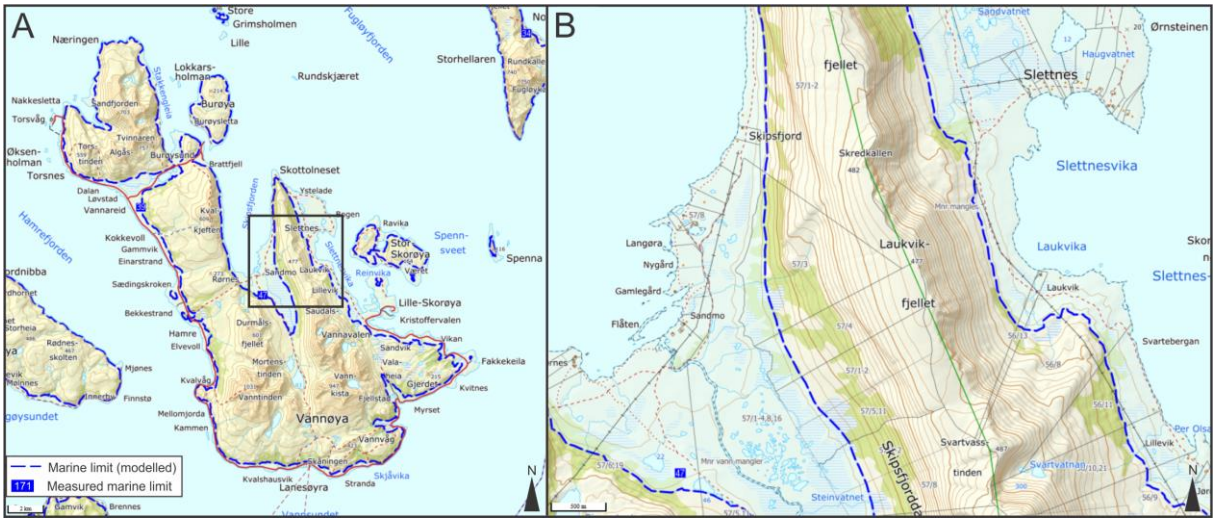

Figure 15: A: ML on Vannøya. The ML is measured to be 47 m asl in Skipsfjorden and 39 m asl on Vannareid. The black rectangle show the extent of map B. B: Zoomed in map of the surrounding area of Skredkallen (map from NGU (2019b))

Raised shorelines are shorelines formed by normal coastal processes and uplifted and exposed due to isostatic rise (Figure 16; Jørgensen et al., 1997). Shorelines can vary is characteristic as a result of synergetic climatic processes, for example rapid eustatic sea level change will result in a more pronounced shoreline (Jørgensen et al., 1997). Three shorelines are recognised on Vannøya, including the ML. The "Main" and "Tapes" shorelines (Andersen, 1968, Corner and Haugane, 1993) formed below the ML. The Main shoreline formed during YD and lies at an elevation of c. 22 m asl (Corner and Haugane, 1993). The Main shoreline corresponds to the Tromsø-Lyngen advance and has as a result of the uneven isostatic rebound an inclination of approximately 1 m/km (Andersen, 1968). In many localities it is observed as terraces in the bedrock.

The Tapes shoreline was formed during the Tapes transgression maximum in the mid-Holocene (measured in Lyngen to c. 7000 ^{14}C-yrs BP by Corner and Haugane (1993), calibrated to 7580 yrs BP using method described in section 2.2.1) as a response to global warming. The warming caused a rise in global sea-level which was greater than the isostatic rebound in the coastal areas of Norway (Svendsen and Mangerud, 1987, Høgaas et al., 2012). The Tapes shoreline reaches c. 12 m asl (Corner and Haugane, 1993).

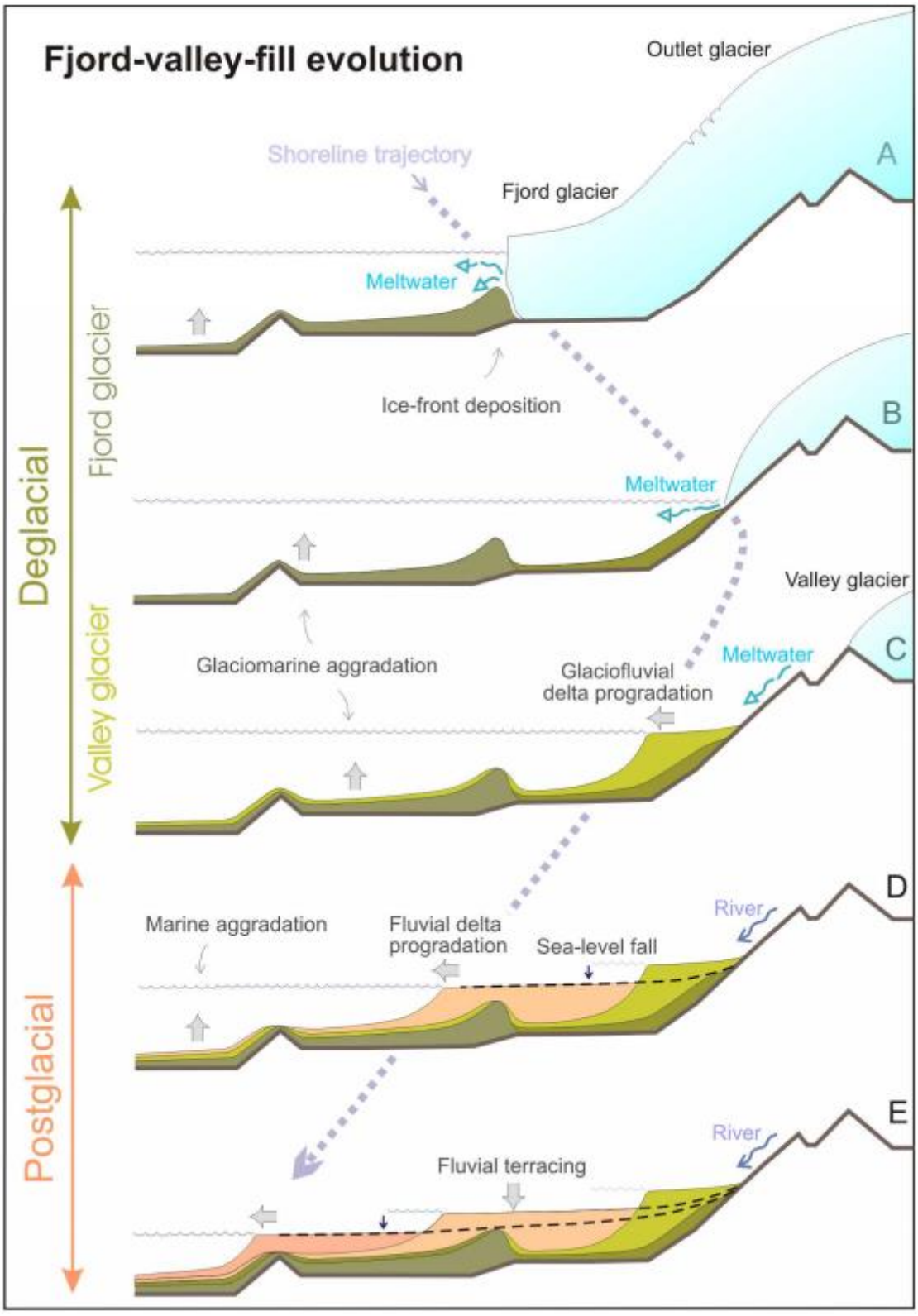

Figure 16: Stages in evolution of a fjord valley during and after glacier retreat. Modified by Corner and Eilertsen (2008) after Corner (2006).

1.8 Definitions

1.8.1 DSGSD

Deep-seated slope gravitational deformations (DSGSD) are large mass movements on high-relief valley walls that extend from near the valley floor to, or beyond, the ridge crest. They can be found in most rock types and are generally characterized by discontinuous and poorly defined lateral boundaries, large volumes (>0.5 km^3) and thicknesses, conspicuous surface features, and low rates of movement over long periods (Varnes et al., 1990, Ambrosi and Crosta, 2006, Agliardi et al., 2012). The most common indicators of a DSGSD is deformational features (e.g. Scarps, counterscarps, trenches, grabens). DSGSD occurrence is closely related to specific geologic and structural features (bedding, foliation, faults and folds) and topographic features (valley bends and slope gradient changes; Agliardi et al., 2012).

1.8.2 Failure mechanisms

Rockfall: Rockfalls are abrupt, downward movements of rock, or both, that detach from steep slopes or cliffs. The falling material usually strikes the lower slope at angles less than the angle of fall, causing bouncing. The falling mass may break on impact, begin rolling on steeper slopes, and continue until terrain flattens (Figure 17; Highland and Bobrowsky, 2008).

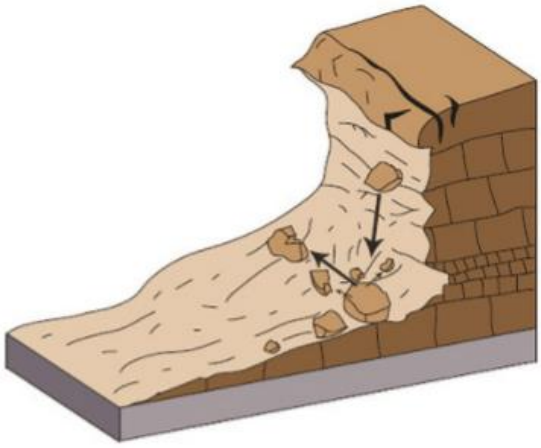

Figure 17: Schematic model of a rockfall (Highland and Bobrowsky, 2008).

Direct topple: Forward rotation and overturning of rock columns or plates (one or more), separated by steeply dipping joints. The rock is relatively massive and rotation occurs on well-defined basal discontinuities (Figure 18). Movement begins slowly, but the last stage of failure can be extremely rapid (c. 5 m/s). Occurs at all scales (Hungr et al., 2014).

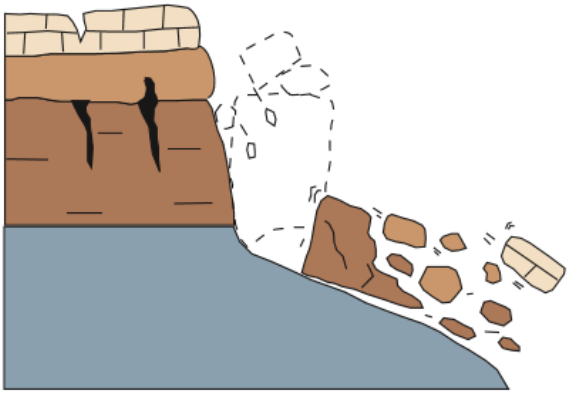

Figure 18: Schematic model of a topple (Highland and Bobrowsky, 2008).

Flexural topple: Bending and forward rotation of a rock mass characterized by closely spaced, steeply dipping joints or foliaiton, striking parallel to the face of the slope (Figure 19). The rock is relatively weak. No well-defined basal joints are present, so that rotation of the strata must be facilitated by bending. The movement is generally slow (c. 1,6 m/a^{-1}.) and tends to self-stabilize. However, secondary rotational sliding may develop in the hinge zone of the topple. It can occur on a large scale (Hungr et al., 2014).

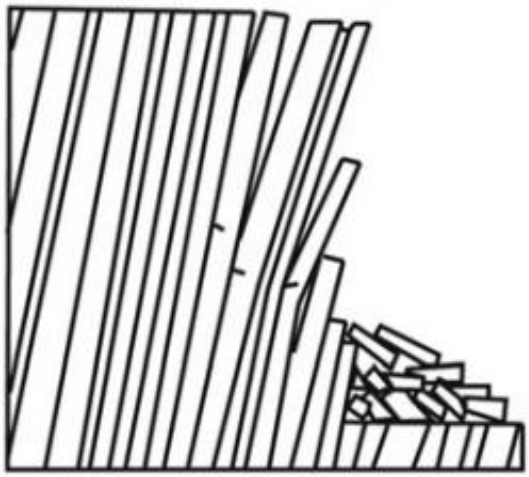

Figure 19: Schematic model of flexural topple (Goodman, 1976, Brideau and Stead, 2010).

Planar slide: Sliding of a mass of rock on a planar rupture surface (Figure 20). The surface may be stepped forward. Little or no internal deformation. The slide head may be separating from stable rock along a deep, vertical tension crack. Rapid failure (c. 1.8 m/h; Hungr et al., 2014).

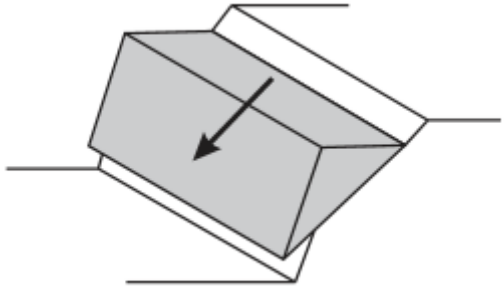

Figure 20: Sketch of planar failure along one slide plane (Wyllie and Mah, 2004).

Wedge slide: Sliding of a mass of rock on a rupture surface formed by two planes with a downslope-oriented intersection (Figure 21). No internal deformation. Failure occurs extremely rapidly (c. 5 m/s; Hungr et al., 2014).

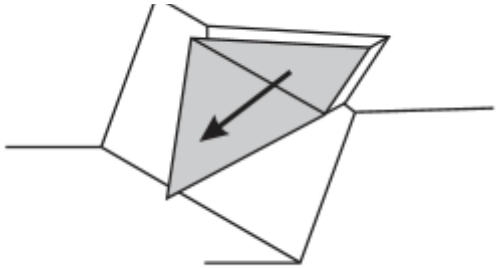

Figure 21: Sketch of wedge failure on two intersecting discontinuities (Wyllie and Mah, 2004).

Rock compound slide: Sliding of a mass of rock on a rupture surface consisting of several planes, or on a surface of uneven curvature, so that motion is kinematically possible if accompanied by significant internal distortion of the moving mass (Figure 22). Horst-and-graben features at the head and many secondary shear surfaces are typical for this type of failure. Failure may occur either slow or rapid (c. 1.6 m/a-1 – 1.8 m/h; Hungr et al., 2014).

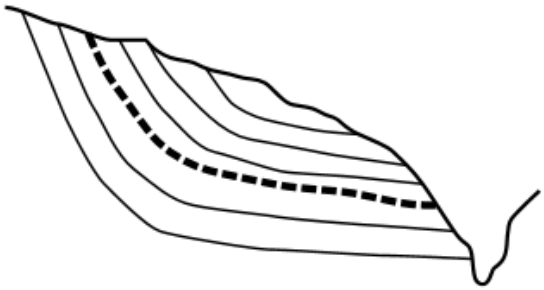

Figure 22: Schematic diagram of curved compound slide (Hermanns and Longva (2012) after Braathen et al. (2004), Glastonbury and Fell (2010)).

Rock irregular slide ("Rock collapse"): Sliding of a rock mass on an irregular rupture surface consisting of several randomly oriented joints, separated by segments of intact rock (Figure 23). Occurs in rocks with non-systematic structures. Failure mechanism is complex and usually difficult to describe. Elements of toppling might be included. Often sudden and extremely rapid sense of failure (c. 5 m/s; Hungr et al., 2014).

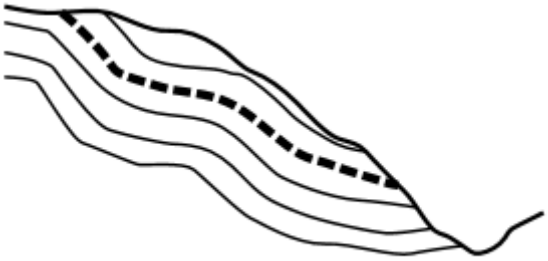

Figure 23: Schematic diagram of irregular compound slide (Hermanns and Longva (2012) after Braathen et al. (2004), Glastonbury and Fell (2010)).

1.8.3 Rock avalanche

Rock avalanches are defined as gravitational mass movements involving a large mass of rock debris that slides, flows, or falls rapidly down a mountain slope (Braathen et al., 2004). The cause of rock avalanches are instabilities in mountain slopes. Such instabilities are triggered by various local forces (Braathen et al., 2004).

1.8.4 Geomorphology and morphostructures

Morphostructure: The morphological expression of a deformational structure of tectonic or gravitational origin or by their interaction (Agliardi et al., 2001).

Scarp: Morphological expression of a downhill dipping collapse or main failure surface with a downslope movement (Figure 24).

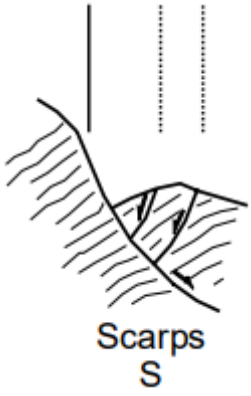

Figure 24: Schematic diagram of scarps (Agliardi et al., 2001).

Counterscarp: Scarp with an opposite dip-direction of the back scarp (Figure 25; Agliardi et al., 2001).

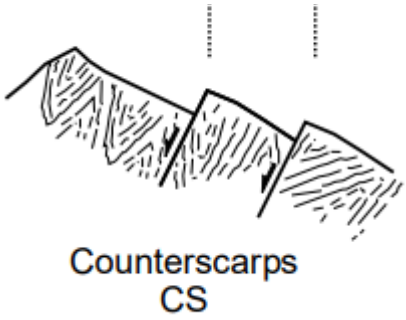

Figure 25: Schematic model of counterscarps (Agliardi et al., 2001).

Trench: Linear and deeply cut form, expression of extensional opening of a vertical or downward dipping surface (Figure 26).

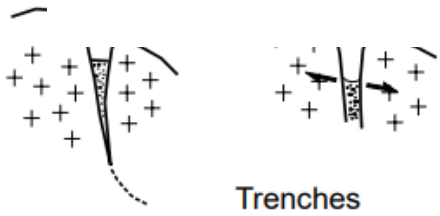

Figure 26: Schematic diagram of trenches (Agliardi et al., 2001).

Backscarp: Scarp which marks the boundary between the bedrock and the unstable area.

Joint: A fracture dividing rock into two sections that moved away from each other.

Terrace: A step-like landform. Consists of flat or gently dipping geomorphic surface. Usually bounded to one side by a scarp.

Flank: In situ material adjacent to sides of surface of rupture (Wyllie and Mah, 2014).

Lineaments: A linear landscape feature that is distinctly different from other features nearby and that reflects an underlying geological structure (Allaby, 2013).

Fault: A discontinuity surface separating two rock masses across which there has been shear displacement.

Horst: Up-thrown block lying between two steep-angled fault blocks (Allaby, 2013).

Graben: A downthrown, linear, crustal block, bordered lengthways by normal faults (Allaby, 2013).

Solifluction: Slow downslope flow of saturated unfrozen earth materials (Harris et al., 1988).

Talus: A sloping mass of coarse rock fragments accumulated at the foot of a cliff or slope (Allaby, 2013).

Unstable rock slope: An area that has moved from its original geological location.

2 Materials and methodology

This chapter presents all methods used in this project. As the main focus of this project is to understand the evolution of the URS, the focus of this study is mostly based on geomorphological and morphostructural mapping. Structural mapping was conducted in order to produce structural maps and profiles (and kinematic analysis). Satellite InSAR data was used to estimate displacement of the active area. A sediment core from one of the avalanche-dammed lakes was collected in order to find a minimum age of previous rock avalanches from radiocarbon analysis.

2.1 Geological mapping and data collection

2.1.1 Fieldwork

Skredkallen and its surrounding areas was investigated for 2 weeks in August 2018, one day in November 2018 and one day in March 2019. All fieldwork was assisted by concurrent masters student Leif Trønnes. The first three days in August was carried out together the supervisor and co-supervisor. The purpose of the fieldwork was to conduct geological and geomorphological mapping of the area.

The deposits below Skredkallen were visited again in November, together with the supervisor and PhD candidate Lis Allaart. The geomorphology of the area was investigated in greater detail.

A coring trip was carried out in late March 2019. The coring trip was assisted by the supervisors, master student Leif Trønnes and PhD candidate Lis Allaart. The purpose of the trip was to obtain sediments from a lake on the avalanche deposit, during the winter when the lake surface was frozen.

2.1.2 Geological mapping

Morphostructural and structural mapping was conducted for the upper part of the slope (source/active area). A total of 436 foliation measurements and 704 joint measurements were obtained during fieldwork, including both in-situ and displaced bedrock. Not all outcrops in the source area could be visited due to inaccessible terrain. As a result, fieldwork was mostly limited to the upper part of the URS and along the back scarp. A total of 11 localities were visited along the back scarp. Measurements were distributed over a 10 m horizontal distance at each locality. Geomorphological mapping was done for the lower part of the slope (depositional area). Geomorphological and morphostructural mapping was done by

identifying and describing elements in the field, and analysing field and aerial photographs. Field observations were mainly concentrated in and around the rock avalanche deposits. Observations include block sizes and concentrations, ridges and depressions, amount of finer material (sand, silt etc.) and vegetation cover. A number of sedimentary profiles were dug to distinguish rock avalanche deposits from other types of deposits, such as moraines, till and eolian sand. Assumed upper limits of raised shorelines were mapped by GPS tracking. Analyses of DEMs and stereoscopic imaging also proved helpful for geomorphological mapping. Field photographs were captured by smartphones. A DJI Inspire drone was brought for capturing aerial photographs both for photogrammetry and geomorphological mapping. The drone proved to be very helpful for mapping as significant parts of the unstable area could not be accessed in a safe way. A total of 1449 photos and 9 videos were obtained, covering most of the study area.

For structural mapping, multiple measurements were taken at each of the 57 localities (Figure 27), assigned a GPS point using a Garmin Etrex 30x. Structural measurements were made using both compass and smartphone. Compass measurements were made using a Silva compass and the “right hand rule” technique. Smartphone measurements were made by using the FieldMove Clino application on a LG G4 android phone. The smartphone compass was calibrated and controlled for any inaccuracy by comparing it to conventional compass measurements. Every tenth measurement was obtained with a conventional compass to detect any inaccuracy in the application.

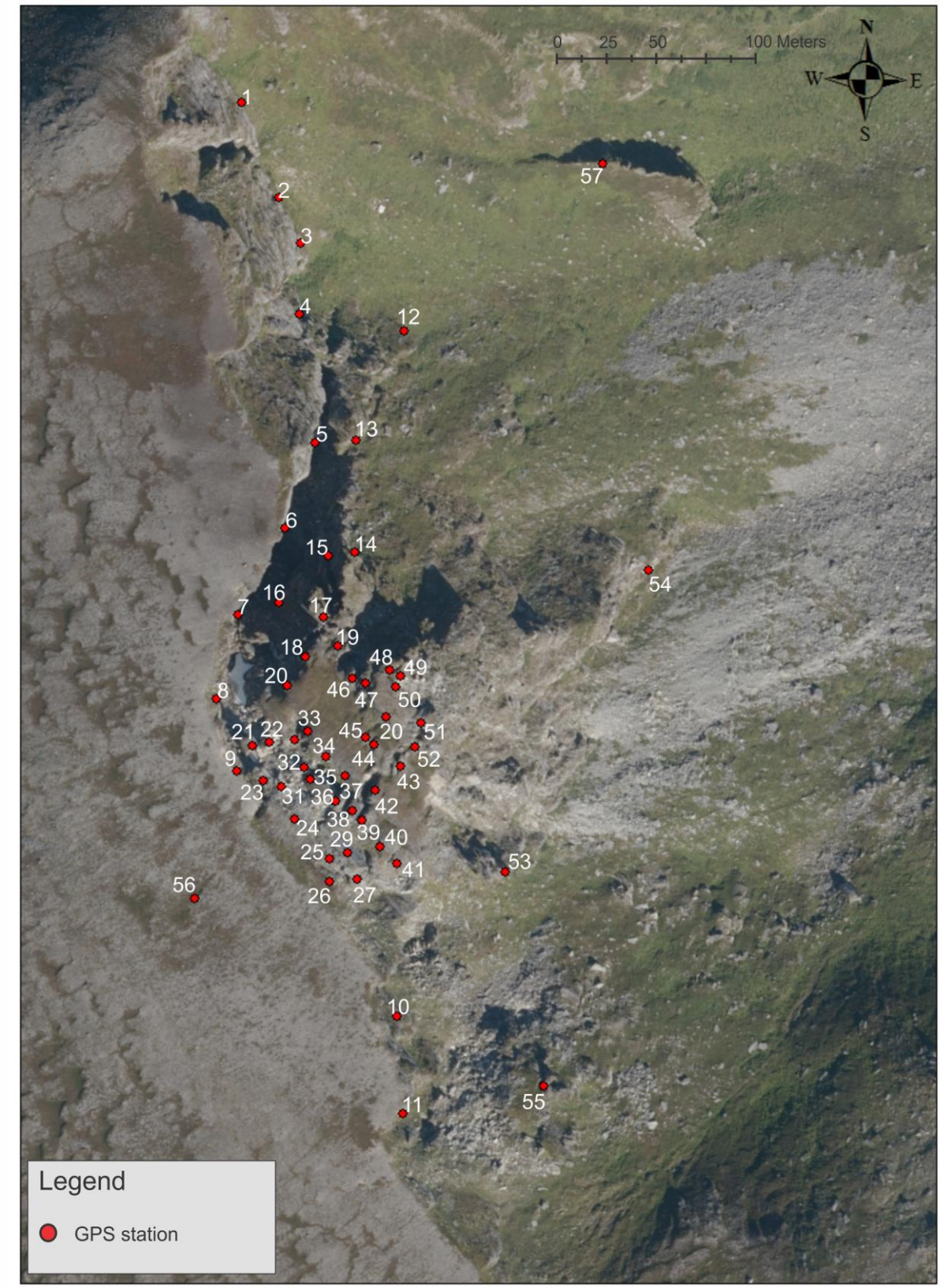

Figure 27: Overview of localities where structural measurements were taken. Orthophoto obtained from (Kartverket, 2019).

2.1.3 Dips 7.0

Dips 7.0 is a software by RocScience for analysis of orientation data. The projects structural data stereographically.

Dips 7.0 was used in this study for structural analysis. The structural data are presented in an equal area projection, lower hemisphere, equal area and by fisher distribution. In this study, structural data is presented in strike/dip with right hand rule. A total of 304 measurements were used in the structural analysis. The foliation and joint sets were defined by using one standard deviation variability cone. On the colour plot, the density is set between 0 – 9.3%, where darker colors represent high values and light colours low values.

2.1.4 ArcGIS

ArcMAP is a geographic information system by ESRI. Version 10.5 was used for this study for structural and geomorphological mapping. Digital Elevation Models (DEMs) were extracted from the ArcticDEM, orthophoto and contour lines were uploaded from Kartverket (2019) and all data was georeferenced. These datasets were used to visualize and illustrate the study area in GIS.

2.1.5 Lake coring

Sediment coring was conducted to retrieve organic matter for radiocarbon age dating of the avalanche deposits. A lake determined to have formed after the deposit of the (last) major rock avalanche event was chosen, as sediment dated from the bottom of this lake will reflect the period of time following the avalanche deposit.

Coring involved drilling through the ice with an ice drill, and extracting sediments from the deepest part of the basin using a Russian corer. The corer was pushed as far down into the sediments as possible, locked and brought to the surface. A core of approximately 60 cm was successfully retrieved. An attempt was made to collect more sediment cores, but the substrate was very hard and the corer was damaged during the second attempt. The sediment core was stored in a plastic tube, secured with floral foam and covered in plastic wrap for protection and preservation during travel and storage.

2.2 Sediment dating

The sediment core was sampled for organic material in the lab at UiT. All lab work was assisted by the co-supervisor. Four samples were extracted from different depths of the core. Two samples were extracted from the lowermost part of the core (58-57 cm depth and 56-55 cm depth) to provide a minimum age of lake formation, and one from middle (40-39 cm

depth) and upper part (24-23 cm depth; Figure 28) to evaluate the stratigraphic order of the sediments. The samples were extracted by cutting out a cube of approximately 1-2 cm^3 of material. All samples were washed through a 250 µm sieve to remove most non-organic and fine material. The remaining material was investigated under a stereo microscope, where suitable samples for ^{14}C dating was collected. For the three lowermost samples (58-57 cm, 56-55 cm and 40-39 cm), mostly mosses, and some leaves were collected for dating. For the uppermost sample, leaves were used for dating. The samples were dried for 1-2 days at 40°C. Then they were weighed and wrapped in aluminum foil for shipping. The samples were sent to The Tandem Laboratory at the Uppsala University for accelerator mass spectrometry (AMS) ^{14}C dating.

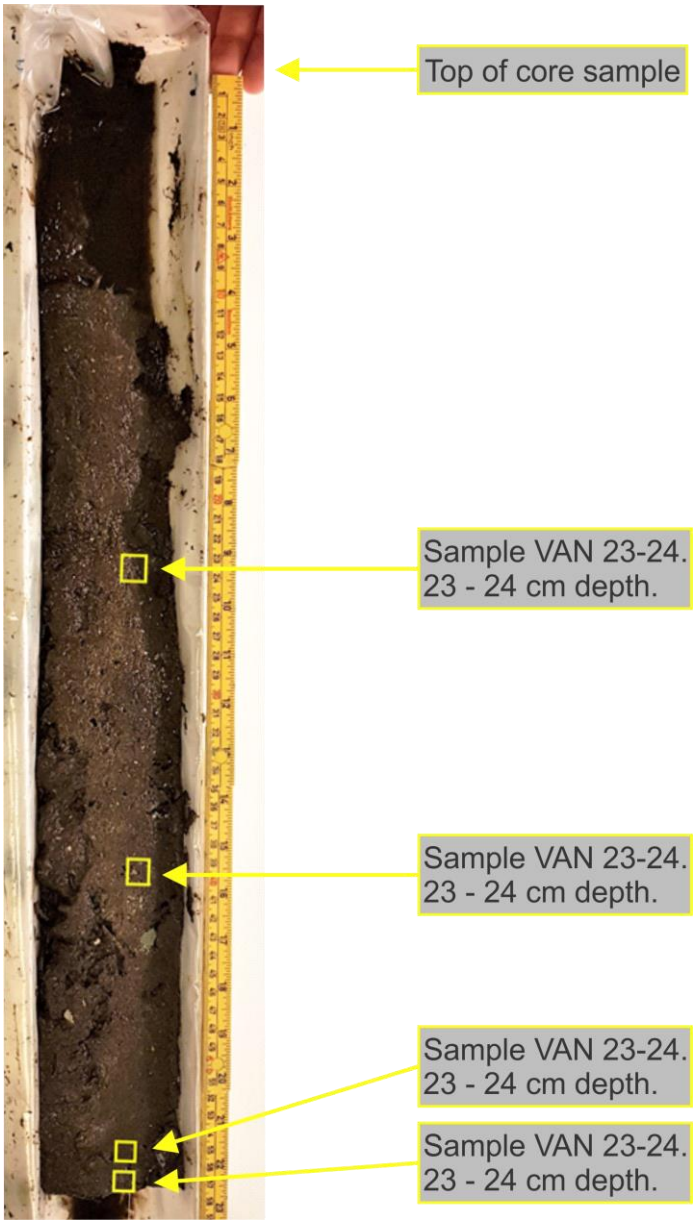

Figure 28: Position of samples extracted from core for ^{14}C dating.

2.2.1 OxCal

The OxCal program is an online software by the University of Oxford intended to provide radiocarbon calibration and analysis of archaeological and environmental chronological information. Version 4.3 (Ramsey, 2009, Bronk Ramsey, 2013) and the IntCal13 (Reimer et al., 2013) dataset were used in this study in order to convert ^{14}C ages to calibrated years before present (cal. yr BP; BP = AD 1950). All calibrated ages are presented as calculated mean values using the 95.4% probability ranges.

2.2.2 Rbacon

R is a software environment for statistical computing and graphics. It provides a wide variety of statistical and graphical techniques. For this study, Bacon (v. 2.3.3; Blaauw and Christen, 2011) and R x64 (v. 3.4.3; R. Core Team, 2017) were used in order to create an age-depth model for the dated sediments. The age-depth model was made by importing a csv file with the ^{14}C ages and uncertainties into the software. An accumulation rate of 20 cm a^{-1} were chosen to best fit the probability curve calculated by the software.

2.3 Volume estimations using the Scheidegger equation

An empirical relationship between the runout distance and the height difference divided by the volume of deposits was found by Scheidegger (1973). The height difference (H) divided by the runout length (L) equals the tangent of the angle of reach. The angle of reach is illustrated in the equation below.

$$\tan \alpha = \frac{H}{L} = 10^{0.62419} \times V^{-0.15666}$$

The Scheidegger curve suggests a logarithmic relationship between the H/L ratio (or the angle of reach) and the volume (shown on Figure 29), resulting in a decrease in the angle of reach with an increasing volume (Scheidegger, 1973, Corominas, 1996, Oppikofer et al., 2016). Data from historic rock avalanches in Norway, mapped by Blikra et al. (2001) are included in the figure, indicating that the Scheidegger curve is conservative. This is clearly shown on Figure 29 where more than 90% of Norwegian events have shorter run-out distance than predicted by Scheidegger (1973).

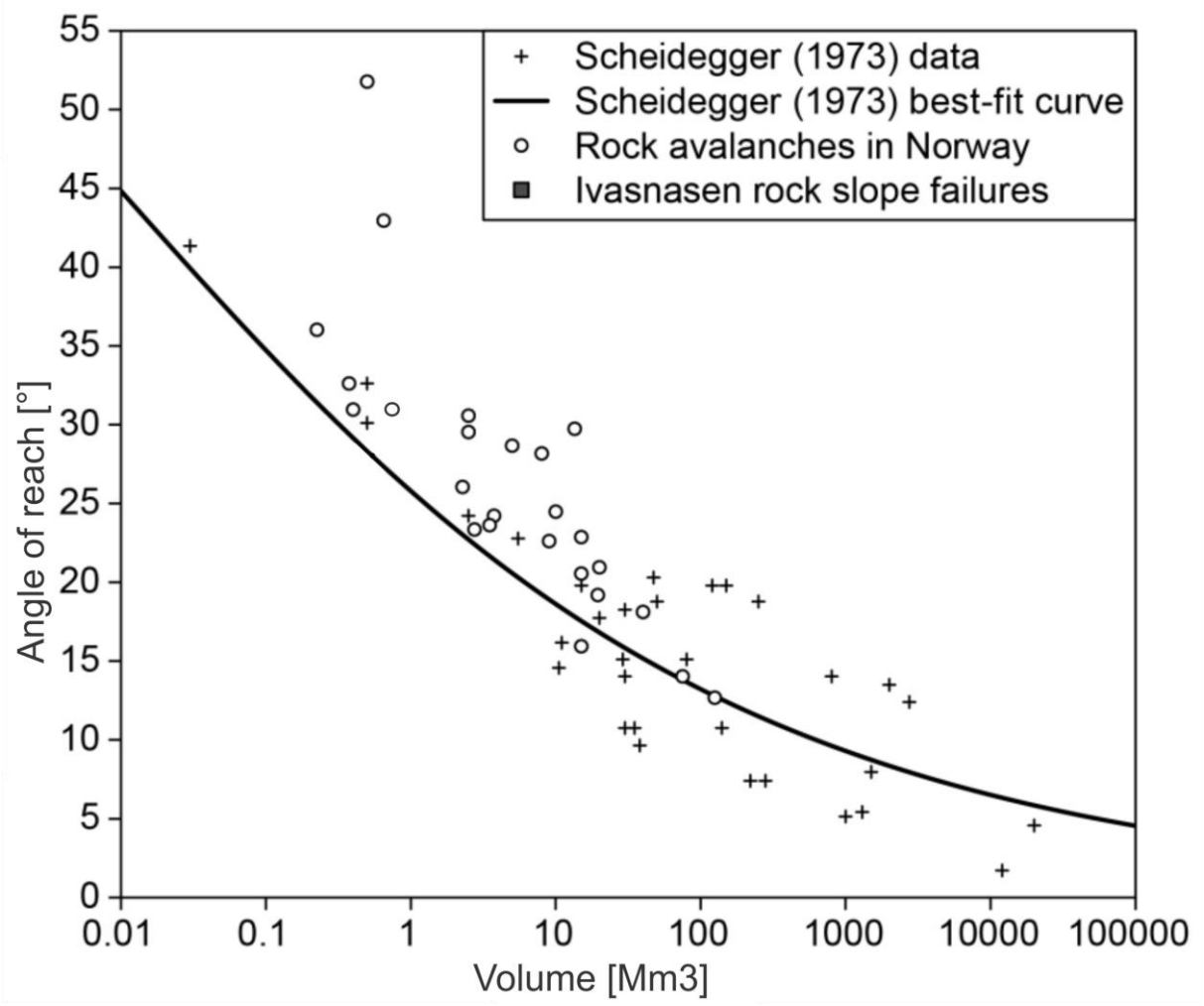

Figure 29: Empirical relationship between the angle of reach of a rock avalanche and its volume based on the inventory by Scheidegger (1973). Data from Norwegian rock avalanches are plotted as dots. Modified after Oppikofer et al. (2017).

By measuring the height difference and run-out distance of the historical rock avalanche deposits, the Scheidegger formula was modified in order to calculate the volume of previous rock avalanche event(s). The modified formula for calculating the volume of previous events was:

$$V = \left(\frac{\frac{H}{L}}{10^{0.62419}} \right)^{\frac{-1}{0.15666}}$$

2.4 InSAR: Satellite-based radar

Interferometric Synthetic Aperture Radar (InSAR) is a method for detecting and measuring displacement over time. The method is based on comparing synthetic aperture radar (SAR) image pairs. SAR is a space born instrument imaging the earth from above. SAR orbits the earth in an N-S or S-N direction (the azimuth direction). SAR data is organized in radar coordinates, range and azimuth. Range is the distance from the radar to the measured ground (Figure 30). Azimuth is the distance along the radars flight path (Eriksen, 2013). As the radar orbits the earth, radar beams are being sent and received in a sideways direction (Line of sight). The position of pixels is recorded by the range and azimuth direction, calculated from the satellites own position. The range direction is given by timing the return of the reflected echo of the beam. The azimuth direction is resolved by Doppler spread. This is a technique where reflected echo from objects in front of the satellite are being compared to objects behind the satellite (Rosen et al., 1998, Eriksen, 2013). The radar coordinates are converted into map coordinates by a method called geo-coding. The radar is ascending as its orbiting from the South Pole to the North Pole, while it is descending as it orbits from the North Pole to the South Pole (Figure 31; Eriksen, 2013).

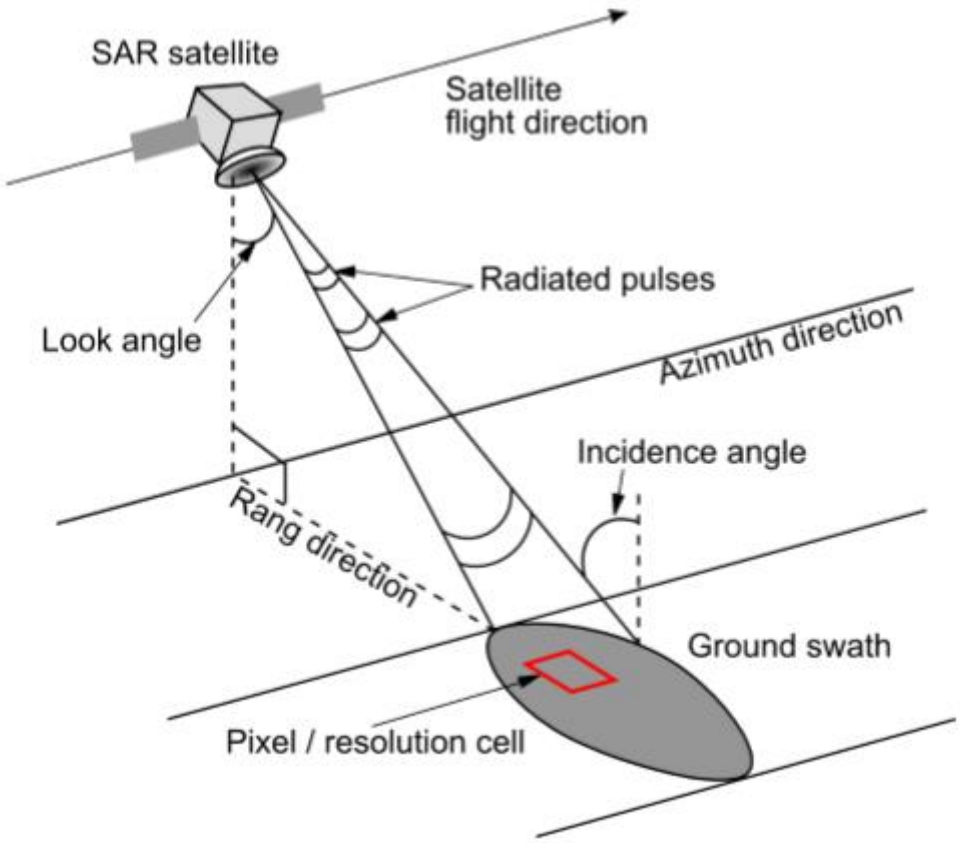

Figure 30: Geometry of a Synthetic Aperture Radar (SAR) system. Modified by Eriksen (2013) after Lauknes (2011).

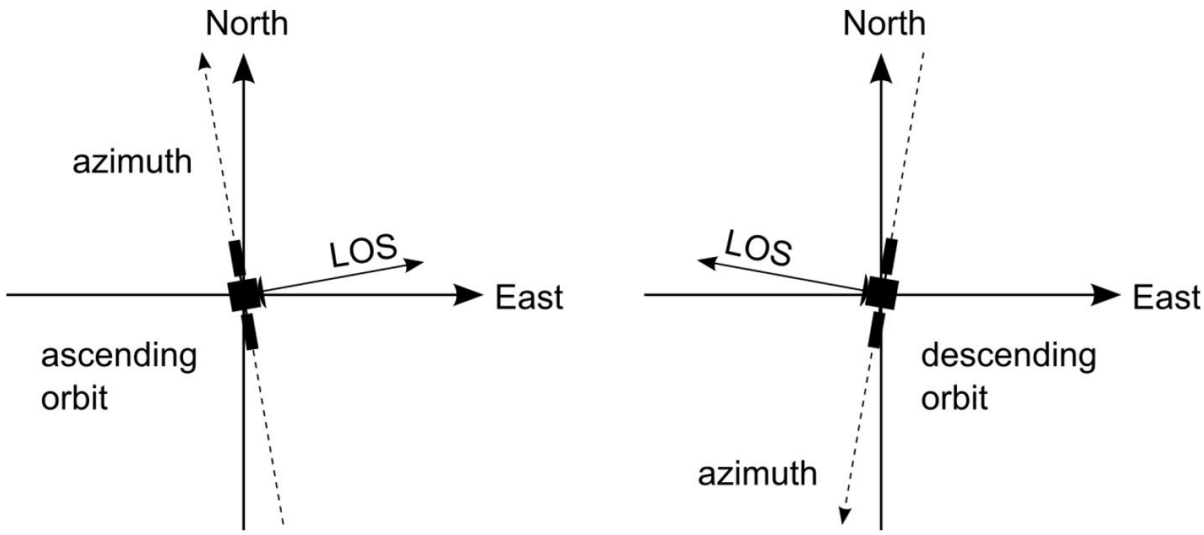

Figure 31: Illustration of the azimuth and LOS for ascending and descending satellites. From Eriksen (2013) after Lauknes (2011).

Interferometry is a technique where SAR images are combined to produce an interferogram showing the difference in phase (interferometric phase). Electromagnetic pulses are sent out, with a certain wavelength and amplitude. A shift in phase is referred to as phase contribution. A phase contribution could indicate surface displacement, if the displacement has occurred between two flyovers. A number of other reasons may cause phase contribution, which has to be accounted for (subtracted). There reasons include small changes in satellite position for the different flyovers, with a following difference in topography, and a difference from atmospheric path delay.

The Sentinel-1 satellite was used, which has a repeat cycle of c. one week. InSAR imagery was acquired from InSAR Norge (NGU, 2019a). Two ascending and descending tracks have been used as the polar location of Troms means that they overlap. The datasets cover the summer months between July 2016 and September 2018, making it a useful tool for displaying the current movement rates. The InSAR data assumes a linear displacement from around November to June every year as no data is available due to snow cover. The ascending lines are used in this study, as they have LOS down towards ENE, which aligns with the expected movement of the URS at Skredkallen.

3 Results

This chapter outlines the results of the study, including geomorphology of the area and the rockslide, lithology, structural analysis, InSAR analysis, and investigation of the deposit.

3.1 General geomorphology

This chapter presents the overall morphology of the study area. The geometry and appearance are illustrated in Figure 32. The morphological elements are presented in Figure 33.

The mapping area is crosscut by a NNW-SSE-trending ridgeline, Laukvikfjellet, which slopes from 480 m asl down to the east at 35° and down to the west at 25°. The eastern slope flattens out at c. 50 m asl and slopes gently down to the sea at c. 10° (Figure 32).

The uppermost part of the western slope is characterized by a gentle slope (ca. 10°) with a thin cover of weathered bedrock. The slope gradually steepens downslope to an angle of up to 30°. Further downslope, the surface cover appears gradually more affected by solifluction. The solifluction lobes are observed down to an elevation of 370 m asl. Below this the slope angle ranges from 25 - 35° and the ground becomes more vegetated. There are some outcrops of bedrock in steeper sections. Under 200 m asl, the slope gradually flattens out towards Skipsfjorden, where the lowest 50 m asl slopes at <10°. From 200 m asl to 50 m asl, the slope is mostly covered by forest. The lowermost c. 50 m asl consists of raised marine sediments covered by peatland.

The E-facing slope has a steeper character than the oppositely facing slope. From the highest point of Laukvikfjellet (477 m asl) and down to c. 150 m asl, the slope is dipping 40°, and covered by a thin layer of grassy vegetation. Some subvertical outcrops of bedrock are found in the uppermost 100 meters. At 150 m asl, the slope flattens to a 20-25° slope angle. This area marks the toe of the mountain ridge. A thick cover of talus follows the toe of the ridge and covered by a thin vegetation layer (Figure 34). At c. 50 m asl, the slope flattens out gently towards the sea in a platform of raised marine sediments, some outcrop ridges and peat. The platform between the toe of the eastern slope and the sea is characterized by a series of marine terraces/raised shorelines of both rock and sand deposits. The outcrop ridges appear perpendicular to the shorelines. A series of small streams are found beneath the toe of the ridgeline and flow across the platform. S of Skredkallen, the streams end up in Laukvika bay in a sandy beach zone. In the area N of Skredkallen, the streams connect several small lakes.

The Laukvikfjellet ridgeline is crosscut by a NE-SW-striking lineament (herewith termed the Skipsfjord-Slettnes Fault) which shows some offset and defines the northern boundary of the rockslide (Figure 33).

Overview of the unstable area and deposits

A 1.2 km backscarp is located along the top of the ridgeline, with a steep fall towards E (Figure 33). Roughly 400 m of the middle part are characterized as the currently active backscarpv which detatches the unstable area from the bedrock. The unstable area at Skredkallen is located between 270 and 470 m asl. The backscarps give way to a flat terrace/paleosol and delimited at the front by vertical cliff faces. There is no distinct toe in the lower slope. The backscarp is easily observed both in the field and on aerial photos as a distinct change in shape along the NNW-SSE trending mountain ridge. The unstable area is comprised of a system of moving blocks, terraces and fractured rock material and is characterized by a series of scarps, columns and lineaments. Areas of multiyear snow and ice are present within the unstable area. A detailed description of the unstable area follows in section 3.2.

Below the unstable area a series of bouldery rock avalanche deposits stretch from the assumed base of the rockslide to the NE for 1.4 km. The deposits are stacked, with lobes nearest the rockslide appearing fresh with only a thin layer of vegetation cover in a few places. Lobes stretch out from several release areas within the unstable area of the rockslide. Beyond these fresh deposits, large lobes of bouldery deposits stretch out onto the plateau in a series of ramps. This area contains very large blocks and is far more vegetated than the upslope deposits. The thickness of the deposit declines towards the distal parts, however the size of the blocks does not. The block sizes and morphology of these deposits are described in more detail in section 3.5.2. Surrounding the unstable area in the E-facing slope is evidence of previous RSF activity, visible in the field as a thin cover of rock avalanche deposits and debris flow levees.

The deposits are separated from the marine sediments on the plateau by a sharp front, visible in the terrain as a distinct rise in elevation from the marine sediments. Some areas along the most distal deposits appear to be affected by erosion as they appear to be washed out and are described in detail in section 3.5.2. Some small areas of massive, fine grained sand can be found to the S and E of the deposits. The details about these sediments are described further in section 3.4.3. Some outcrops of weathered bedrock are also present in this area. These

outcrops are most common in the upper (upslope) parts of where the sediment cover gets thinner.

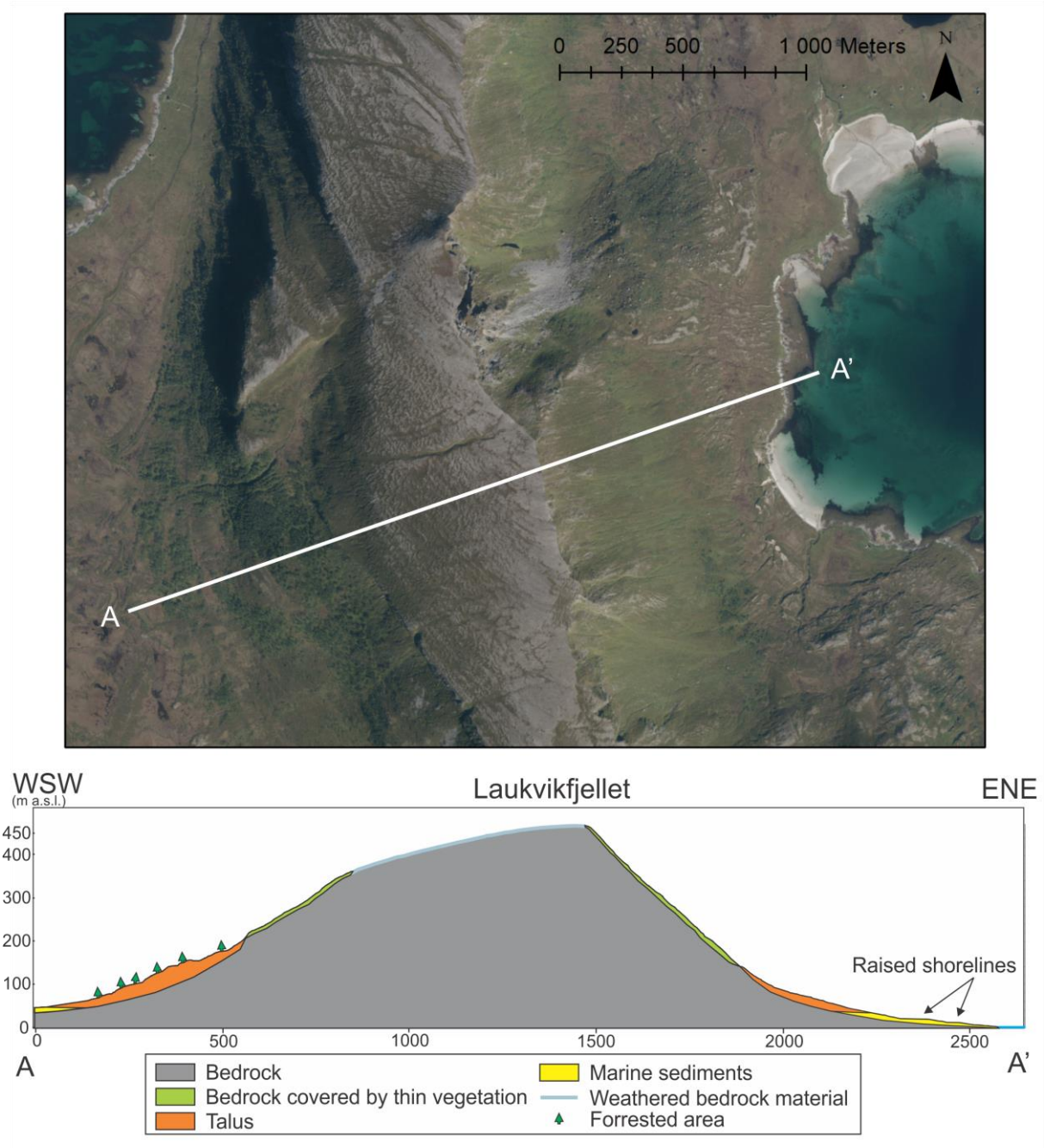

Figure 32: Simplified elevation profile through the study area, just S of Skredkallen as shown on the attached map. Note the distinct difference in dip between the E and W facing slopes. Orthophoto obtained from (Kartverket, 2019).

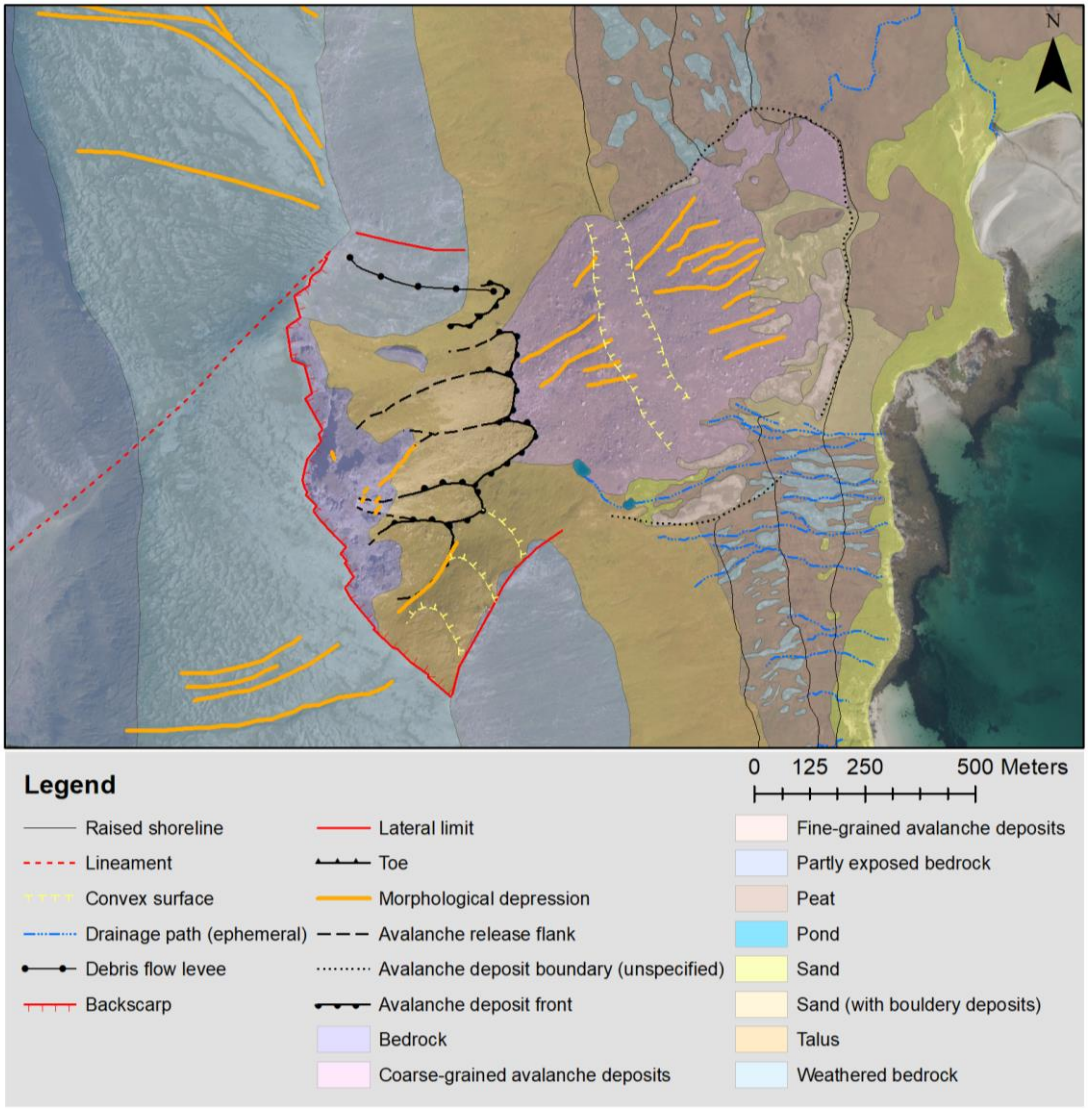

Figure 33: Overall geomorphological map of the study area. Orthophoto obtained from (Kartverket, 2019).

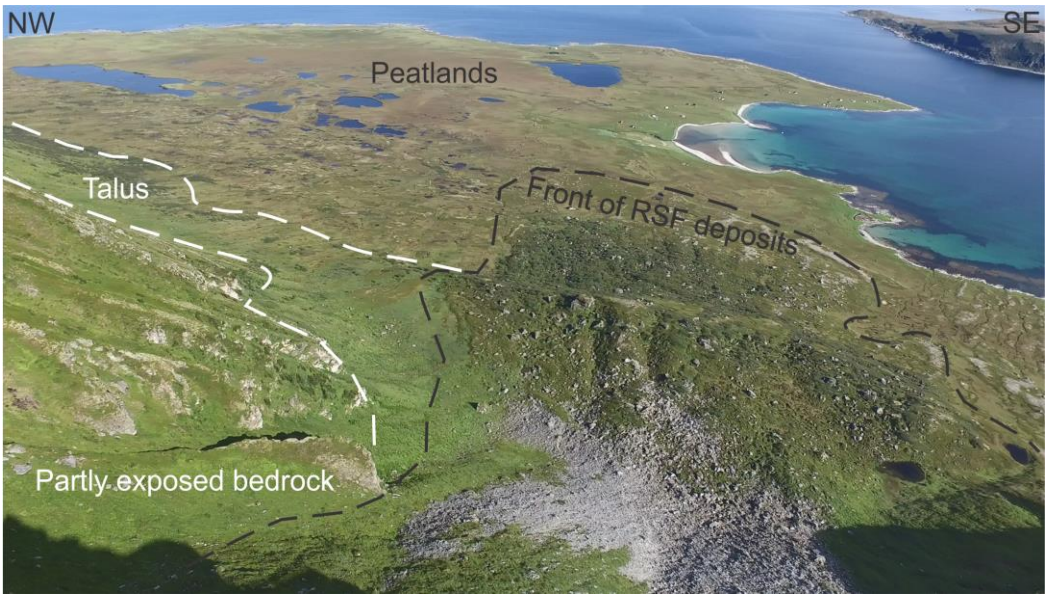

Figure 34: Drone photograph from August 2018 illustrating the geomorphology outside the front of the RSF deposits. Black dashed lines show the front of the RSF deposits, while white dashed lines show the talus zone.

3.2 Geology and geomorphology of the URS

This chapter describes the morphological elements and morphostructures of the active unstable area, presented in Figure 35.

Three sets of scarps striking NW-SE, NNE-SSW and NE-SW delimit the URS at the western edge. Opening on the NE-SW and NNE-SSW-striking scarps has resulted in a trench <25 m wide and <100 m deep (Figure 36). Sliding on the NW-SE-striking scarp has resulted in an offset of the terrace from the ridge of c. 25 m. The backscarps comprise three sets of zig-zagging subvertical structures striking NW-SE, NE-SW and NNE-SSW (Figure 37). The zig-zag structural pattern is visible in the field as NW-SE and NE-SW striking subvertical cliffs and NNE-SSW striking cliffs in the northern part. The interaction between the NW-SE and NE-SW sets has resulted in several detached, rectangular terraces above the unstable area.

The most dominant backscarp orientation is NW-SE striking. This structural set makes up the longest segment. However, only c. 2 m of bedrock is exposed along the NW-SE striking backscarp. The NW-SE striking set was observed in field with a steep dip towards NE. North of the unstable area, the NW-SE striking set make up subvertical segments of cliffs, displaying heights of up to 100 meters.

The NE-SW segments are the second most dominant set of backscarps. Together with the NW-SE striking set, these two make up the zig-zag shaped patterns which are found along the top of Laukvikfjellet ridge (Figure 37). Together with the NNE-SSW striking set, the NE-SW set results in an NE-SW trending opening towards the unstable area. A SE tilt of the adjacent block results in a vertical cliff along the two backscarps of up to 100 meters.

Unlike the two other sets of backscarps mentioned above, the NNE-SSW striking set is mainly exposed along a trench which flanks the NW part of the unstable area (Figure 36) and is further described in section 3.2.5.

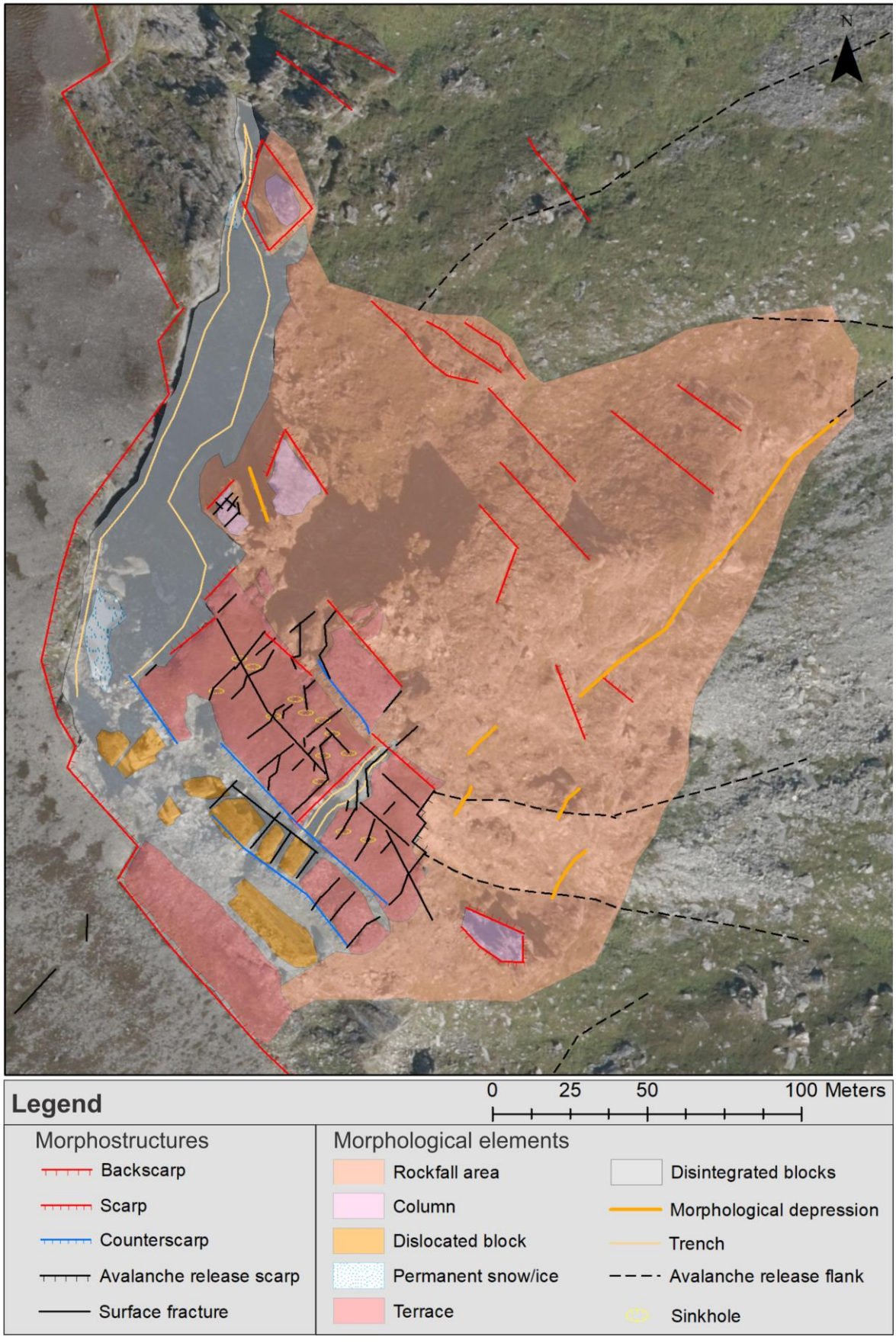

Figure 35: Overview of geomorphological elements and morphostructures in and around the unstable area. Orthophoto obtained from Kartverket (2019).

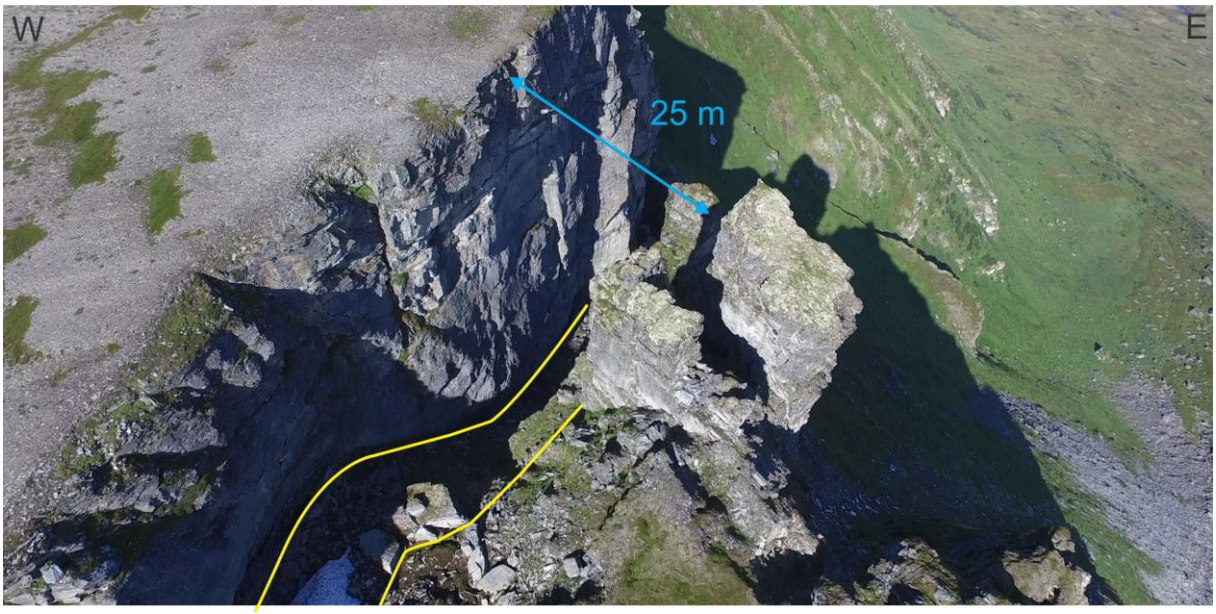

Figure 36: Drone photograph from August 2018 showing the largest opening along the NNE-SSW set of the backscarp. Yellow lines show the trench as a result of the opening.

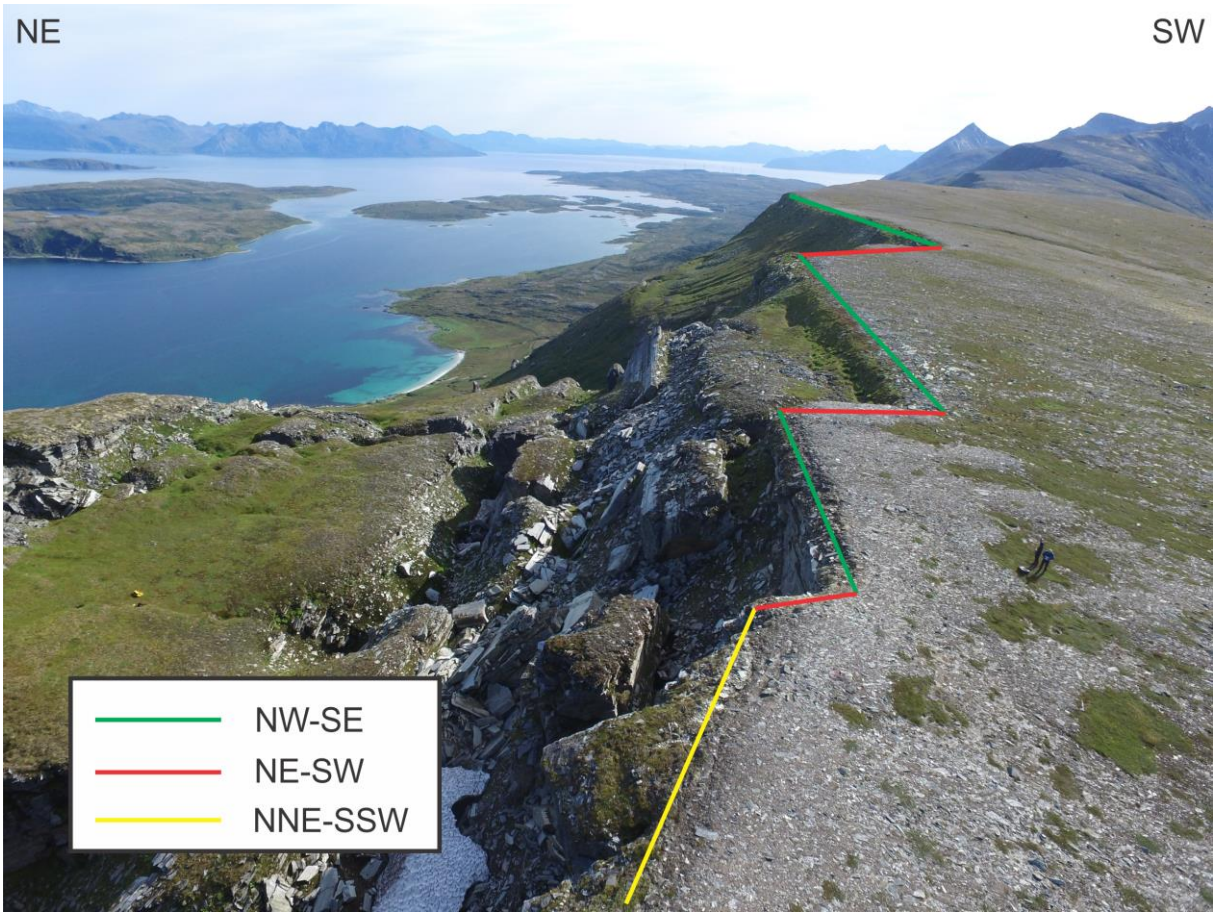

Figure 37: Drone photograph from August 2018 illustrating the different orientation of the backscarps.

3.2.1 Scarps

The unstable area is crosscut by multiple scarps. The scarps delineate the URS into several terraces and displaced blocks and form release flanks on the outermost parts. The NW-SE striking scarps have a similar orientation as the main back scarp as they also dip towards NE, and comprise the most dominant set of scarps in the unstable area. The scarps are mostly found along the northeastern part of the unstable area.

The NE-SW striking scarps are most distinct in the southern part of the unstable area and have a steep dip to the SE (Figure 38). The most prominent of these crosscuts almost the while unstable area. Opening along this scarp has resulted in a NE-SW striking trench, separating the two largest terraces. The opening of the crosscutting trench results in a forward tilt of the southern part of the unstable area. Along the southern flank of the southern terrace, a NE-SW striking avalanche release scarp is present. This scarp differences from the other scarps by the appearance. It appeared during fieldwork as a fresh “scar” along the southern flank.

A series of NE-SW striking scarps are located along the northern flank of the unstable area. These scarps are subvertical and flanks the unstable area including Kallen to the main trench.

3.2.2 Counterscarps

Scarps displaying a sliding sense of movement and an opposing dip to the backscarp, are marked as counterscarps. The counterscarps mapped on Skredkallen has a NW-SE orientation, which display a similar strike as the NW-SE striking scarps and backscarps, but has a steep dip towards SW. The most distinct counterscarps are found along the southwestern flank of the main terrace and along the southwestern side of the outermost terrace (Figure 38). This has resulted in a graben-like topography of the unstable area, where the central part is the most down-dropped.

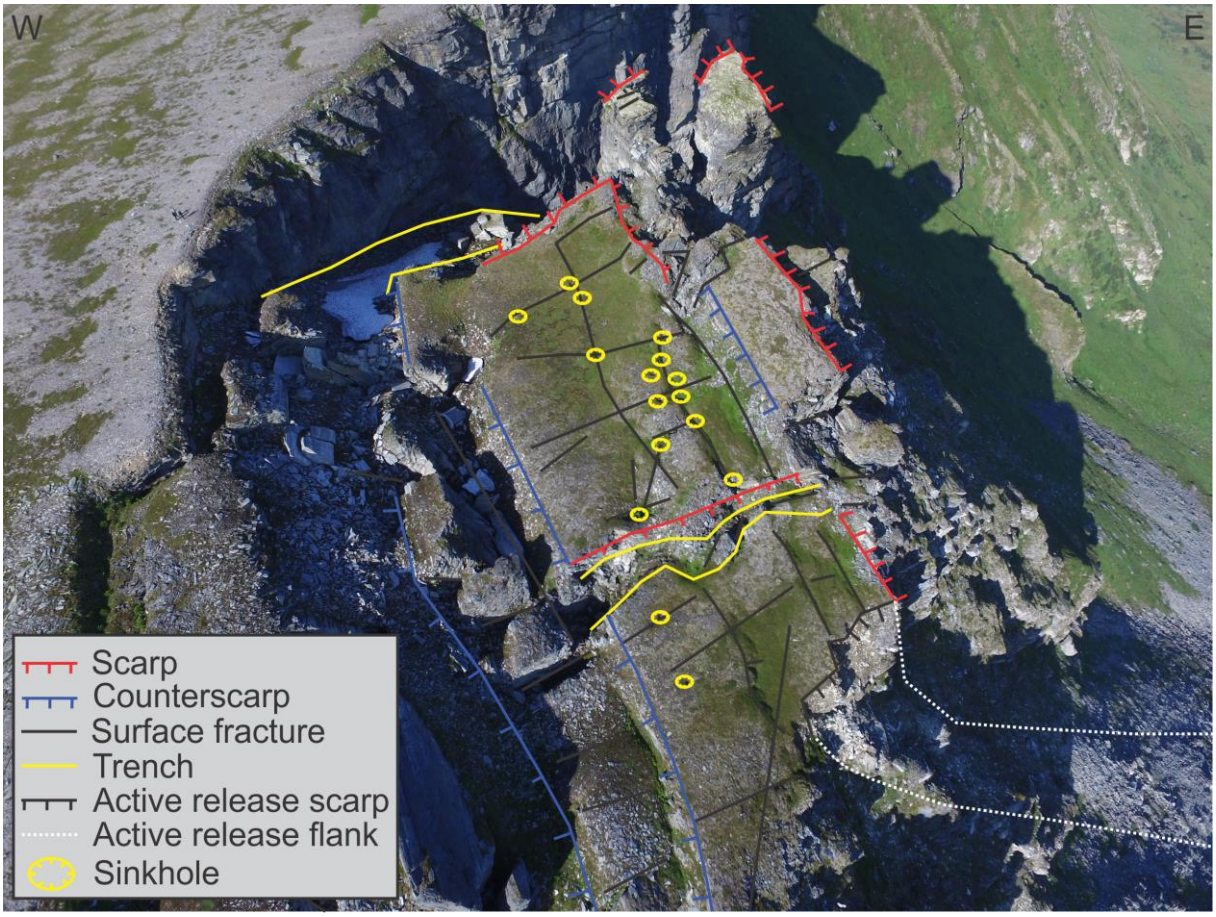

Figure 38: Drone photograph from August 2018 giving an overview of morphostructures and morphological elements within the URS.

3.2.3 Dislocated and disaggregated material

The rockslide comprises a system of moving dislocated blocks. The block surfaces display terraces. They are separated from the in situ bedrock by scarps and trenches, but they are not disaggregated (Figure 39 A). The central terrace of the URS is subsided relative to both the outermost terrace and the inner terraces, forming horst/graben complex (Figure 39 B), defined by NW-SE striking scarps and counterscarps (Figure 35). The elevation of the central graben is 454 m asl, about 5 – 10 meters lower than the outermost horst. The terraces show signs of deformation from a network of surface fractures which were visible in the field as morphological depressions in the vegetation cover (Figure 35). The intersections of these fractures create distinct sinkholes in the topography (Figure 39 C). The surface fractures are described in further detail in section 3.2.4.

Figure 39 Field photographs from August 2018. A: Example of a displaced terrace separated from the in situ bedrock by a NW-SE and a NE-SW striking backscarp. B: Example of a sinkhole in the main terrace. C: Picture showing how the main terrace is downdropped relative to the outermost terrace, creating a horst/graben geometry in the unstable area.

Between the main terraces and in in situ bedrock are masses of smaller dislocated blocks and dissagregated material (Figure 40). The blocks are distinguished from terraces by their lack of vegetation, small size and random orientation. Most blocks are located between the central terrace of the URS and the NW-SE back scarp, but smaller disaggregated material are also found between the unstable area and the NE-SW striking backscarp (Figure 41 A). In terms of geometry, most blocks show either a rectangular, rhombus or trapezoid shape (Figure 41 B). The rectangular blocks are shaped by the orthogonal joint sets, while the rhombus- and trapezoid shaped blocks are shaped by oblique sets.

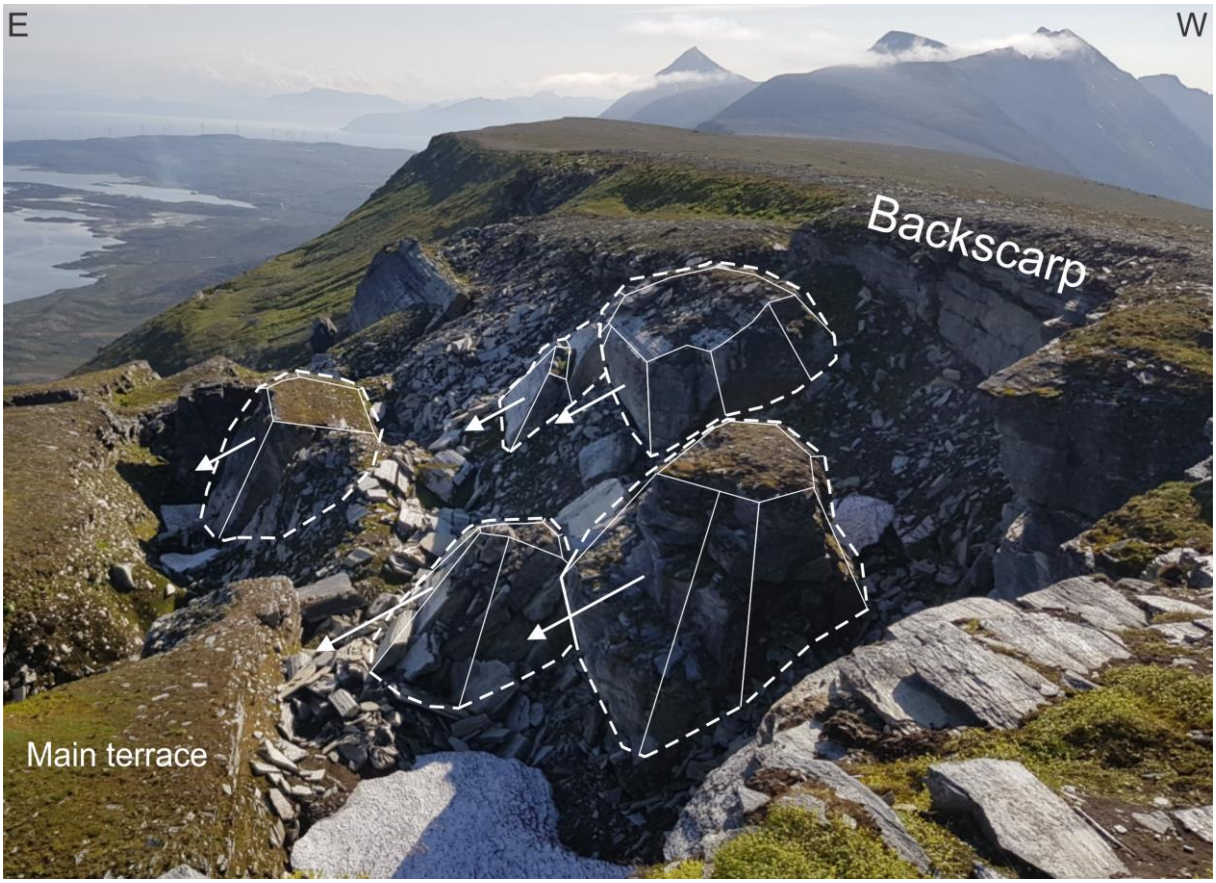

Figure 40: Field photograph from August 2018 illustrating the slide blocks between the NE-SW striking backscarp and the main terrace. Dashed polygons mark the base of active sliding blocks. White lines show the shape of slide blocks. White arrows show the sliding direction.

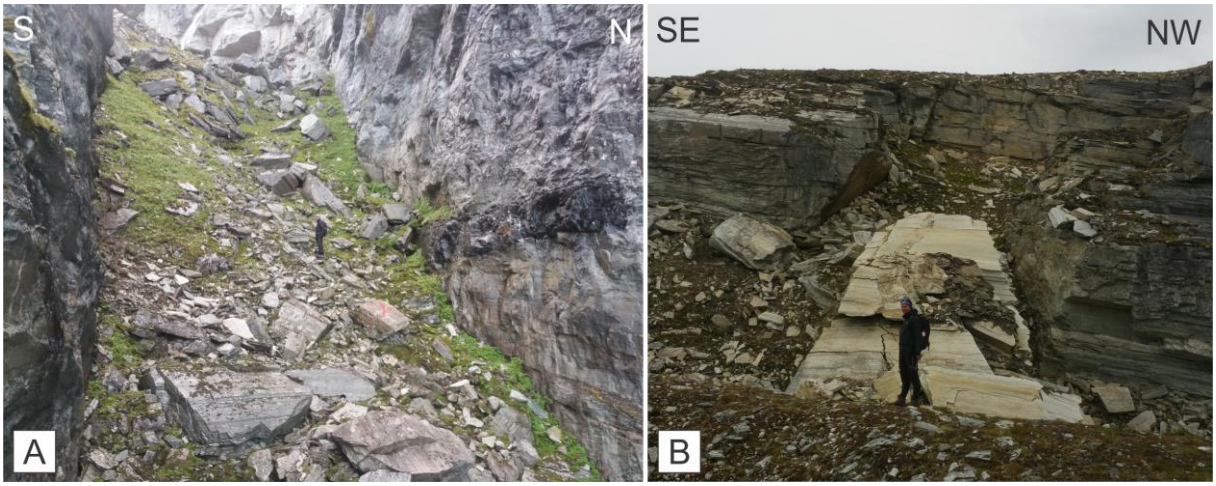

Figure 41: Field photographs from August 2018. A: Disaggregated material between the NE-SW striking backscarp and the unstable area. B: Slide block with a trapezoid shape which has collapsed from the NW-SE striking backscarp.

3.2.4 Surface fractures

Several surface fractures were visible at Skredkallen as morphological depressions in the vegetation cover. These depressions were most distinct in the largest slide blocks and terraces, with a linear and cross cutting geometry and sinkholes at the intersections of the fractures. No or little vertical displacement were observed along these structures. Most surface fractures were observed in the main and southern terrace (Figure 38). The fractures are mostly striking NE-SW and NW-SE. Also, one NE-SW striking lineament are mapped within the in-situ bedrock, with a similar orientation to the fractures in the unstable area. The NE-SW striking fractures aren't as frequent as the NW-SE striking ones, but can be traced up to 100 meters in length. All fractures show striking similarities with the scarps and counterscarps in terms of orientation.

3.2.5 Trenches

The main trench is located between the NE-SW striking backscarp and the SW and NW flanks of the URS (Figure 36). The trench is delimited by NE-SW and NW-SE striking structures of the main terrace. The depth of the trench ranges from a maximum of about 60 meters by Kallen to about 10 meters in the southwestern end. The trench is mostly filled up by fractured blocks and bedrock material, but also some permanent ice are present.

A smaller, NE-SW striking trench (minor trench) is located within the unstable area. The minor trench has an opening of c. 5 m and a depth of 2 – 3 m. The opening along this trench separates the southern terrace from the main terrace (Figure 38).

3.2.6 Permanent snow/Ice

Two areas within the NE-SW striking segment of the main trench have a permanent snow/ice cover. The largest is approximately 300 m^2 and is situated in the intersection of the NE-SW and NW-SE striking backscarps at an elevation of 440 m asl (Figure 42 A) A smaller snow patch is situated in the lower part of the main trench (370 m asl) between the backscarp and a displaced rock column (Figure 42 B).

The permanent snow could indicate that there is permafrost in the URS even though the local area is about 500 meters below the local permafrost zone. The NE-SW striking segment of the main back scarp is shielded from sunlight, and strong winds promote wind-drift accumulation in the sheltered areas. Large snow-cornices were observed during fieldwork in March, creating a great source for snow-accumulation.

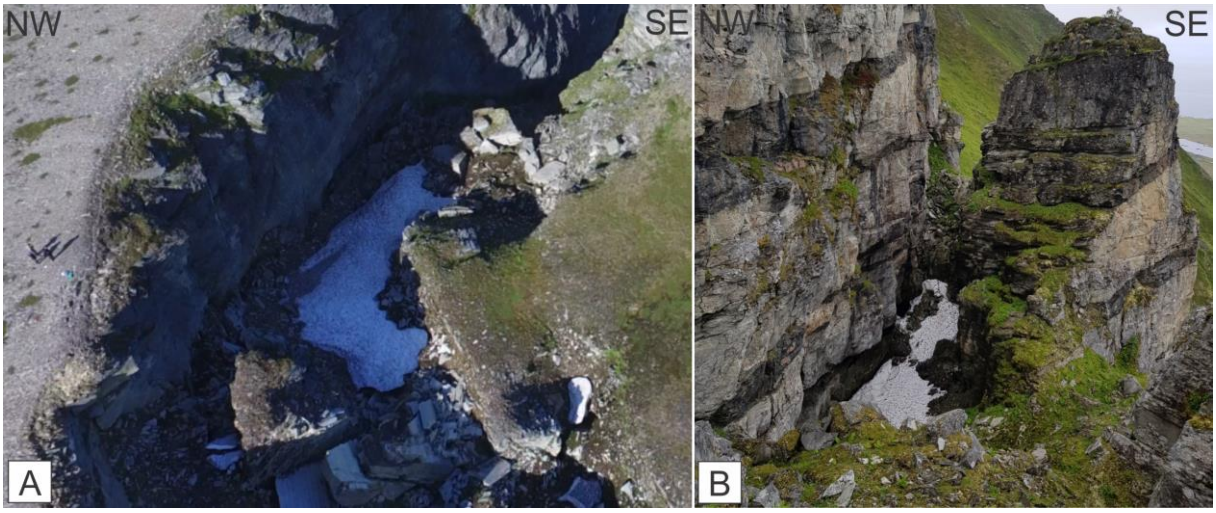

Figure 42 - A: Drone photo from August 2018 showing the largest snow cover in the main trench. B: Field photograph from August 2018 showing the smaller permanent snow/ice between the NE-SW striking backscarp and the unstable area.

3.3 Geomorphology of the Laukvikfjellet slope

3.3.1 Introduction

This chapter describes the geomorphology outside the previously described unstable area. The following descriptions focus on the area that is not a part of the active unstable area, but present key factors for understanding the geological history of the area.

3.3.2 Talus deposits

Evidence of erosion is found along the eastern foot of Laukvikfjellet as talus deposits. The talus deposits appear as a "transfer zone" (termed the talus zone) between the steep E-facing slope and the plateau (Figure 43). The talus deposits appear at an elevation of 115 - 100 m asl and end at 50 – 70 m asl. The material ranges from fine sand to large boulders. The deposits are covered by a thin layer of vegetation and some small areas of forest. The talus zones crosscut by debris flow channels in several places (Figure 44), usually in the vicinity of exposed bedrock and ending in the mid-lower parts of the talus zone. The rockfall paths are visible in the field as distinct depressions in the slope and fade out in the talus zone as small fan shapes. The largest material is found in the middle and lower parts of the talus zone, which is a typical sorting characteristic of talus fans as the largest blocks have the most momentum and therefore travel the furthest. These blocks were easily visible in the field since they were not covered by vegetation.

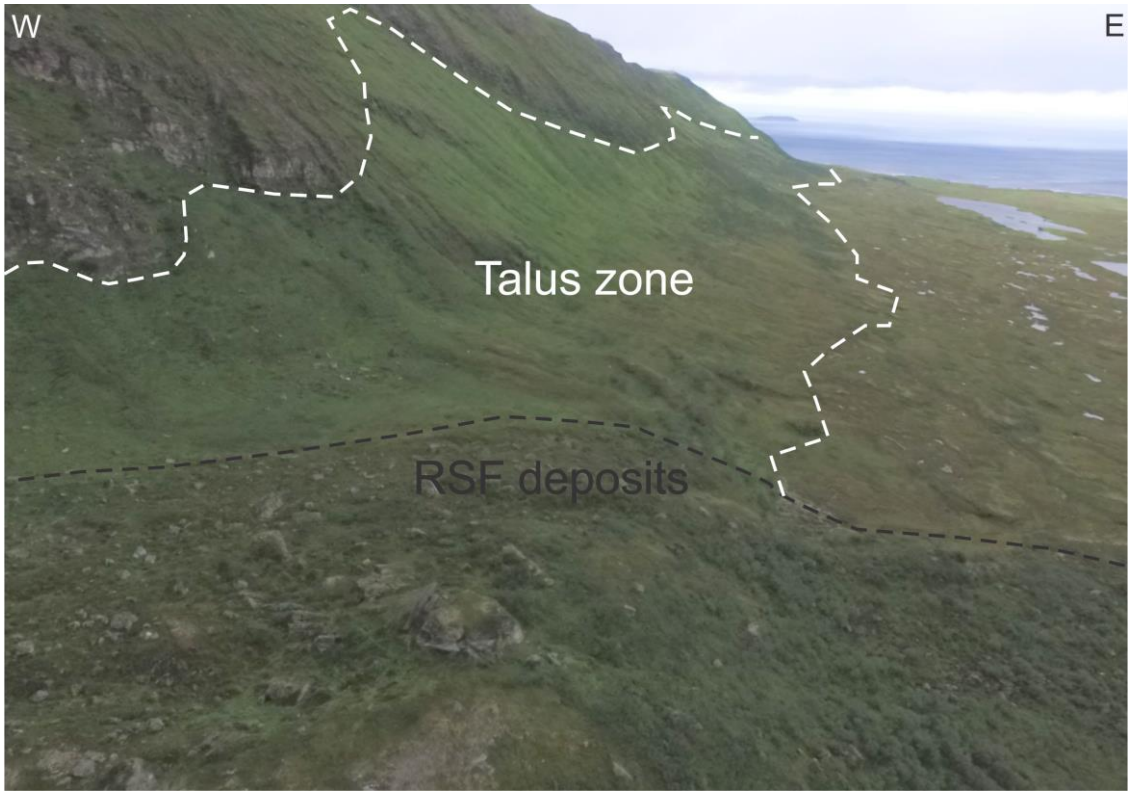

Figure 43: Drone photograph from August 2018 showing the talus zone following the E-facing slope north of the URS. Note the distinct change in slope above and below the talus zone.

Figure 44: Field photograph from November 2018 Illustrating debris flow channels (yellow dashed lines) are cross-cutting the talus zone (white dashed line) along the E-facing slope S of Skredkallen.

3.3.3 Solifluction

The W-facing slope of Laukvikfjellet is mostly covered by weathered bedrock material. The surface is affected by solifluction, evidented by lobes of creeping material stretching in the downslope direction (Figure 45). The solifluction is amplified by the lack of vegetation and by the constant strong winds experienced on the island. The size of the soliflucted lobes are up to 20 meters in diameter and 1 meter in thickness. The soliflucted areas can be traced all the way down to the forested area near Skipsfjorden. Soliflucted areas are also found on the E-facing slope. However these areas are a lot less distinct than the equivalent W-facing soliflucted areas and are only found outside the flanks of the unstable area.

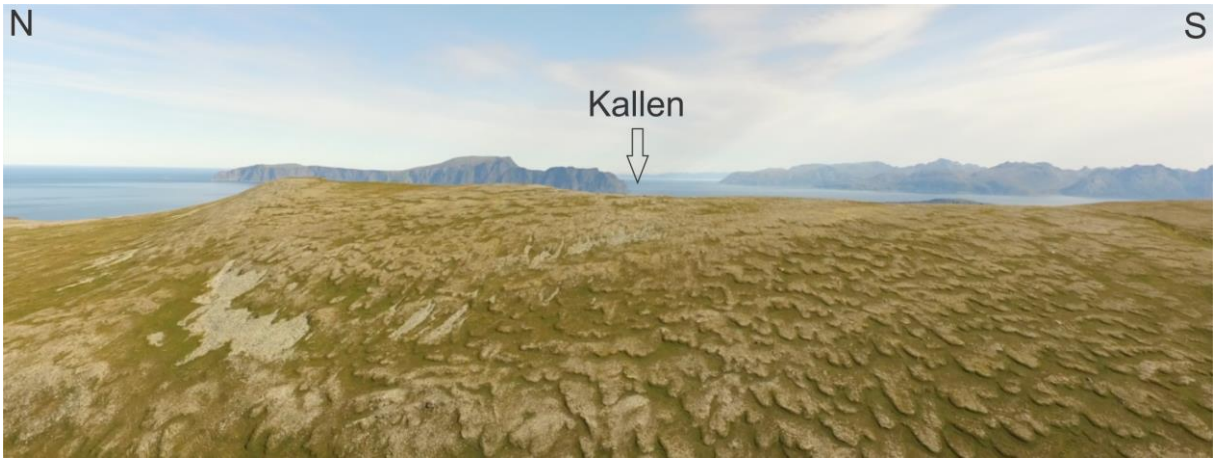

Figure 45: Drone photograph from August 2018 of the W-facing slope of Laukvikfjellet. Weathered material are covering the uppermost part of the slope, while the downslope areas are sandier and vegetated with soliflucted bodies.

3.4 Geomorphology of the low-lying area

3.4.1 Coastline

The coastline in the study area is a part of a small bay, locally named “Laukvika”. The coastline varies between outcrops of bedrock and sandy beaches. The sandy beaches are mainly located where the largest streams meet the ocean. The sandy beaches have a similar composition as the raised marine deposits, consisting of medium grained, massive sand, suggesting a similar depositional environment

3.4.2 Peat

Most of the areas mapped as marine sediments are covered by peat bogs. All peatlands on Slettnes and Laukvika are located below the ML. The peat occur sporadically along the ML and by the foot of the talus zone, but gradually more often down towards sea-level, and are most dominant N of the RSF deposits. The peat are more of fine-grained composition than the marine sand and a high organic content, creating a low permeability of the deposits. The

resulting poor drainage conditions for water have resulted in several ponds in the boggy terrain, especially N of the RSF deposits. Some surface drainage occur in the peat bog areas as small streams across the whole study areas. The largest concentration of streams are found S of the RSF deposits between the talus zone and the ocean. A number of small streams also seems to appear from the front of the RSF deposits. The peat is also found in the morphologically depressed areas within the outer domain of the RSF deposits. Some blocks of the same characteristics as the ones located within the RSF deposits are found in an area of peat, outside the front of the RSF deposits and are further described in Section 3.5.2.

3.4.3 Sporadic sand deposits

Some sporadic bodies of sand are found inside and outside the rock avalanche deposits. These deposits typically consist of massive, medium grained sand interbedded with some thin layers of fine sand (Figure 46). The largest deposit is found between Skrea and the village Slettnes. Some layers are more iron-rich and appear darker than the surrounding sand. The iron-rich parts also proved to be very hard to dig through, as it is finer grained and more compacted. Some sections of the same sand appear sporadically above the ML and within the RSF deposit. Figure 46 shows a sand pit dug at 87 m asl within the RSF deposits.

Figure 46: Field photograph from August 2018. Sedimentary profile through a body of sporadic sand deposits by the southern flank of the RSF deposits. The deposits mostly consist of massive sand.

3.5 RSF/Avalanche deposits

3.5.1 Deposit lakes

Two lakes are present near the southern flank of the rock avalanche deposits (Figure 47). The lakes are c. 100 meters apart from each other and lie at an elevation of 96 and 104 m asl, respectively. Both lakes are of similar size, and have a diameter of c. 15 meters and a depth of 2-3 meters. Ephemeral drainage channels connect the two lakes and can also be traced down through the lower deposit. The lakes are probably controlled by precipitation and ground water seepage.

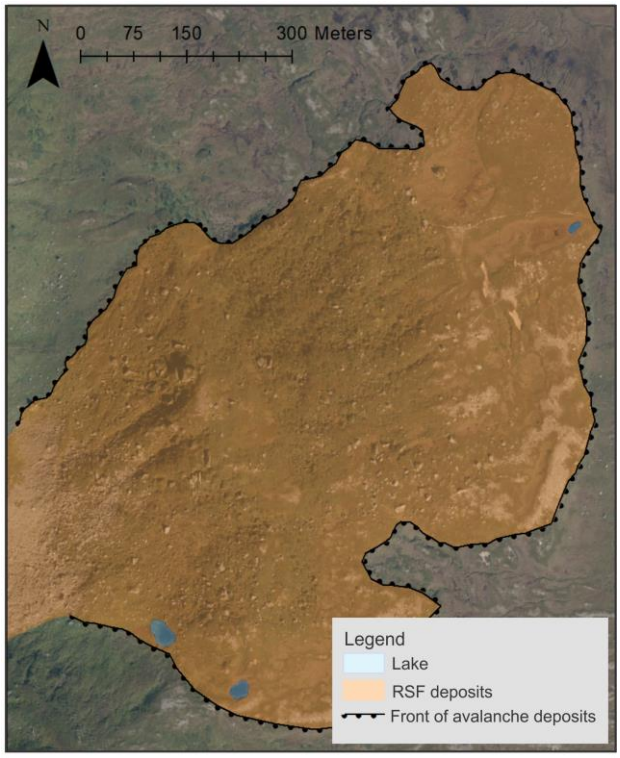

Figure 47: Lakes within the RSF deposit area. Orthophoto obtained from Kartverket (2019).

3.5.2 RSF deposits

The RSF deposits extends for c. 1.4 km from the backscarp, and for 950 meters from the foot of Laukvikfjellet. The general geometry of the depositional body is a lobe shape, with an extending width and declining thickness towards the NE. However the internal geometry of the RSF deposit body varies with distance from the assumed source area. The area can be characterized by 3 main domains (Figure 48 A). The innermost domain extends from the foot of the mountain and slopes upwards from 105 to 115 m for 250 meters towards the NE. The front of the domain is characterized by a distinct change in the slope gradient (Figure 49 A). This ramp slopes down to 45 m asl at 15°. As the ramp flattens out, it gives way to the middle domain. A number of radial ridges can be traced from the foot of the mountain through the inner and middle domains (Figure 49 A). Block sizes in the inner domain range from 1 – 100 m^3, with some extreme cases measuring up to 1000 m^3 (Figure 49 C). The orientation of the blocks are random (Figure 49 B), however the largest blocks tend to be concentrated along the top part of the radial ridges. Inside of the depressions between the radial ridges the average boulder size was up to 10 m^3.

From 45 m asl, the middle domain stretches for 200 meters (400 to 600 meters from the foot of Laukvikfjellet). The radial ridges here are smaller than the ones in the innermost domain, but show a similar orientation. The block sizes range from large rocks to boulders of ca. 10

m^3, smaller than those mapped in the inner domain. The middle domain is highly vegetated, and the northern half is covered by a thin forest. The front of this domain is less distinct than the previous, as it displays a shallower gradient. It slopes from 35 to 20 m asl at an angle of 5-8° (Figure 48 B/C).

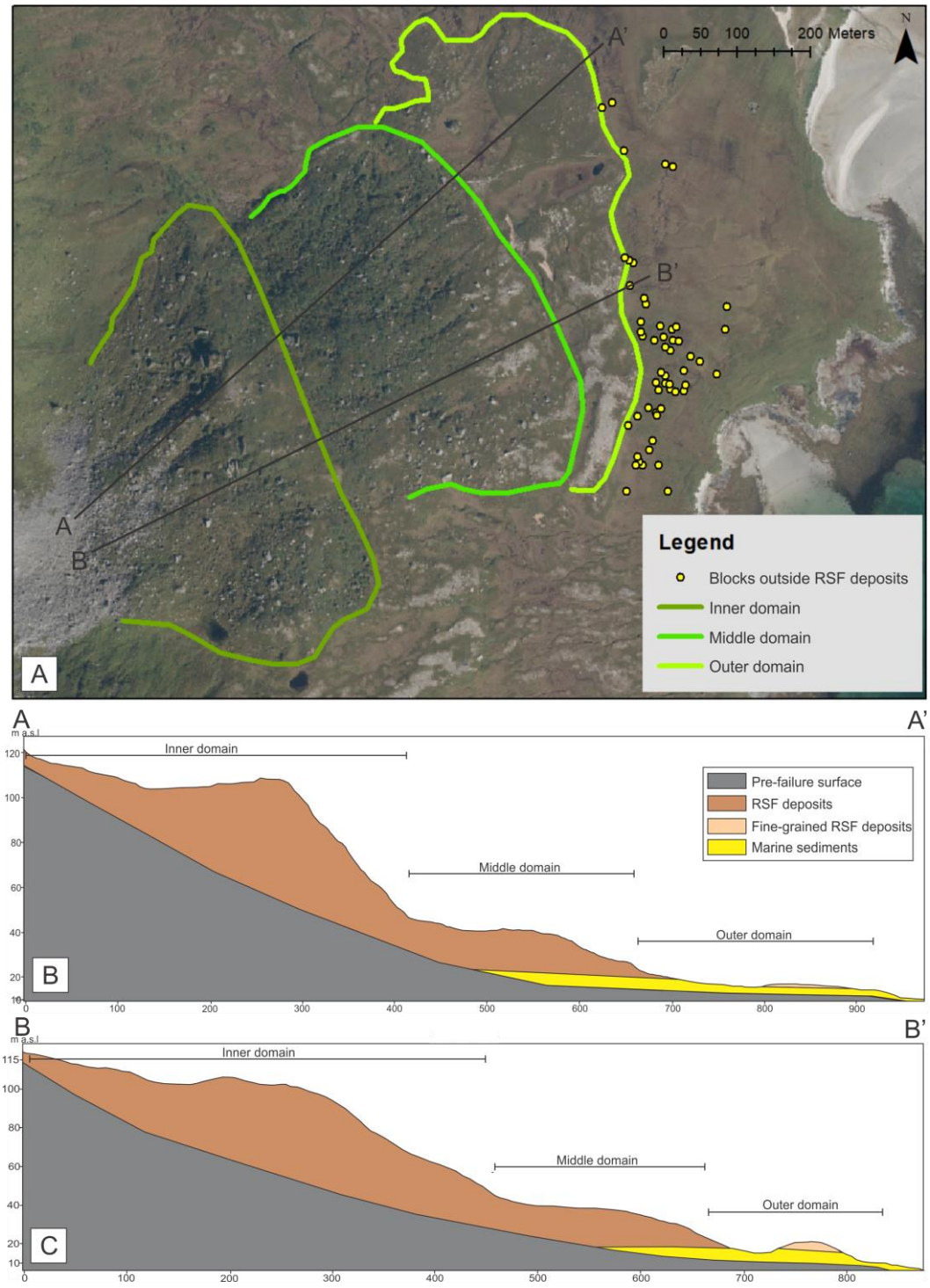

Figure 48 A: Map illustrating the extent of the different domains within the RSF deposits and blocks outside the front of the RSF deposits. Orthophoto obtained from Kartverket (2019). B, C: Simplified elevation profile through the RSF deposits, pre-RSF surface derived from typical surface profiles measured alongside of the deposit area. Vertical scale exaggerated by a factor of 2.25.

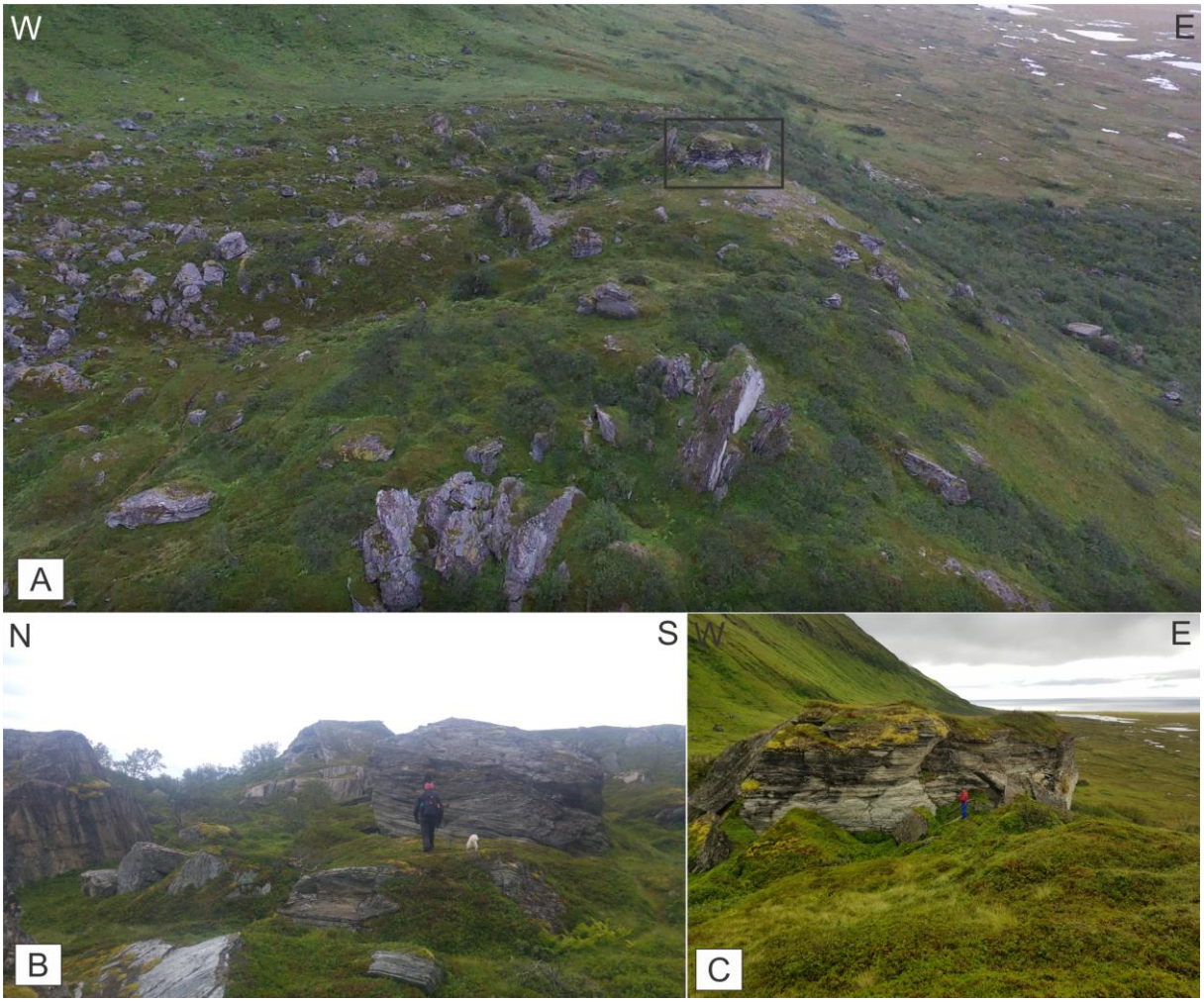

Figure 49 A: Drone photograph of the inner domain from August 2018. Note the radial ridges on the left side of the picture and the distinct change in slope towards the middle lobe. B: Field photograph from August 2018 showing the inner lobe showing the typical size and orientations of the blocks. C: A zoom-in of the black rectangle in A showing the largest block within the RSF deposits.

The outer domain slopes gently from 20 to 15 m asl. This area is less vegetated than the inner two lobes and has no radial ridges. It is characterized by a mixture of peat, marine sand, fine grained rock avalanche deposits and sporadic boulders (Figure 48 B/C). The outer parts of the domain show gentle ridge-like shapes that follows the front of the RSF deposits (Figure 50 A). The fine grained rock avalanche deposits are concentrated to the frontal parts of the lobe. The fine-grained deposit material consists of a range of clast sizes from sand to gravel to boulders <1 m across (Figure 50 B).

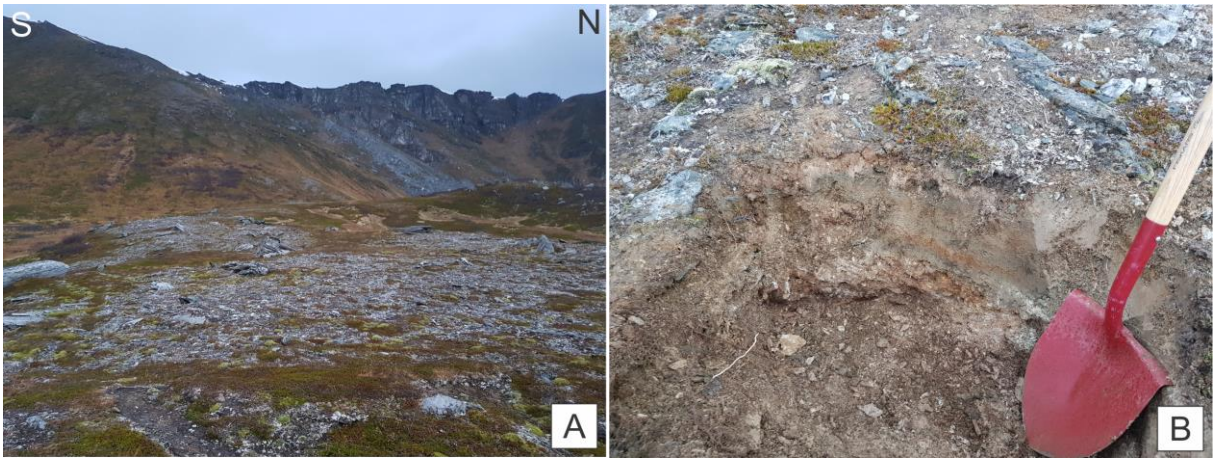

Figure 50 A: Field photograph from November 2018 showing a ridge of fine grained rock avalanche deposits along the flank of the RSF depositional lobe. B: Field photograph from November 2018 illustrating the composition of the fine grained RSF deposits.

The concentration of blocks within this domain is significantly lower compared to the former two. The block range in size from 5 – 10 m^3, and have a random orientation. A large block of roughly 100 m^3 is located in the northern part of the lobe, inside of an area of peat. Some sporadic blocks appear outside the front of the lobe (Figure 48 A). These blocks have the same size as the blocks within the lobe and appear to be associated with the rock avalanche event.

Some areas of the lobe appear to be eroded, shown by missing patches of deposits, and by missing chunks in the lobate front of the deposit. The most distinct area is a missing chunk at the S. A bay-shaped area cuts into the deposits, which results in a narrowing of the deposit from 730 meters to 580 meters in width (Figure 51 A). Several smaller oval-shaped depressed areas are also found inside of the outer domain (Figure 51 E), where marine deposits/peat is exposed (Figure 51 B). The depressed areas appear are boggy and contain no or minimal boulders from the deposit. The depressions are inside of the deposit extent, but breach the boundary of the extent by a thin channel.

Outside of the peat and inside of the deposit, some elongated dune structures are present (Figure 51 C). The dunes contain thick sandy deposits, (Figure 51 D). Some of the dune structures are open, revealing the inner stratigraphy of the deposit. The fine-grained deposit material appears more resistant to erosion than the surrounding areas, as they are more compact and contain a range of clast sizes.

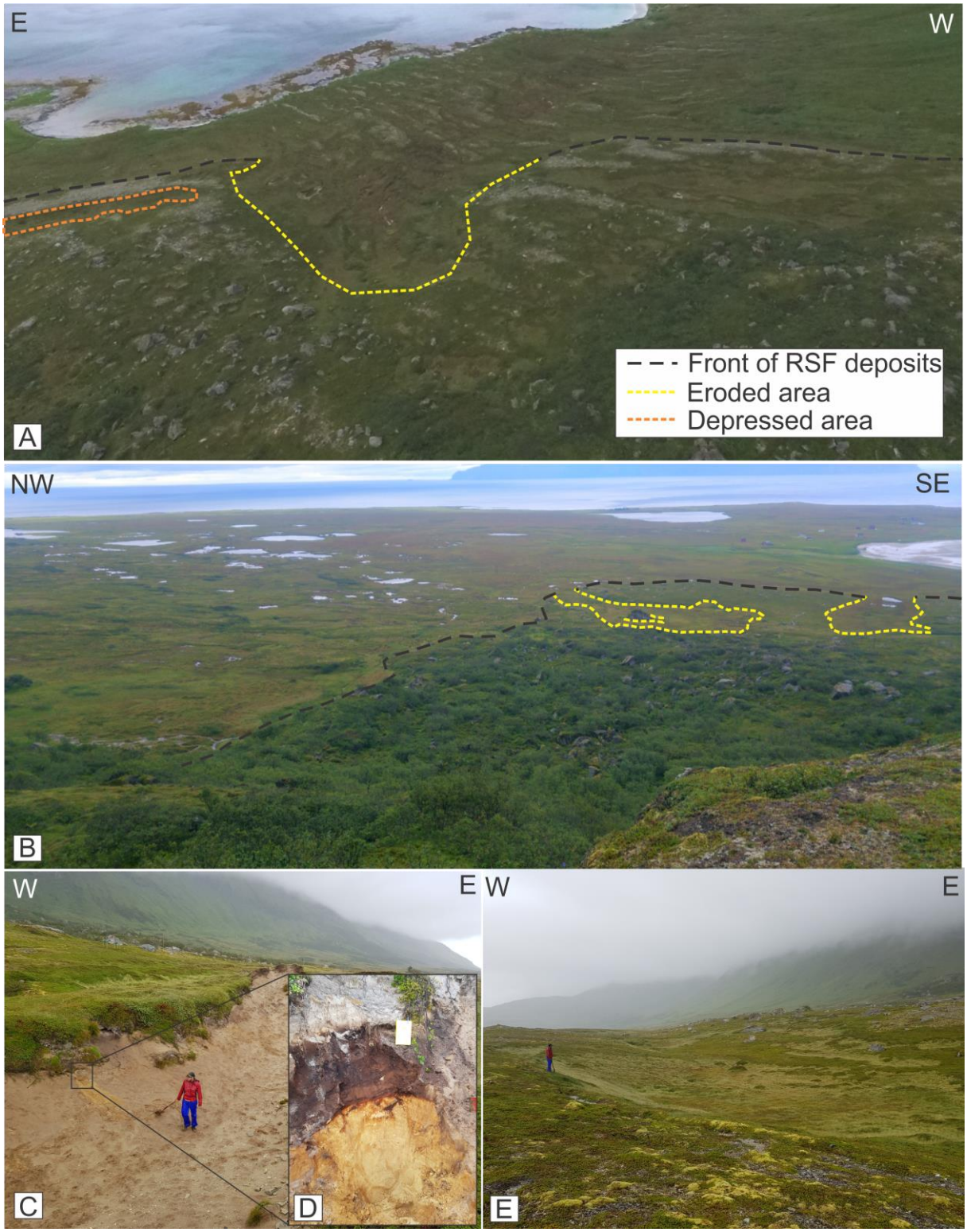

Figure 51 A: Drone photograph from August 2018 showing an eroded area in the southern part of the RSF deposits. B: Field photograph from August 2018 showing eroded lagoon-shaped areas in the northern parts of the RSF deposits. Note the large boulder that are separated from the rest of the RSF deposits. C: Field photograph from August 2018 showing a sandy pit in one of the morphologically depressed areas in the outer lobe. D: Excavated area marked in C. Note the massive texture of the sand. E: Field photograph from August 2018 showing an example of depressed area in the outer lobe.

3.5.3 Raised shorelines and marine deposits

Three shorelines are present at Slettnes and form important morphological markers in the depositional area. The three shorelines were mapped by Corner and Haugane (1993) as the ML, Main and Tapes shoreline. The mapped shorelines corresponds well with the observed shorelines on Slettnes in terms of appearance and elevation and is therefore mapped as in the same manner.

Marine Limit

The ML of the neighbouring valley Skipsfjorddal, assumed to have been formed at the time of deglaciation, is suggested to be ca. 47 m asl (Corner and Haugane, 1993). It is found at Slettnes as an erosional knickpoint in the bedrock at a similar elevation. The ML could only be traced sporadically. It could not be traced across the RSF deposits, but is modelled across the deposits along the same contour. At this elevation, the ML intersects the deposits along the upper part of the middle domain.

Main Shoreline

The most distinct shoreline at Slettnes is found at an elevation of 21 – 22 m asl, and corresponds with the Main shoreline in Skipsfjorddalen. The shoreline is seen as an erosional notch in the uppermost part, and forms a terrace further downslope. The terrace appears as a distinct flat, peaty area, crosscut by some streams. The lower boundary of the shoreline is visible as a distinct drop in elevation. It can be easily traced for c. 500 meters S of the RSF deposits (Figure 52), but is less distinct N of the RSF deposits in the field. The shoreline could be traced for c. 400 meters on a high resolution DEM (Figure 53), but not across the RSF deposits. The Main shoreline is modelled across the RSF deposits on Figure 53, which mostly follows the front of the middle domain.

Tapes Shoreline

The lower shoreline is found at approximately 12 m asl and corresponds with the mapped Tapes shoreline in Skipsfjorddalen. The shoreline starts below the distinct elevation drop below the Main shoreline. The Tapes shoreline has a similar appearance as the Main shoreline, as it forms an erosional notch in the upper boundary, and forms a terrace further downslope. The shoreline is less distinct than the Main shoreline and is crosscut by some streams. It can easily be traced S of the RSF deposits, for c. 500 meters (Figure 52), but

appear less distinct N of the RSF deposits, and could not be traced during fieldwork. The maping of the Tapes shoreline N of the RSF deposits is based on a high resolution DEM (Figure 53). The Tapes shoreline could also be traced along the front of the RSF deposits. The steep front of the RSF deposits appeared like an erosional notch, while a depositional terrace occurred below.

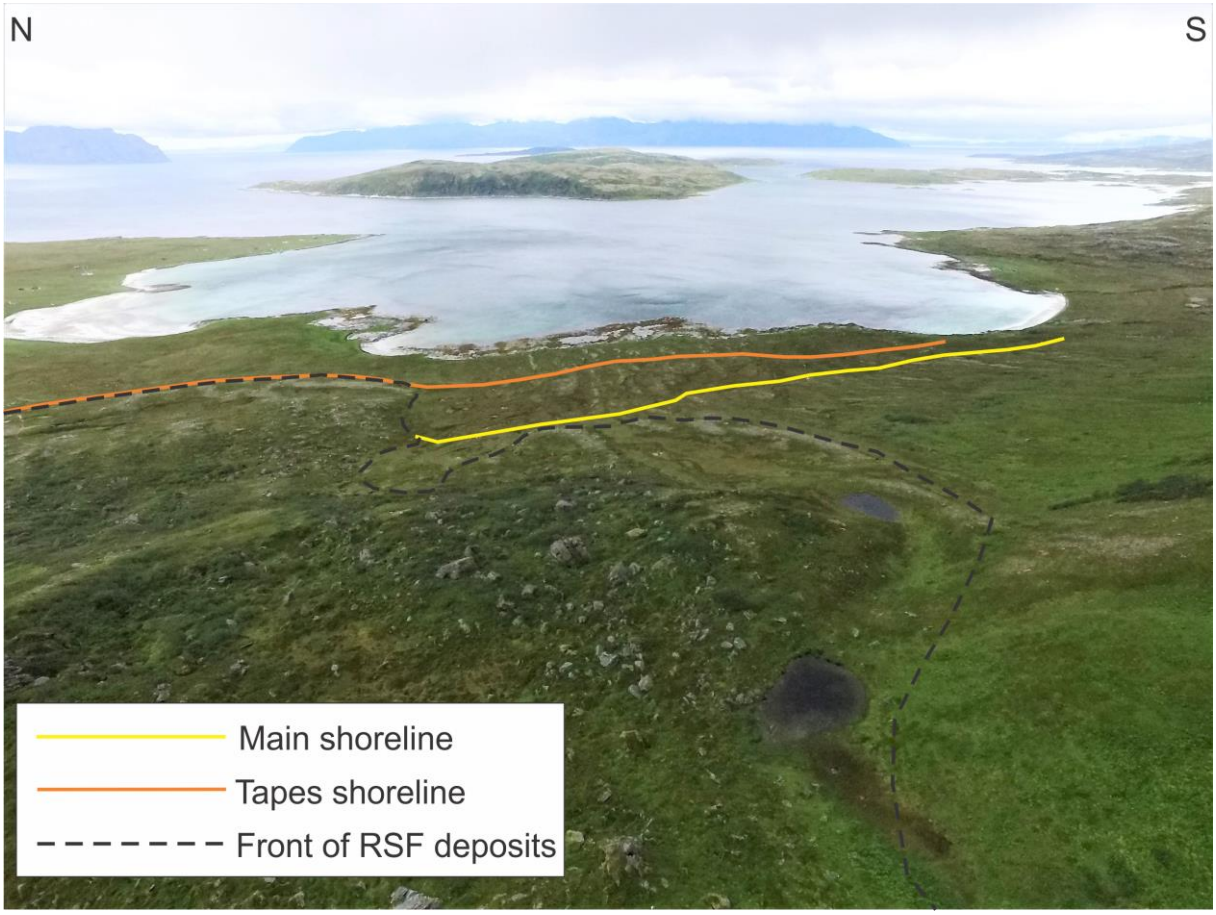

Figure 52: Drone photograph from August 2018 showing the raised shorelines S of the RSF deposits, where they are most distinct. The Main shoreline could not be mapped across the RSF deposits and are therefore not marked across the deposits.

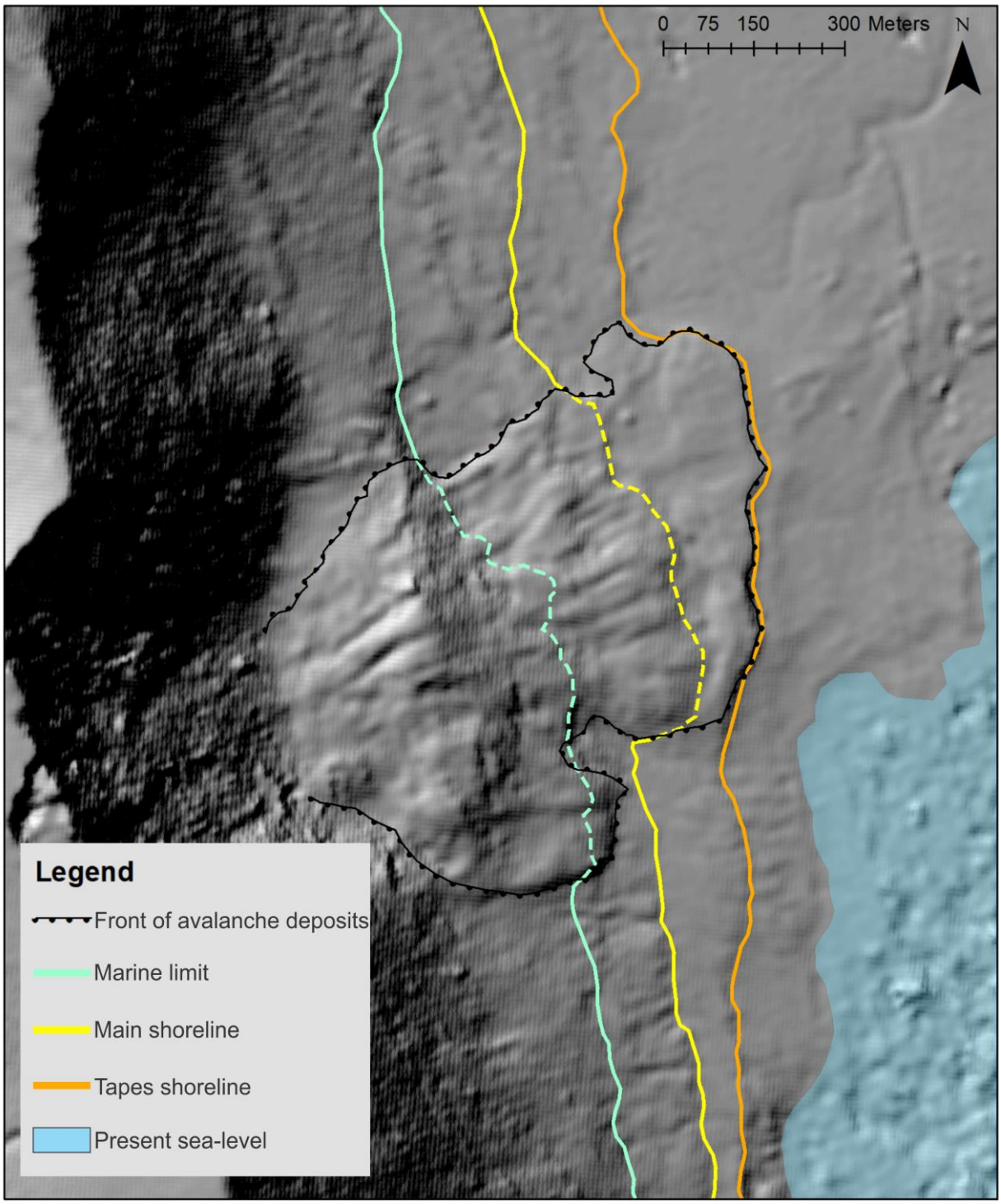

Figure 53: 2 m resolution hillshade map showing the raised shorelines and the ML and their interaction with the RSF deposits. Dashed lines show the modelled shorelines across the RSF deposits. Hillshade based on 2 m resolution ArcticDEM.

3.6 Dating of the rock avalanche event(s)

This chapter presents both the relative and absolute dates of previous RSF events. Relative ages found by studying the cross-cutting relationships between the RSF deposits and surrounding geomorphological elements in the study area and thereby their relative ages. Minimum ages are presented as the ages from ^{14}C dating.

3.6.1 Relative age

The RSF deposits have cross-cutting relationships with other geomorphological elements (Figure 54). As the three marine shorelines have been dated in previous studies, the relationship between these features and the domains within the RSF deposits can be used to put the failure events into a temporal context.

At 12 m asl the front of the RSF deposit drops sharply by ca. 1 m, at a slope angle of 45º before flattening off into a peat platform which contains some large rockfall boulders. The slope angle of the deposit front is markedly steeper than other deposits in the area that are resting at their natural angle of repose. This notch is therefore interpreted as a secondary process, the Tapes shoreline, indicating the deposit is older than the Tapes event.

No other clear notches are visible at the elevations of the two uppermost shorelines (ML and Main). The interaction with these events and the deposits is less clear. The modelled Main shoreline on Figure 53 follows the front of the middle domain, where the geomorphological character of the deposits changes. Above the projected Main shoreline marine sand deposits have been observed, and the deposit is blocky and hummocky. At the shoreline, the radial ridges truncate at an abrupt change in slope angle, and the outer domain below displays a smoother and gentler appearance. The lateral extent of the deposit below the ML is constrained by erosion, with missing sections disrupting the lobate shape.

The ML could not be traced across the RSF deposits. The modelled shoreline is above any mapped marine sand, and no significant erosional features are observed. No clear notch or steep front is mapped, and the ML is projected through the gentle slope connecting the inner and middle domain.

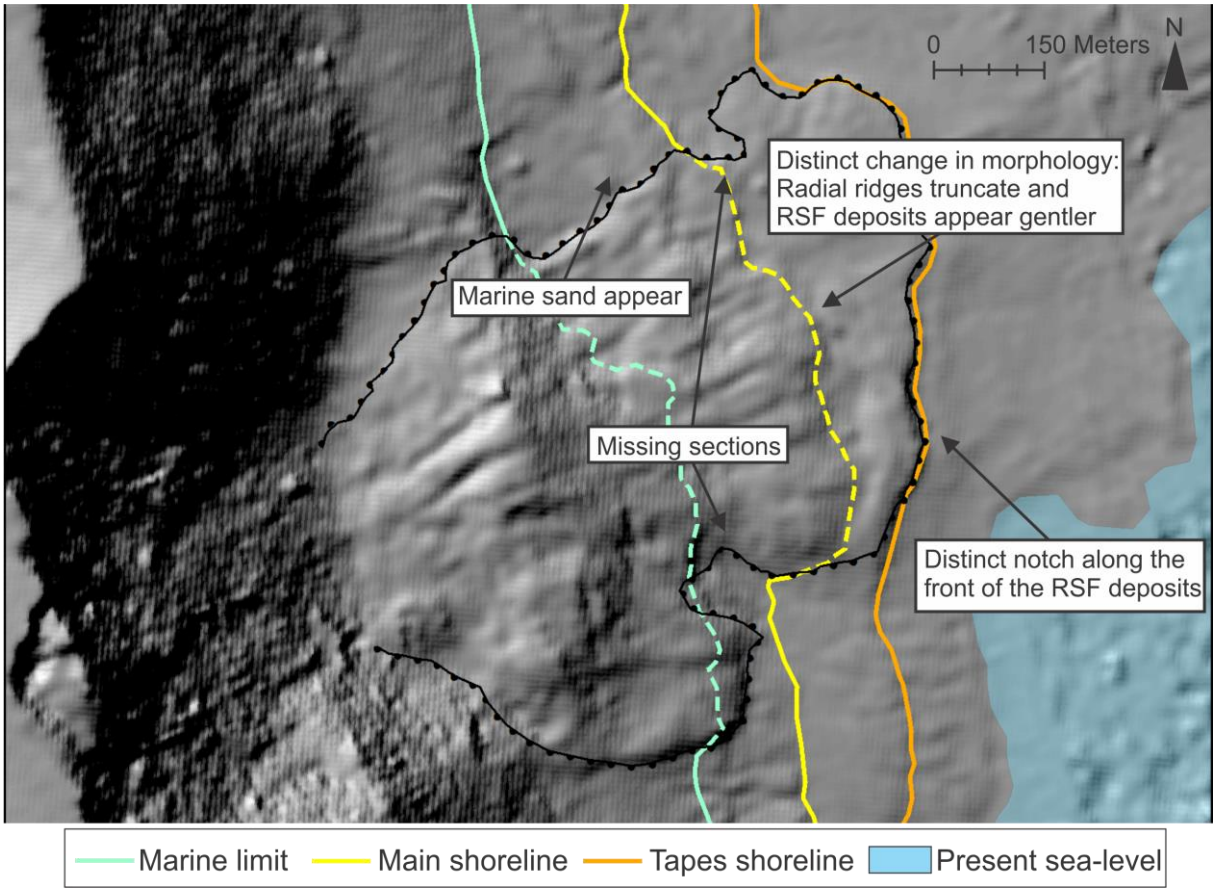

Figure 54: 2 m resolution hillshade map illustrating the different indications for illustrating the relative age of the deposits. Hillshade based on 2 m resolution ArcticDEM.

3.6.2 Absolute age

This chapter presents the ^{14}C ages of the samples measured at Uppsala University.

The sediment core consisted of homogenous peat with some minerogenic contribution of mostly clay to fine sand, with fragments of medium to coarse sand. The deepest samples (58-57 cm) correspond to the oldest calibrated date, 1642 cal. yr BP (Table 1). The samples from a 56-55 cm depth show a slightly younger calibrated age (1598 years BP). The two uppermost samples (40-39 cm and 23-24 cm) correspond to the two youngest calibrated dates of respectively 1017 and 296 years BP. For the three lowermost samples, mostly mosses (and some leaves) were collected for dating, while leaves (identified as Empetrum nigrum) were collected for the uppermost sample.

To find the ages of sediments outside of the sampled intervals of the core, an age-depth profile was modelled using R x64 3.4.3 (Figure 55).

Table 1: Radiocarbon ages of the four lake sediment samples. Calibrated ages are mean ages within the 95.4 % confidence intervals.

Sample	**Lab number**	**Depth (cm)**	**δ 13C‰ (V-PDB)**	**14C age (yr BP)**	**Calibrated age (cal. yr BP)**	**95.4% probability ranges (cal. yr BP)**	**Dated material**
VAN 23-24	Ua-62818	23 – 24	-26,0	257 ± 27	296	429-375, 365-360, 325-280, 171-151	Leaves
VAN 39-40	Ua-62819	39 – 40	-25,0	1 117 ± 27	1019	1170-1163, 1075-957	Mostly mosses, some leaves
VAN 55-56	Ua-62820	55 – 56	-25,0	1 688 ± 28	1598	1693-1655, 1629-1535	Mostly mosses, some leaves
VAN 57-58	Ua-62821	57 - 58	-25,8	1 731 ± 27	1642	1706-1567	Mostly mosses, some leaves

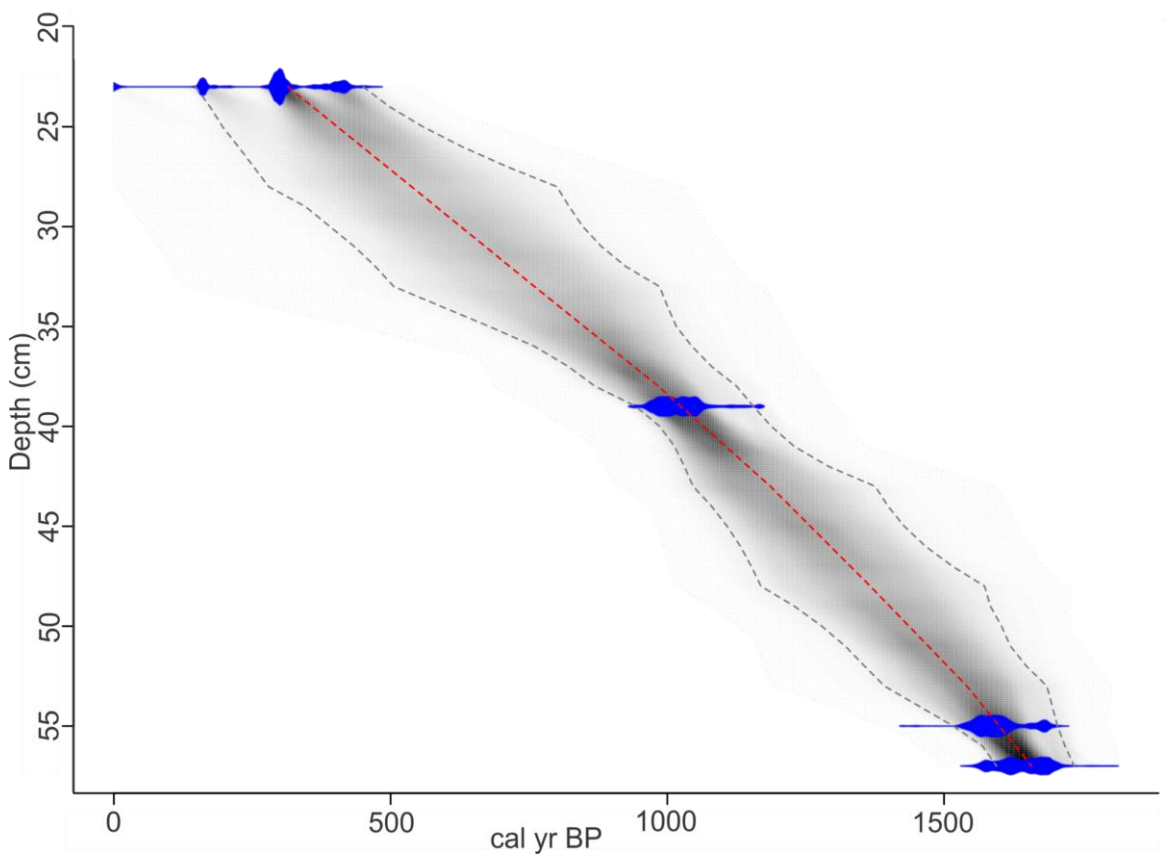

Figure 55: Age-depth model for the avalanche-dammed lake at Skredkallen, showing calibrated radiocarbon dates and age-depth curves (the darker grey indicating more likely calendar ages). Central stippled lines show the best models based on the mean age for each depth and outer stippled lines the 95% confidence intervals.

3.7 Volume estimation

This chapter presents a volume estimation for historic rock avalanches. Volumes are presented for the three domains illustrated in Figure 48. Volume estimation for previous RSF events are based on the formula presented by Scheidegger (1973). The height difference and run-out distance are based on the elevation of the current unstable area and the current extent of the mapped RSF deposits.

The run-out distance (L) are measured as the distance from the backscarp to the front of the RSF deposits along the profile showed on Figure 56. The height difference (H) are measured as the difference in elevation between the backscarp and the front of the RSF deposits. The measured values are 1420 m for run-out distance (L) and 460 m for height difference (H) (illustrated on Figure 57). Together, these parameters give an angle of reach of approximately 18°. This angle gives a volume of c. 13 Mm^3 using Scheidegger (1973) formula (Figure 58). This volume has been calculated based on the maximum avalanche runout, without consideration of the possibility of multiple failure events which may have formed the deposit.

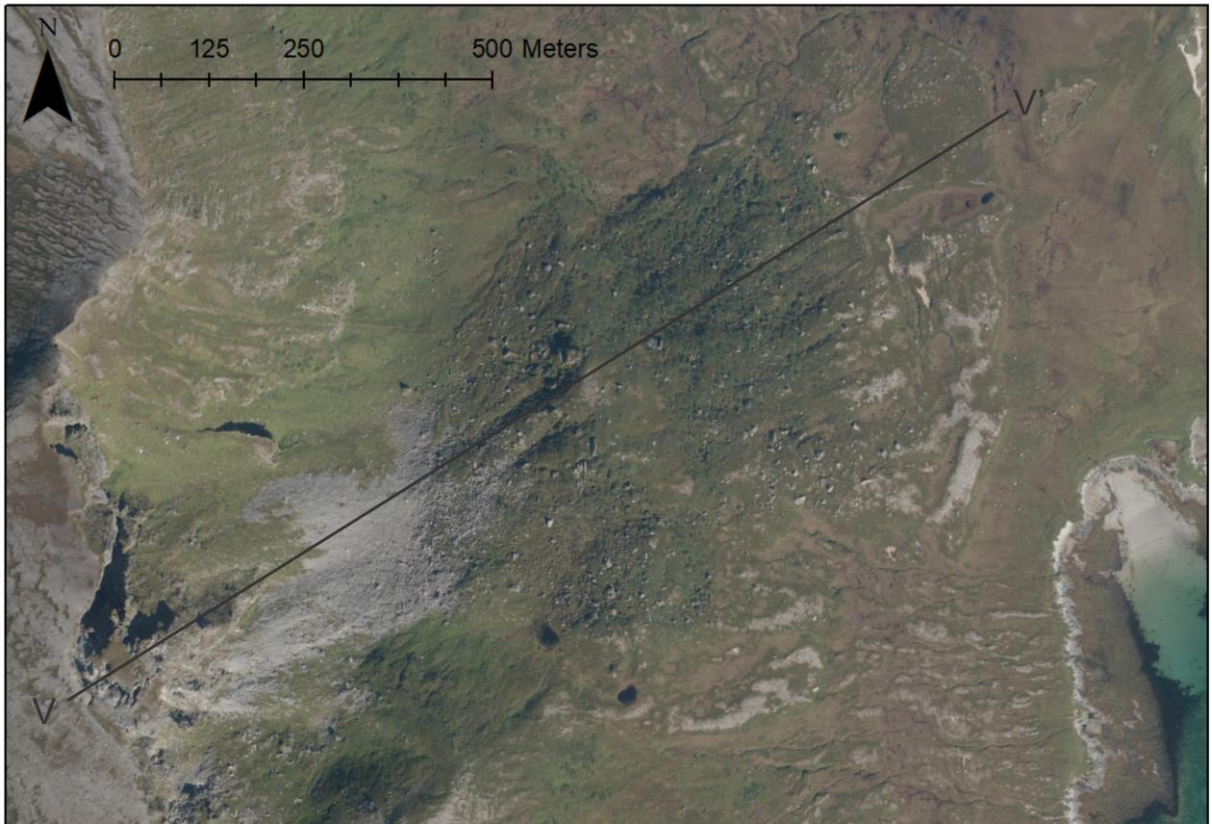

Figure 56: Map showing the profile line used to measure parameters for calculating volume. Orthophoto obtained from Kartverket (2019).

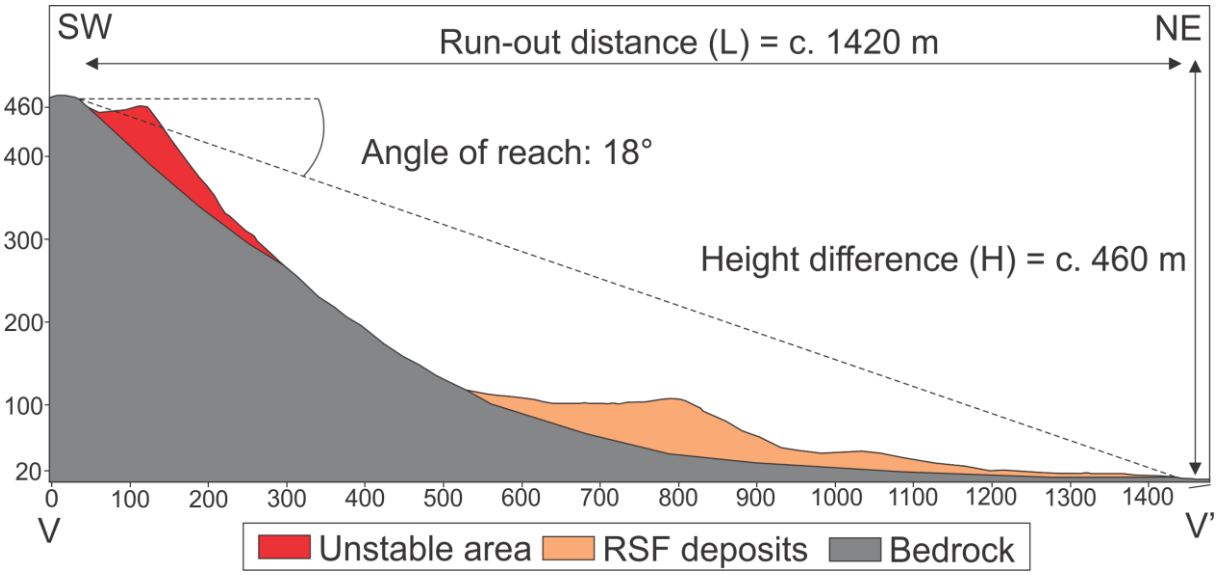

Figure 57: Profile across the URS and RSF deposits illustrating the different parameters used to calculate the volume of the rock avalanche.

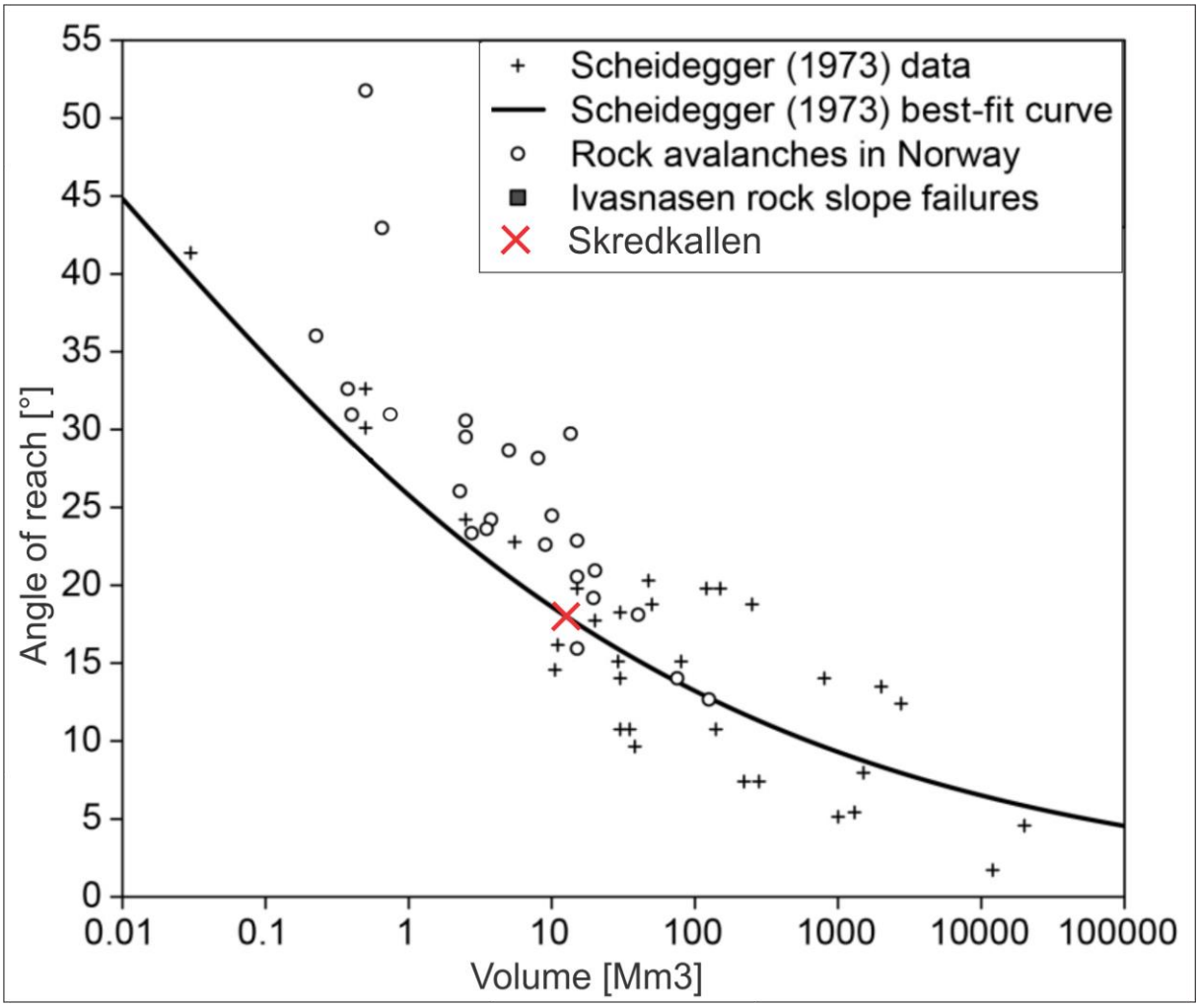

Figure 58: Angle of reach from the measured run-out distance and height difference plotted into the Scheidegger curve. Modified after Oppikofer et al. (2017).

3.8 Geology and structural analysis

3.8.1 Lithology

The lithology of Skredkallen is tonalitic gneiss with mylonitic foliation, cross-cut by numerous mafic sills, (Figure 59; Bergh et al., 2007). The tonalitic gneiss is homogenous and shows little variation in colour and texture. However, some local variations in plagioclase and quartz content can be found. The tonalitic gneisses show high strength as they require numerous hammer strikes to break apart.

The mafic sills are oriented parallel to an older generation of foliation (Figure 60), which occasionally is crosscut by zones displaying a phyllitic to mylonitic structure in a grey to brownish matrix. The cross-cutting zones are parallel to the later-stage dominant foliation, dipping gently towards NNE and are up to 0.05 m thick, with an average thickness at c. 10 cm. (Figure 59). The zones are usually found in the upper part of the mafic sills. In some places, the zones are heavily weathered and show low strength as they could easily break by a hammer strike. These zones could represent internal shear zones related to thrusting of the Skipsfjord Nappe.

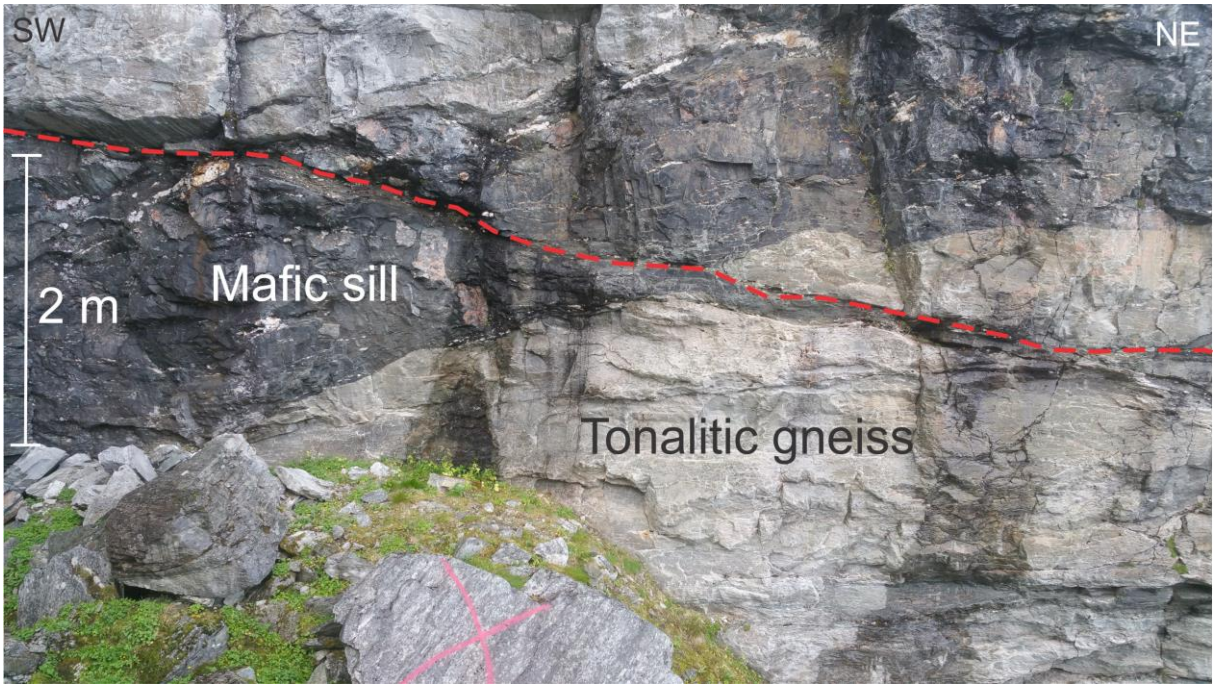

Figure 59: Field photograph from August 2018 illustratiing the lithologies on Skredkallen along the NE-SW striking backscarp. The red stippled line are marked along the upper boundary of a possible internal shear zone.

3.8.2 Foliation

The foliation (SF) in and around Skredkallen is well-developed, with measurements of the in-situ bedrock along the backscarp showing an average gentle dip towards NNE (292/14±13.8). Dip angle varies by up to 13°. The foliation is widely spaced and displays mica-rich surfaces. Slickedslided surfaces with a NW-SE trending sense of shear occur along the foliation. Stretching lineations (ductile) are common features, typically found in the intersection between joint sets, foliation or cleavage and gently NW dipping foliation.

The main parts of the URS show a similar foliation orientation to the back scarp, but slightly tilted in various directions (Figure 60). The tilting direction varies throughout the whole URS. Figure 61 shows how small parts of blocks are tilting either towards NE or SE relative to the general foliation which is striking NW – SE.

Figure 60: Drone photograph from August 2018 showing foliation orientations on Skredkallen. Foliation on the displaced rock column "Kallen" are marked as yellow stippled lines. Foliation along the back scarp are marked with white stippled lines. Mafic dykes are shown with orange markers.

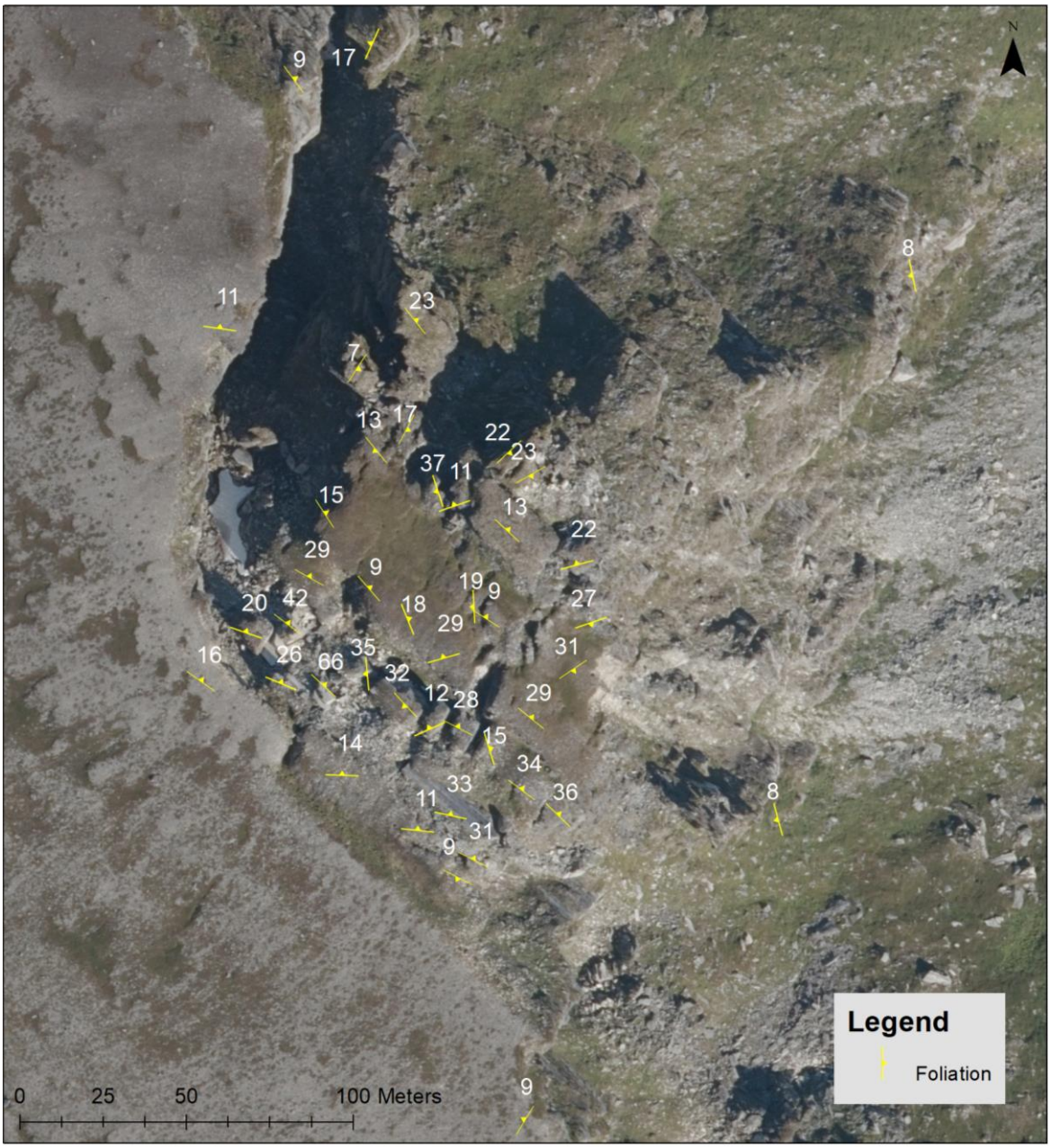

Figure 61: Foliation measurements. White numbers above foliation symbols show the dip for the measured site. Orthophoto obtained from Kartverket (2019).

3.8.3 Joints and fractures

Four main joint sets have been mapped at Skredkallen. The joint sets presented in Table 2 were defined on the basis of field observations and structural measurements along the backscarp (i.e. in situ bedrock). The joint sets (and foliation) are illustrated in Figure 62 using Dips 7.0 with 1σ standard deviation variability cone. These structures are cutting all lithological units and occur at all scales. Joints and fractures are found both in the bedrock and in the URS. The smallest fractures haven't developed an opening yet or are covered by vegetation, while the largest show openings of up to 2 – 3 m. Both listric and planar fractures are observed. There are great variations within all joint sets in terms of strike/dip, which

means a large number of joint sets could be present at Skredkallen. However, four joint sets were clearly observed (Figure 63), and therefore identified in this study for practical reasons.

Table 2: Orientation, spacing, persistence, shape and roughness of the mapped discontinuities. The attributes given in this table are based on estimates in field.

Set	**Orientation (strike/dip)**	**Spacing (m)**		**Persistence (m)**		**Shape**	**Roughness**
		NE/SW	SE/NW	NE/SW	SE/NW		
SF	292/14 ± 13.8	0.05 – 0.5	-	0.1 – 2	-	Planar	Rough
J1	034/82 ± 16.9	-	0.5 – 2	-	10 – 25	Planar, occationally listric	Smooth to very smooth
J2	203/66 ± 9.0	-	0.2 – 1	-	0.5 – 1	Planar	Smooth
J3	309/68 ± 10.5	0.2 – 0.5	-	0.1 – 0.5	-	Both planar and undulating	Rough
J4	117/83 ± 15.5	0.5 – 1	-	0.5 – 20	-	Planar	Rough

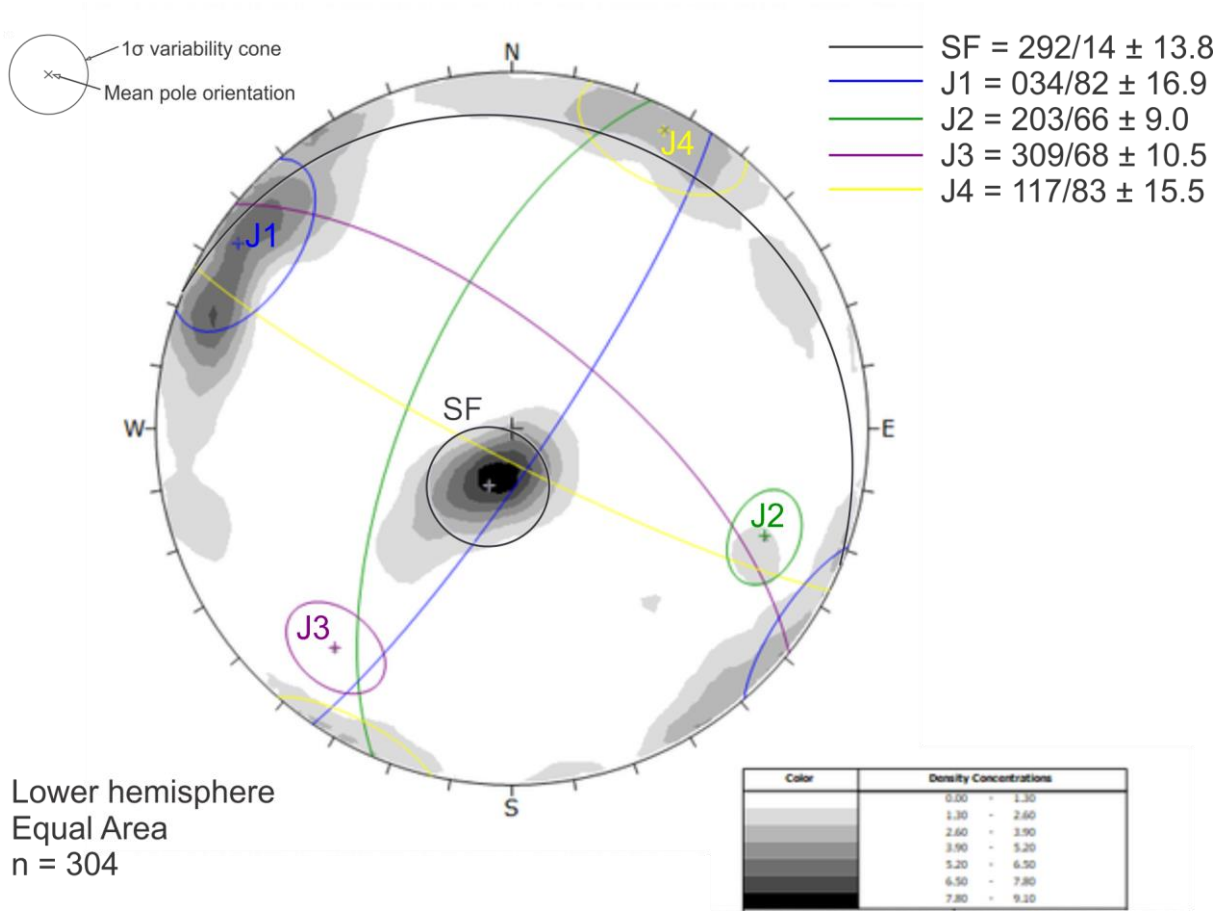

Figure 62: Stereographic analysis for the measurements done at Skredkallen. Joint set assignment is based not only on stereographic analysis, but also on field observations, e.g. in the case of J2 and 3.

Figure 63: Field photograph from August 2018. Illustration of joint sets 0.5 km south of Skredkallen in an ESE facing aspect.

Joint set 1 (J1) is the most dominant joint set on Skredkallen and strikes NNE-SSW with a steep fall towards ESE (034/82±16.9). The J1 joints are well distributed along the whole back scarp with high persistence and smooth planar planes, which in some places becomes listric with depth (Figure 64 A). Even though some planes show listric geometry, the strike orientation remains constant. Slickenslided surfaces with slickenlines are found on some planes, which could indicate a pure-dip slop down towards SSE. Joint set J1 generally corresponds with the NE-SW striking morphostructures. Orange mineral coating often occurs along this joint set (Figure 64 B). Some pink staining occurs occasionally.

Joint set 2 (J2) is striking NNE-SSW with a moderate dip towards NNW (203/66±9.0). The set was observed less frequently than the other sets. The joints often displayed orange mineral coating (Figure 64 B). In the field, J2 could be observed as being part of a conjugate set (Figure 64 B). J2 corresponds with the NNE-SSW striking backscarp.

Joint set 3 (J3) is striking NW-SE with a moderate dip towards NE (309/68±10.5). J3 was easy to observe in the field, but hard to measure. This set is slope parallel, and shows low persistence and frequency. In some places, J3 displays a very distinctive, undulating geometry as it tends to refract along foliation (Figure 64 C). The undulating geometry can be observed both in small- and large scale on similar slope aspects along the backscarp. In small scale it is observed as a stepwise failure, while on large scale it appears more undulating.

Joint set 4 (J4) is striking NW-SE and is dipping steeply towards SW (117/83±15.5). This is a prominent joint set. Calcite slickenlines can be observed occasionally, indicating dextral strike-slip movements. J4 appears both in small scale as fissures with low persistence and in large scale as highly persistent near-vertical walls along the backscarp. Joint set J3 and J4 corresponds well with the NW-SE striking morphostructures.

Figure 64: Field photographs from August 2018. A: J1 joints with listric geometry. B: Conjugate joints with orange mineral coating. C: The coloured area illustrates the undulating geometry along J3 joints.

3.9 InSAR data of the study area

3.9.1 Introduction

InSAR from the Sentinel-1 ascending 1 and 2 satellite paths are presented as maps showing LOS displacement in mm a^{-1}. The displacement rates are examined in relation to morphological elements (scarps, terraces, columns) to get a better understanding of how the unstable area moves, and which areas are the most actively moving. It is important to mention that all velocities are recorded within the LOS of the satellite, which only displays one component of the movement vector. As a result, the actual movement rates could be greater than the velocity measured by the satellites. Comparting more than one LOS data set can give an indication of the actual movement vector. The two ascending satellite tracks have very similar data capture orientations, however they show a difference of 1.8º in the LOS, with ascending 2 closer to the E azimuth. Ascending 2 also shows an incidence angle 4.6º steeper than ascending 1.

3.9.2 Velocity data by satellite-based InSAR

Displacement rates from the Ascending 1 and 2 satellites are presented in Figure 65 A as point data. Negative values show a movement away from the satellite. When assessing variations in velocity for point data, polygons are drawn for areas that display similar displacement rates, as they display a more area-wide movement. A total of 7 polygons are drawn and shown in Figure 65 A. The yellow to red coloured points show negative (downward) displacement rates, while the blue coloured dots show positive (upward) displacement.

Both satellites indicate that the highest velocities are found at Kallen and at the southern terrace (Polygon 4 and 7). Velocities in these areas are up to -12.3 and -10.0 mm per year respectively (Figure 65 B). The Ascending 2 satellite generally displays higher variations and higher values in velocity. The other polygons within the unstable area (polygon 3, 5 and 6) show displacement rates between -0.9 and -2.2 mm per year. Two polygons were measured outside the unstable area, in situ bedrock (Polygon 1 and 2), and display movement rates of -0.4 to 0.9 mm per year. The velocity graphs showing average displacement rates presented in Appendix A suggests that the unstable area moves fastest in June and September.

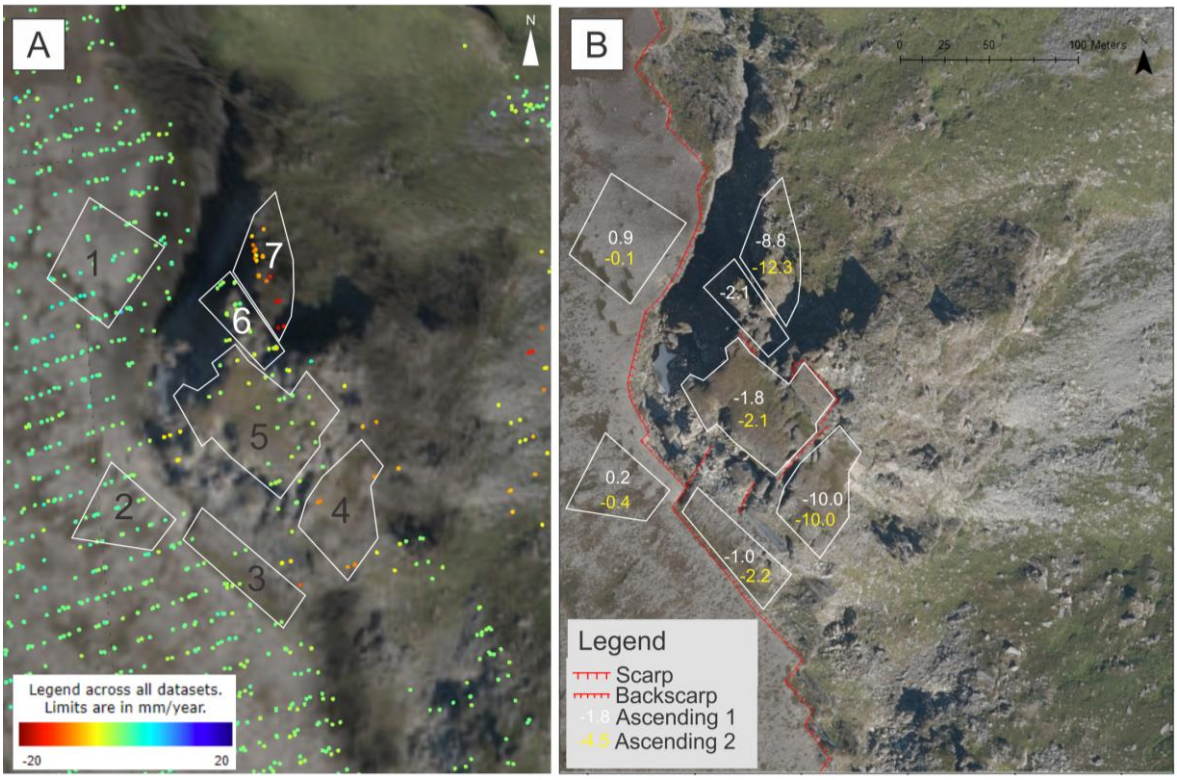

Figure 65: A: Overview of displacement measured from the Ascending 1 and Ascending 2 satellites and the polygons of the unstable area. B: Map of the same perspective with measured displacement rates for each polygon and the main morphostructures relation to the polygons. Values are negative as they record movement away from the satellite. Orthophoto obtained from Kartverket (2019).

4 Discussion

4.1 Introduction

The URS at Skredkallen is a unique case as it as it is the only URS in the WTBC that has been intensively studied. The site is popular recreational area for locals. It is therefore of both scientific and social interest to understand the driving and controlling factors of the URS.

It is also of interest to understand the history of previous events and their controlling factors, to understand how the slope has responded to different triggers, to try to predict possible future events. As the RSF deposits below Skredkallen are interacting with previously studied and dated geomorphological elements, as well as the dated lake sediments from this study, it is possible to relate the deposits to these elements in order to constrain a relative timeline.

The discussion chapter brings together key results presented in this study to present a conceptual and historical overview of the unstable area at Skredkallen and its deposits. The research objectives presented in Chapter 1.2 will be addressed in this chapter by answering key questions.

4.2 Geology and movement of the URS

4.2.1 Lithology

Skredkallen differs from previous studies of URS in Troms, as it's located within the WTBC, while the majority of mapped URS are located within the Caledonian Nappes (NGU, 2019c). The gneiss bedrock of Skredkallen are considered very strong, and could only be chipped with a geological hammer, giving an unconfined strength of > 250 MPa based on Appendix B. The gneisses are likely to have a higher friction angle (Wyllie and Mah, 2004) than the typically mica-rich schists in eastern Troms (such as the URS on Jettan described by Blikra et al. (2015)).

In the hammer test, the phylitic to mylonitic internal shear zones correspond to a very weak strength value (1 – 5 MPa; Appendix B). They also show some preferential weathering within these layers relative to the surrounding gneisses, indicating a softer nature. These zones could act as sliding surfaces for the URS if they occur at depth in the area of the assumed basal sliding surface. They may also act as a boundary for the flow of groundwater within the URS, decreasing the shear strength of the zones. The zones are parallel with the foliation dipping towards NNE, making it kinematically feasible for sliding along the surfaces.

The internal shear zones can be linked to the emplacement of the Skipsfjord Nappe, as they are aligned with the foliation formed during this event. The thrusting event and also the proximity of the Nappe boundary might suggest that larger shear zones may be present at depth.

4.2.2 Foliation

The foliation has a gentle dip towards NNE. The weak zones within the bedrock are parallel with foliation and could create potential failure surfaces. The basal rupture surface of the unstable area is likely a result of a proportion of foliation planes. Even though some local folds were observed during fieldwork, the foliation on Skredkallen is mostly planar. As all structural measurements were restricted to the upper area of Laukvikfjellet, the possibility of fold structures or changes in foliation orientation in the deeper parts of the URS cannot be excluded.

4.2.3 Morphostructure

There is a strong relationship between the bedrock structure and morphostructure. Within the unstable area we find a consistent alignment of morphostructures: backscarps, scarps, counterscarps and open fractures are all striking NE-SW, NNE-SSW and NW-SE. These structures align well with the regional structures on Vannøya mapped by Bergh et al. (2007) as well as the Skipsfjord-Slettnes Fault and all four locally mapped joint sets. It is likely that the large-scale structures on Vannøya are closely linked with the structures controlling Skredkallen, i.e. the joint sets. The regional tectonic environment has clearly had a large imprint on the bedrock of the WTBC, and is now controlling how and where it destabilises at a local level.

The backscarp is controlled by J1 (NE-SW scarp), and J3 (NW-SE). Where the URS is detaching on J3 surfaces, sliding is observed. Where the URS is detaching on J1 surfaces a tensile opening is observed. Sliding is possible on J3 as it has a dip of 60 - 70°, whereas J4 is sub vertical. This is evidenced by a sliding movement of the unstable area along the NW-SE striking backscarp (J3 surfaces) and a down-sliding movement of the main terrace relative to the “horst” structure. This phenomenon is also repeated throughout the URS, with J3 controlling the formation of most scarps, and a sliding offset observed across them. Some planar sliding movement between the horst and graben structures occur along J4, with an opposing dip to the NW-SE backscarp. Comparatively, where J1 makes up the backscarp a large trench is observed between it and the unstable mass. The movement along J1-controlled

morphostructure throughout the URS is toppling to SE. The material which is separated by these structures displays little difference in elevation, but is generally tilted to the SE in the more distal parts. Toppling has resulted in a metastable rock mass along the southern flank of the unstable area. The steep nature of J1 (and sometimes J2) along the southern flank promotes failure in this area, leading to rockfall and a fresh avalanche scarp on the southern terrace.

4.2.4 Movement and failure mechanism

The interpretation of structural controls on the different parts of the URS are illustrated on Figure 66 and two profiles from Figure 68. The two profiles are modified versions of the conceptual models presented by Trønnes (2019) and are based on a 7.51 cm/pixel DEM.

As the backscarps of the URS are steep and do not daylight in the lower slope (i.e. they are not through-going to the toe), the sliding surface must be controlled by more than one structure. The steep backscarps must transfer to a lower-angle structure to allow for the toe to daylight. Therefore, because the slide isn't a simple planar translational slide, it fits well with the description of a typical compound slide (Glastonbury and Fell, 2008, Hermanns and Longva, 2012, Hungr et al., 2014), a slide which is controlled by more than one structural surface for failure. The sliding movement at Skredkallen is likely controlled by SF and J3 (Illustrated on Figure 66 and Figure 69). The steep dip of the backscarps combined with the gentle dip of the foliation likely forms as J3 and SF could create a step-path geometry (Inset in Figure 69). The sliding surface is probably listric, following J3 in the upper parts, but gradually follows SF more with depth. The step-path/listric geometry leads to internal shearing in parts of the URS, leading to an intensifying in the development of cracks and scarps at the surface (Glastonbury and Fell, 2008). The scarps, counterscarps and surface fractures most likely are a result of this high degree of internal shearing within the rockslide. The frontal part of the unstable area has a step-formed surface where previous failure(s) have occurred, indicating that in previous failures the same failure mechanism may have occurred. Horst-and-graben features are typical morphology for a compound slide, found at the head of the slide. The inward dip of the foliation at the toe supports the idea that the failure surface is listric, and there has been a backwards rotation of the mass in the lower parts. No distinct toe can be mapped which indicated compression the lower slope.

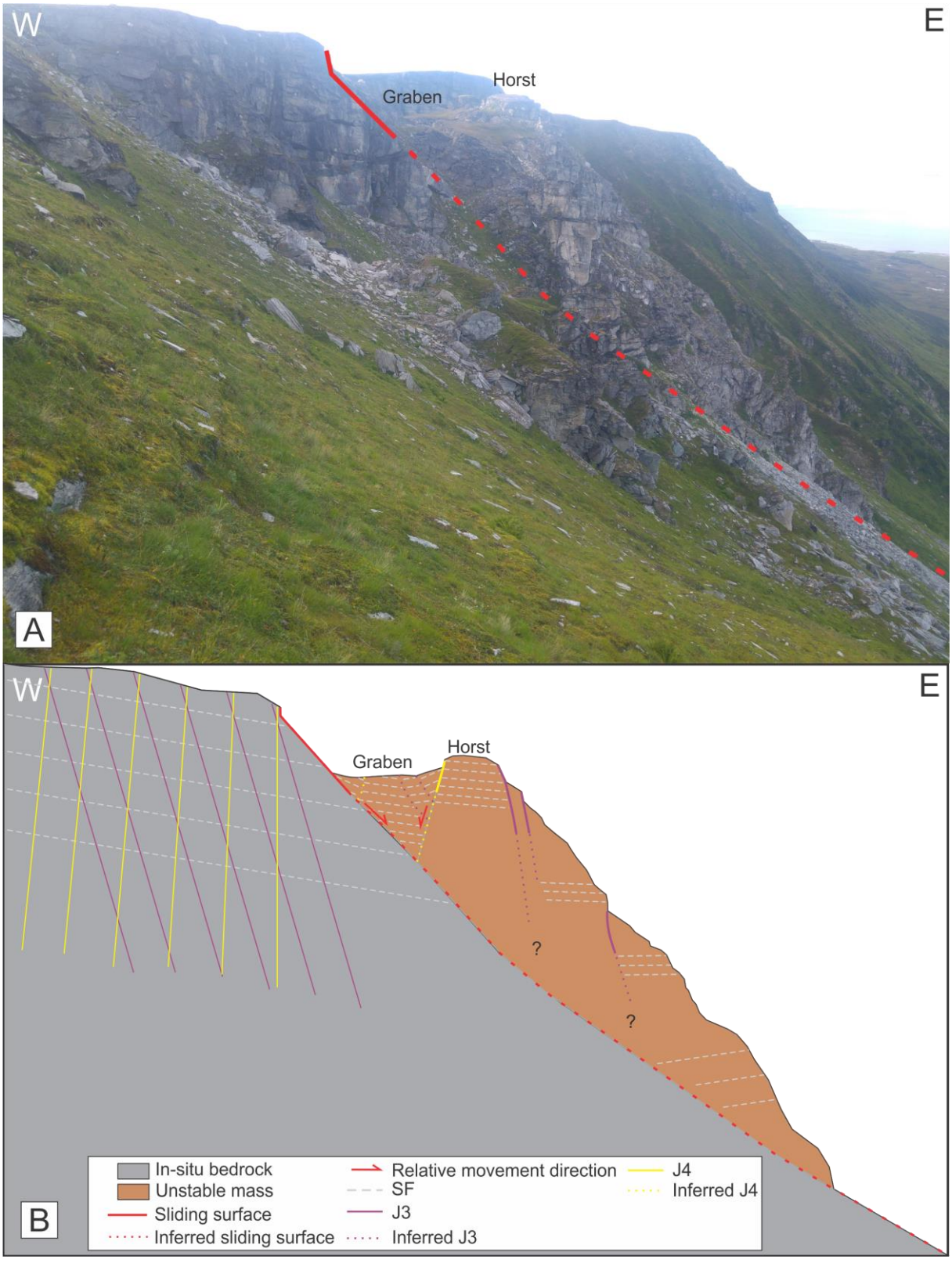

Figure 66 A: Field photograph from August 2018 of the S-facing aspect of the unstable area. Red line illustrates the sliding surface B: Schematic profile of the same aspect showing the most prominent morphostructural features.

Kallen is separated from the rest of the unstable area by a NE-SW opening. The opening towards NE is likely controlled by J4. J4 is subvertically dipping towards the face, which is

required for toppling failure (Wyllie and Mah, 2004). The J4 joints are orthogonal to the foliation, which creates the base of the failure surface and allows the frontward movement of the column (illustrated on Figure 67).

Rockfall deposits beneath the column suggest that the column has been recently debuttressed, destabilising it and allowing it to tilting further towards NE. Kallen is the fastest-moving segment of the URS and should be closely monitored for failure over the coming years.

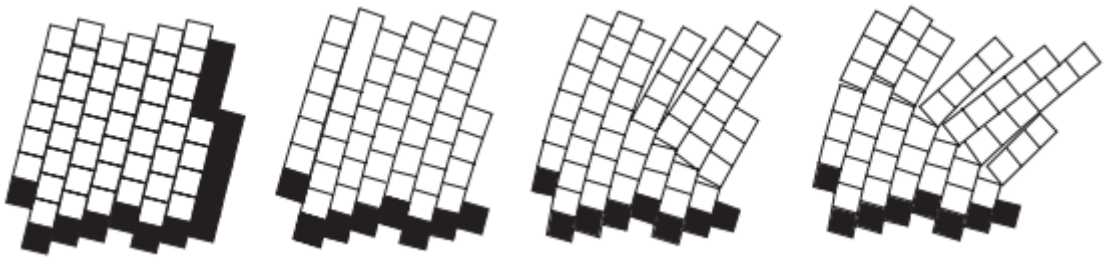

Figure 67: Model of toppling failure; Blocks are made two orthogonal discontinuity sets. Solid blocks are fixed in space while open blocks are free to move. From (Wyllie and Mah, 2004) after (Cundall, 1971)

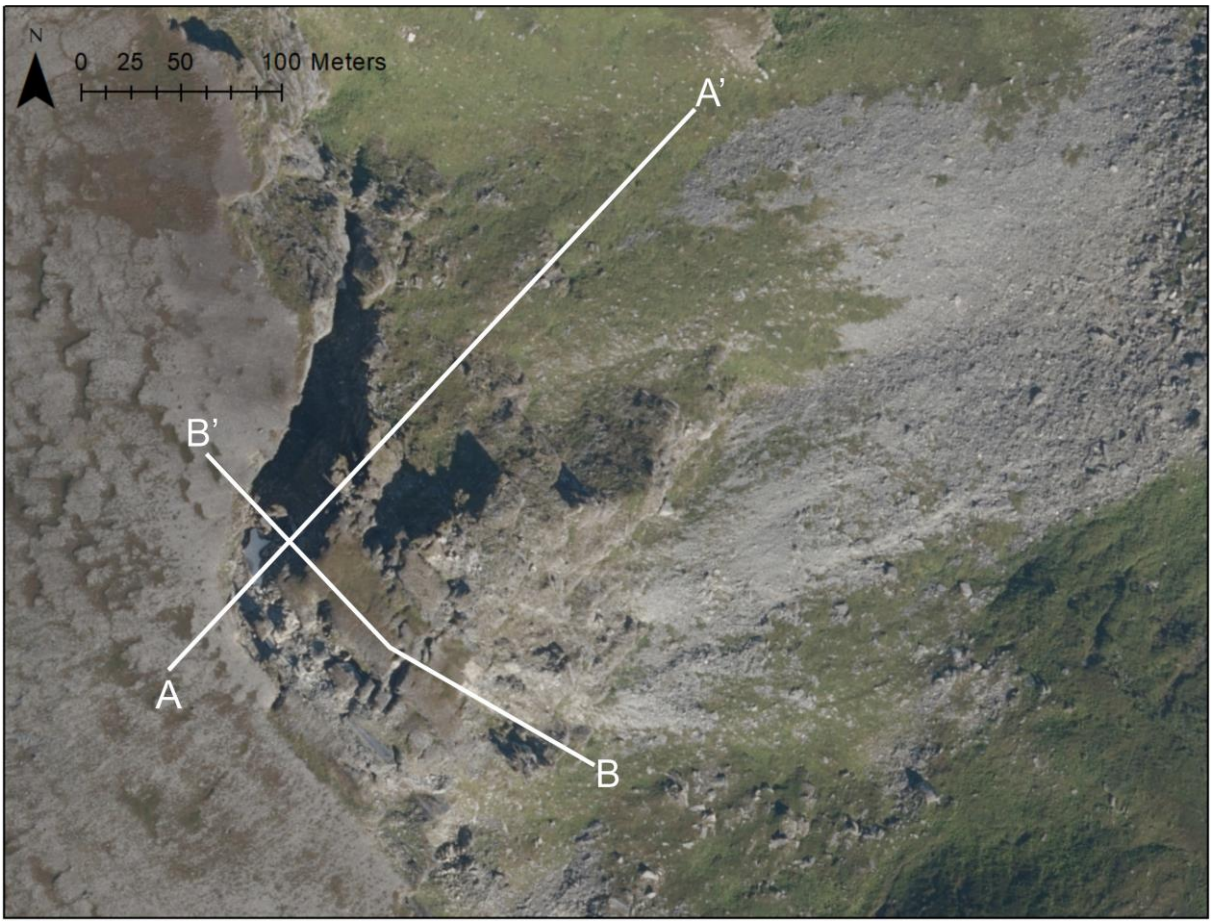

Figure 68: Location of the structural profiles presented below. Orthophoto obtained from Kartverket (2019).

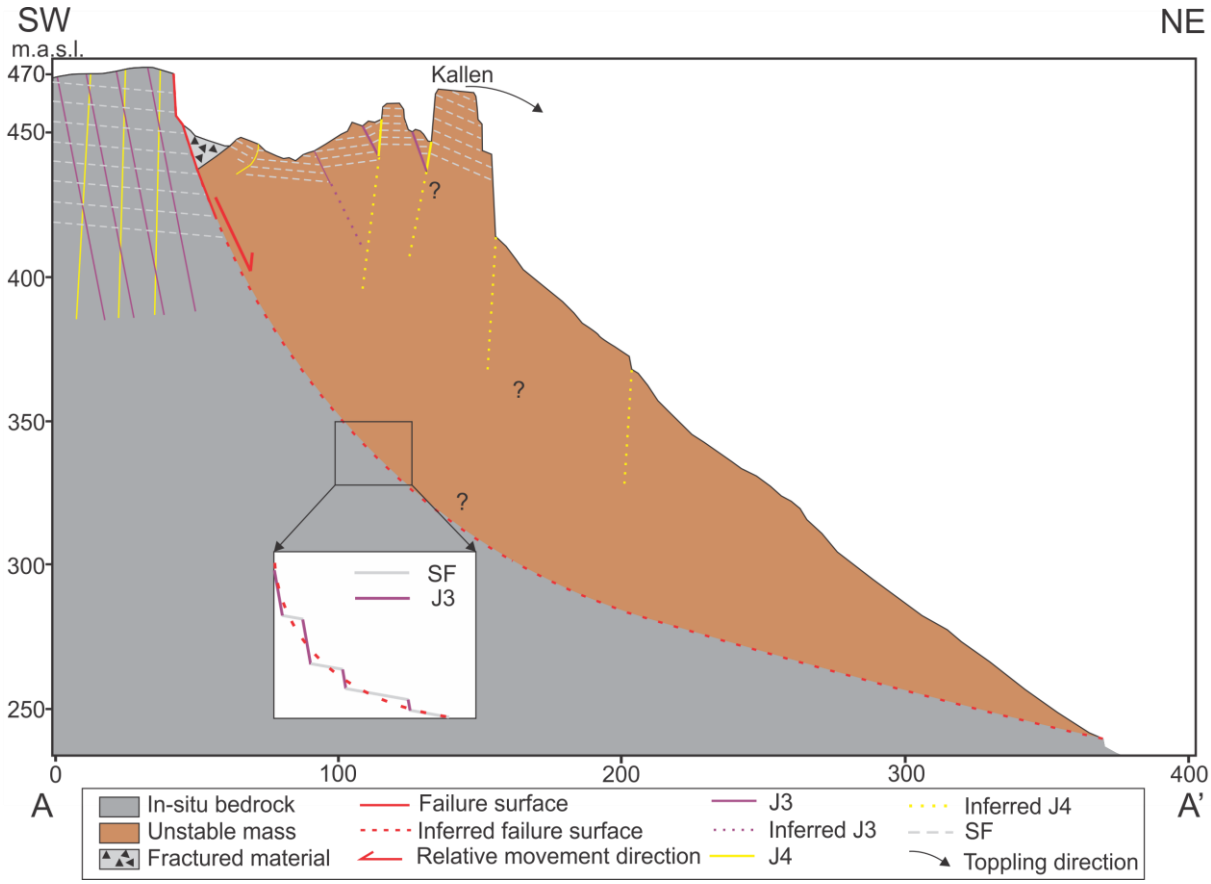

Figure 69: Schematic profile across the unstable area. Modified after Trønnes (2019).

The southern terrace of the URS is separated from the rest of the unstable mass by a major NE-SW striking scarp made from J1 and J2 joints (Figure 70), where J1 is the most prominent. The sense of movement appears to be similar to the NE-SW striking backscarp, where there has been an opening, resulting in the main trench and has tilted the southern terrace down towards SE. The opening along the NE-SW striking scarp within the unstable area is at a smaller scale and has resulted in the minor trench and promotes a toppling failure of the southern terrace towards SE. The front of the southern terrace is showing signs of fresh rock fall processes as a result of the tilt (Figure 70) and is likely the cause of frequent rockfalls from this area. Local stories from the 1950s indicate that a collapse from a tall rock column called “Kjærringa” occurred from this area.

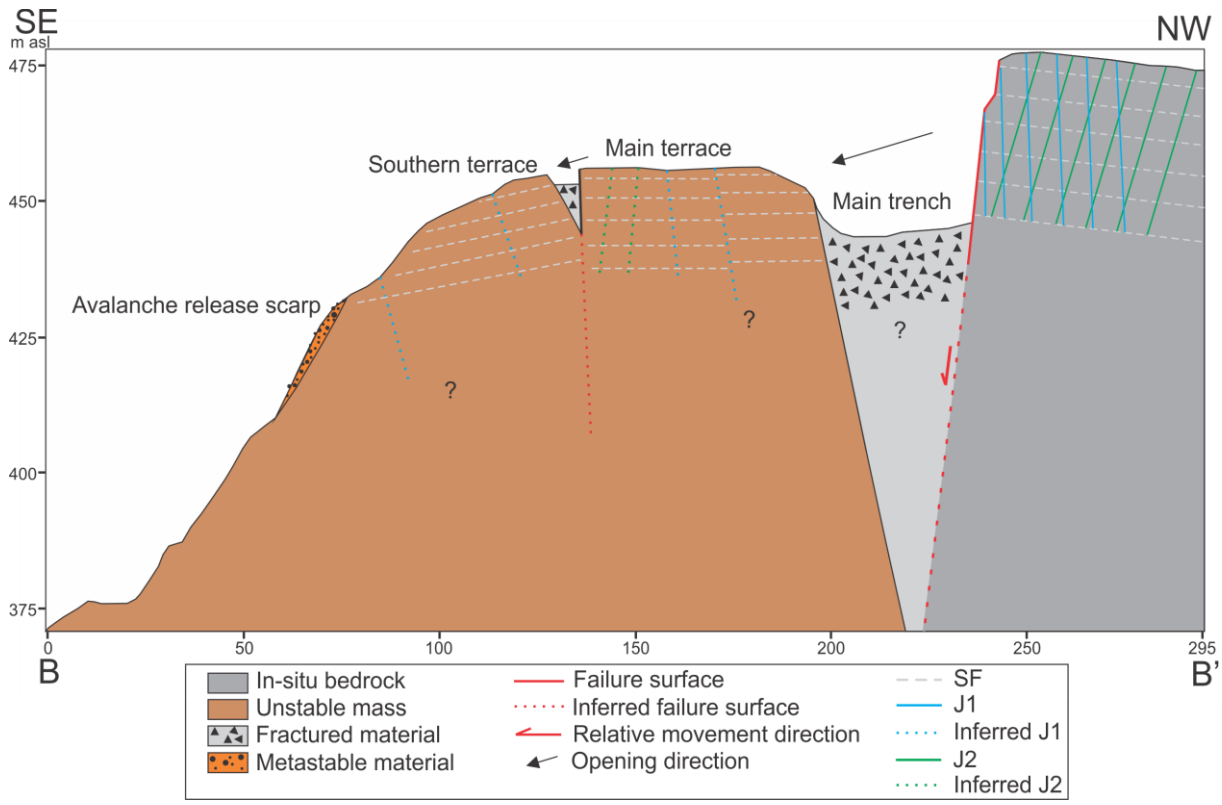

Figure 70: Schematic profile. Modified after Trønnes (2019).

4.2.5 Structural data validation

Field measurements show clear clusters in stereonet, which have been assigned to four joint sets that also were observed with confidence during fieldwork. Some clusters of poles are still outside the 1σ variability cone, mostly around the J1 and J4 quadrants. The clusters could indicate variabilities within and around J1 and J4. It is indicated by Indrevær et al. (2013) that large variabilities in strike on regional geological structures, especially those corresponding to J1 and J2, striking NE-SW to NNE-SSW. There is some crossover between the steepest foliation and the gentle planes along J3, striking NW-SE, due to the similar dip angles. The likely cause for this is because J3 was observed to refract along the foliation, so that it appeared both steep and gentle. The large variability within and outside the 1σ cones could indicate that more joint sets are present. Such a scenario would increase the structural complexity of the URS.

4.2.6 Movement measured by InSAR data

InSAR-derived displacement data can be related to morphostructural elements of the URS to better understand the controlling factors of the active deformation of the URS. Both Ascending satellites show movement rates that are coinciding well with the mapped morphostructures in the unstable area at Skredkallen (Figure 65 B). They generally show the

same displacement pattern across the URS, even though the Ascending 2 satellite in general show higher displacement rates. The differences between displacement rates displayed from respectively the Ascending 1 and 2 satellites could be explained from a difference in LOS, indicating that the gentler LOS for the Ascending 2 satellite is closer to the actual movement vector, which must be more eastward and have a steeper plunge angle. A significant change in displacement rate occurs downslope of the area delimited by the backscarps. The two areas (polygon 1 and 2) above the backscarp show displacement rates lower than 1 mm a^{-1} and are close to the lower detection limit for long time series (Bredal, 2016). The two polygons located upslope of the backscarps (1 and 2) display rates less than 1 mm a^{-1}. These may therefore not reflect genuine geological processes. In contrast, all areas below the backscarp show displacement rates above the detection limit.

The central parts of the unstable area (polygon 3, 5 and 6) show steady displacement rates of approximately -2 mm a^{-1}, indicating that these areas are actively deforming. The southern terrace, separated from the main terrace by a NE-SW striking scarp show a distinctively higher displacement rate, indicating that the scarp is highly active. These measures matches field observations as fresh release scarps was observed in this area.

The two columns in the northern part of the unstable area (polygon 6 and 7) show large variations in displacement rates. The much higher displacement rates could support the local stories that the columns were close enough to jump from one another in the late 19th century. It also indicates that the rock column is controlled by a structure in the morphological depression separating Kallen from the rest.

Only Ascending InSAR-datasets were used due to their favourable LOS for detecting downslope movement. When only ascending datasets are used, movement in LOS only is detected, and is therefore likely to underestimate the actual displacement.

4.3 Failure of Skrea

The distinct disruption of the N-S striking Laukvikfjellet ridgeline where Skredkallen is situated indicates a source area for previous rock avalanche(s). Previous rock avalanche event(s) would likely have failed by the same mechanisms as observed at the current URS, as the previous URS would have had the same structures and structural intersections. The geometry of previous URS would therefore likely have the step-path morphology now seen on Skredkallen. As seen in Figure 71, the assumed failed area is located between the backscarp and the assumed pre-failure ridgeline. The assumed pre-failure ridgeline is mapped

as a continuation of the current ridgeline which is otherwise consistent. The backscarp of the previous URS would likely have been along the inactive backscarps seen today, and along the front of the current URS. The detachment along the backscarp has likely been triggered by glacial debutressing, but the failure(s) of the area could also be a result of other mechanisms which is further discussed in section 4.4.5.

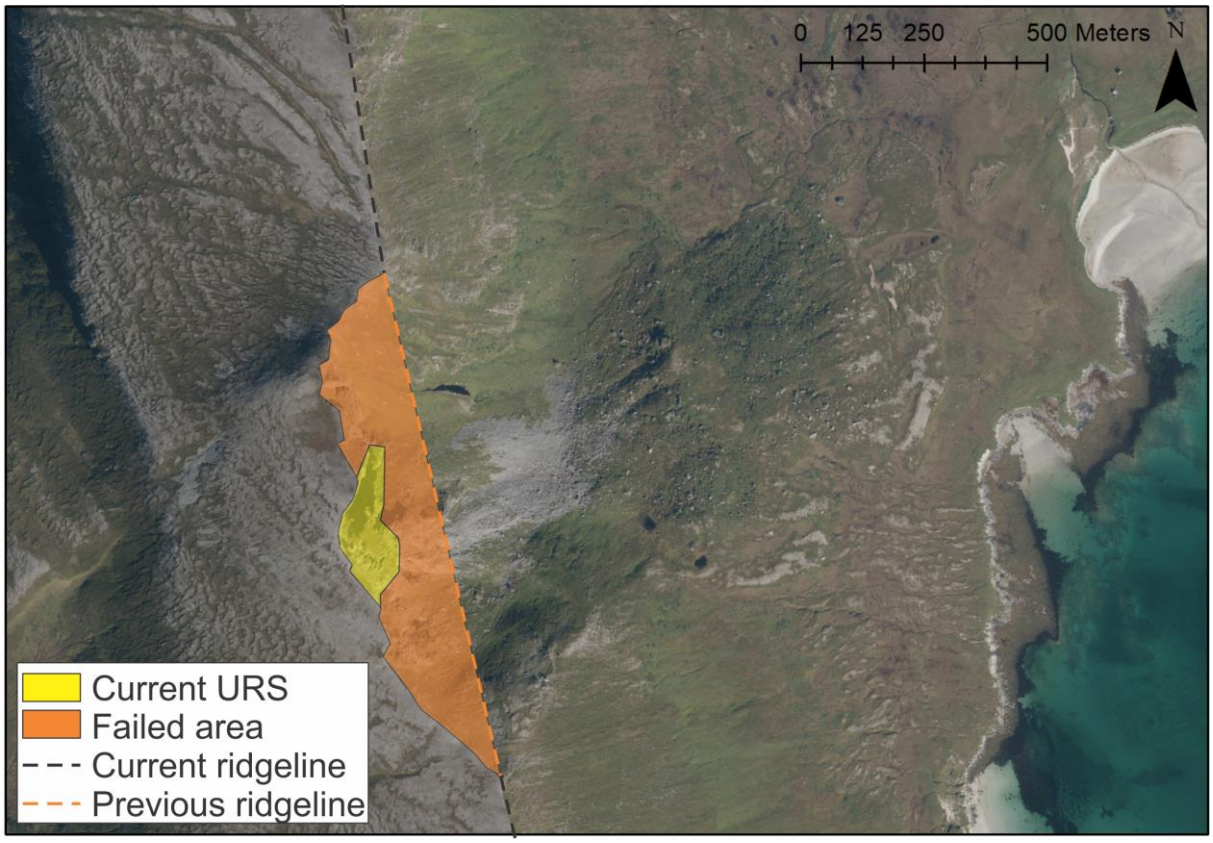

Figure 71: Map illustrating the assumed source area for previous rock avalance event(s) and the current unstable area as polygons. The stipled lines show the current and assumed pre-failure ridgeline. Orthophoto obtained from (Kartverket, 2019).

4.4 Evolution of the area

This chapter discusses the timing of the different events of the study area and their interaction in order to establish an evolutionary timeline of the area.

4.4.1 Validation of ^{14}C dating

The ^{14}C dates provide an accurate time of deposition of the sediments deposited in the pond, however they do not confirm the relative dating observations. The dates were in stratigraphic order, with the deepest sediments dated as the oldest- 1642 cal BP. This indicates that the sediments have not been disturbed by subsequent snow or rock avalanche events. It was difficult to determine if the bottom of the core was in fact also the bottom of the pond, and it may be the case that there are more sediments below the base of the core, which were frozen

and impenetrable at the time of coring. In addition, boulders could be present within the strata stopping the corer from reaching deeper sediments.

This could explain the age difference of the dated sediments and the proposed timing of the main RSF. However it may also be true that the lake was dammed by a more recent failure event in a multi-failure event scenario, which we will discuss futher in a later section. More sediment cores for dating are required to further explore these theories, however could not be done during this study due to complications during coring.

It also must be confirmed that the lake was formed by a RSF event and not another later process such as snow avalanching forming a pit.

4.4.2 Broad overview of the evolution

Vannøya has had a dynamic Holocene period resulting in the complex geomorphology presented in this thesis. Deglaciation of the island occurred between 15-13 ka (Corner and Haugane, 1993). At this time sea level was at the ML, now mapped at 47 m asl in our area of interest. A period of colder and relatively drier climate lead to the YD period, which was characterised by a glacial advance of the ice sheet resulting in the formation of moraines that are mapped in inner Troms. The advance did not reach Vannøya but correspond with the Main shoreline ca. 11-10 ka (Corner and Haugane, 1993), a distinct erosional notch in the landscape of the mapping area at 21-22 m asl. After a retreat ending the YD, a marine transgression occurred which resulted in the erosion of the Tapes shoreline. The transgression exposed the terrace below the Main shoreline, which allowed for the accumulation of organic material forming the widespread peatlands that are seen today. The Tapes shoreline is less distinct that the Main, forming an erosional knickpoint at 12 m asl in the mapping area.

This evolution of the area, based on both literature and observation provides a background for the discussion of the timing of failure events and the proposal of several scenarios which fit.

The two main bounding events of the evolutionary timeline are the deglaciation (deposits older than this would be removed by the ice sheet, assuming a warm-based ice), and the ^{14}C dates which provide a minimum age.

To examine the time gap between these two limits, some key questions need to be addressed:

- Have there been one or multiple failure events?
- Are there cross-cutting relationships between the erosional landforms and the RSF deposits?
- Why do the characteristics of the RSF deposits change with distance from the source?

4.4.3 Detailed evolution of the failure area

To examine the evolution of the area in more detail, the interaction between marine processes and the RSF deposits must be considered (Figure 72). Three different timing scenarios are presented in this discussion, according to the geological events taking place over the Holocene:

1. A RSF at the time of, or shortly after, deglaciation (Figure 73 A).
2. A RSF before the YD, but after deglaciation (Figure 73 B).
3. A RSF event before the Tapes transgression, but after the YD (Figure 73 C).

A failure before or simultaneously with the ML event could fit well with the geometry of the RSF deposits, as the sea level almost reached the base of the inner domain. In this case, the steep slope along the front of the inner domain could be explained as an erosional feature. However, if the RSF deposits beneath the inner domain were affected by marine erosional processes, a smooth curve/coastline should be expected across the RSF deposits. The modelled ML shoreline generally fits a smooth curve along the foot of Laukvikfjellet (Figure 15). The sharp contrast between the smooth curve along the E-facing slope of Laukvikfjellet and across the RSF deposits (Figure 73 D) indicates that a pre/syn ML failure scenario is unlikely. Also, no marine deposits or signs of erosion were observed within the RSF deposits at this elevation during fieldwork.

Scenario 2, where the deposition occurred as the sea-level was between the ML and the Main Shoreline could be more likely as eroded areas along the flank of the RSF deposits are found between these elevations. Also, the modelled sea-level across the RSF deposits during YD (Figure 73 B, sea level at the present-day 22 m contour line) mostly follows the front of the middle domain, indicating that the front could be an erosional feature. This hypothesis is supported by the fact that most radial ridges within the middle domain end abruptly at this point. This would put the timing of the RSF event shortly after deglaciation. This scenario corresponds with studies suggesting that the peak of Holocene rock slope failure activity

occurred soon after deglaciation (Cruden and Hu, 1993, Ballantyne et al., 2014, Hermanns et al., 2017). Additionally, in this scenario the sea-level covers all deposits making up the outer domain, which could explain the geomorphological contrast between the middle and outer domain. A deposition of the outer domain below sea-level could explain the flatter, more widespread character of these deposits. As the sea-level dropped through time, the morphologically depressed areas within the outer domain could have been present as lagoons and the sandy pits as sand dunes. Wave erosion and tidal currents could transport the most distal deposits, which could explain the boulders located outside the front (Figure 48). In this scenario, the deposits could also have been deposited on land, and later been submerged and eroded during the Tapes transgression.

Scenario 3, where the deposition occurred after the YD, when the sea-level was between the Main and Tapes shorelines, is supported by the presence of marine sediments in the outer domain. The steep front of the outer domain corresponds well with the elevation of the Tapes shoreline (Figure 73 C and D). An interaction between the Tapes shoreline and the RSF deposit is supported by the much smoother modelled coastline across the RSF deposits in Figure 73 D, which could be a result of marine erosion. However, these observations could also support the previously mentioned scenario where the deposition occurred before the YD when the sea-level was between the ML and Main shoreline. The observation of marine erosion of the deposits by the Main shoreline contradict this hypothesis, making a post-YD failure scenario unlikely.

Based on all these observations, it is proposed that the RSF occurred between deglaciation and the YD. Given that observed lag time between deglaciation and slope failure in other parts of Norway (Hermanns et al., 2017), we propose that the failure occurred 13-11 ka.

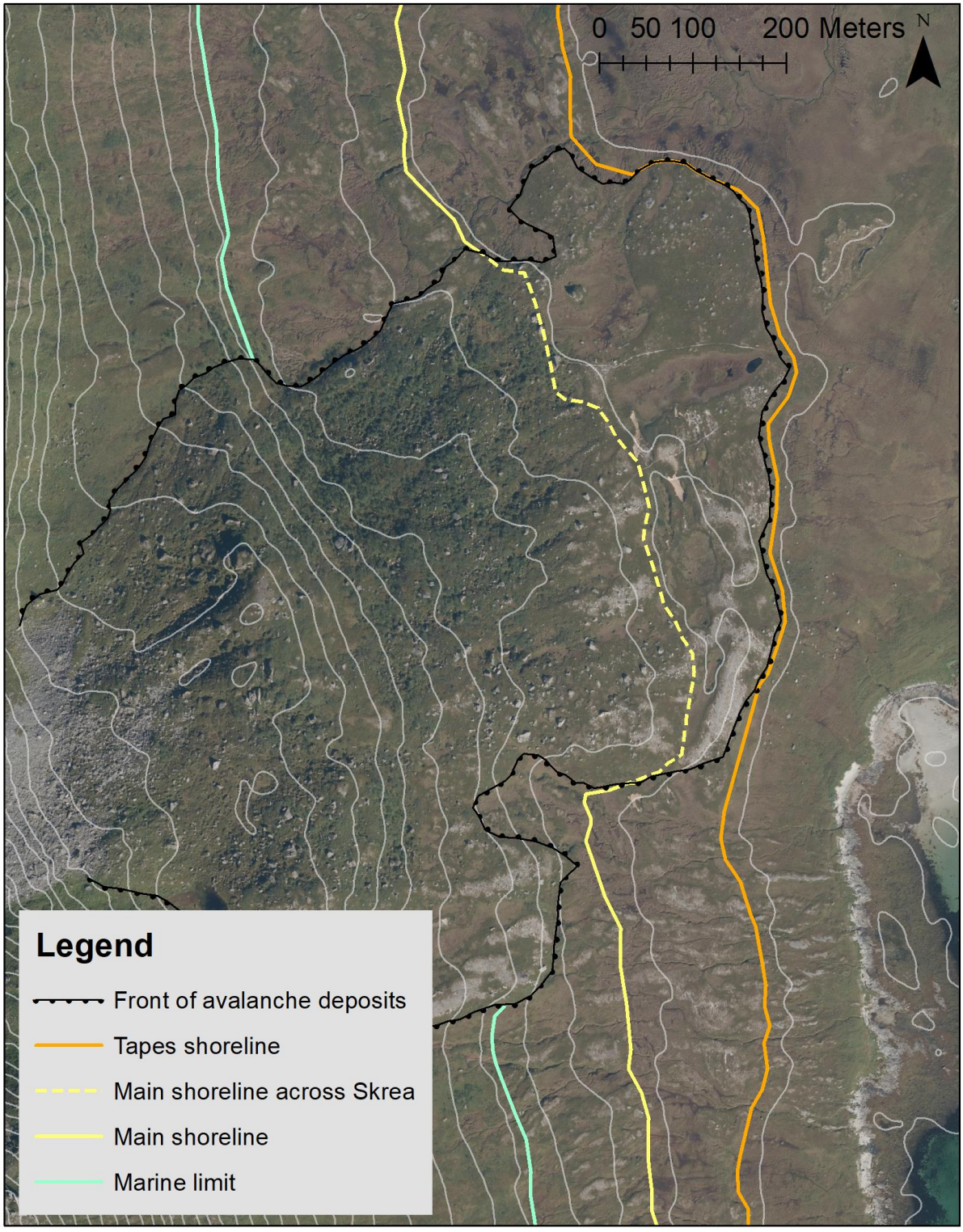

Figure 72: Illustration of the different shorelines used in this discussion, overlaid on Troms 2016 aerial images (Kartverket, 2019). Dashed lines illustrate modelled shorelines across the RSF deposits. Shorelines are based on 47, 22 and 12 m contours extracted from the 2 m resolution ArcticDEM.

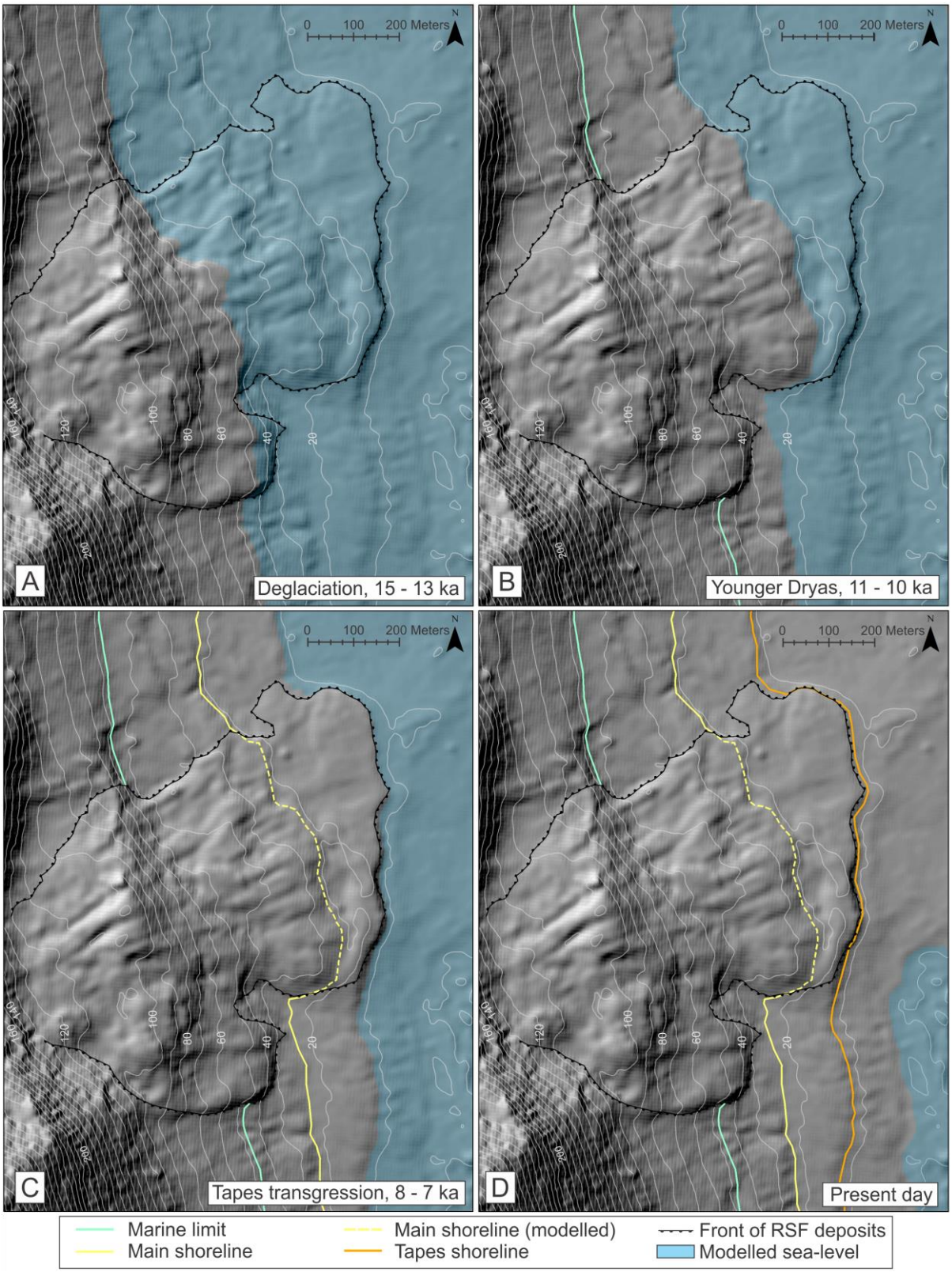

Figure 73: Modelled sea-level over time in the mapping area. A: ML, B: Main shoreline and C: Tapes shoreline. D: Present day sea level, reference to the previous sea-levels and with the extent of the RSF deposits. Background: Hillshade with 2m resolution and contour lines with an equidistance of 10 m.

4.4.4 Single or multiple failure events?

The possibility for multiple failure events at Skredkallen must be considered when analysing the RSF deposits. Four scenarios are discussed here, and illustrated based on the profile line shown on Figure 74. The gap of time between the proposed RSF event (c. 13-11 ka), and the deposition of the dated lake sediments on top of the RSF deposits (c. 1.7 ka) suggests that multiple failures may have occurred. As the sediments were extracted from the inner domain of the RSF, it could suggest that the inner domain has been deposited as one later event (scenario presented in Figure 75 A). However, no data or observations confirm this hypothesis. Slopes do not always fail as one catastrophic mass but rather a series of smaller events (e.g. the Loen disasters of 1905, 1936 and 1950 (Grimstad, 2006)), a scenario here whereby multiple, smaller failures form the inner domain is just as likely. Smaller volumes may stack on top of each other, forming the abrupt change in slope at the front of this domain (Figure 75 B). Temporally, the possibility of one or multiple failures occurring later in time is supported by data- Blikra et al. (2006) showed large rock avalanche activity in western Norway in the last 5,000 years, with a peak activity around 3000 years BP.

In the third scenario a failure event for each domain is proposed. The outer domain was therefore deposited by one RSF event, which occurred sometime between deglaciation and YD, and the deposits making up the middle and inner domains were deposited during two later RSF events (Figure 75 C). However, it is unlikely that the middle and outer domain were deposited separately as they both exhibit signs of marine erosion which the inner domain does not.

Lastly, a scenario whereby all RSF deposits were deposited during one catastrophic failure event must also be considered (Figure 75 D). The different characteristics of the different domains must then be explained by another process. The radial ridges which are only present on the inner and middle domains may be explained by the dynamics of the emplacement event. The heavily eroded and washed appearance of the outer domain is likely a result of erosion. The steep front of the inner domain could also be a result of the geometry of the underlying bedrock (illustrated on Figure 75 D). However for this scenario to be possible, the lake from which the sediment core was taken must have formed as a result of a later, geological process to explain the long time gap between the failure event and the age of the sediments.

Based on this discussion, the two first scenarios are considered the most likely (Figure 75 A and B).

Figure 74: Location for the profiles presented below. Orthophoto obtained from Kartverket (2019).

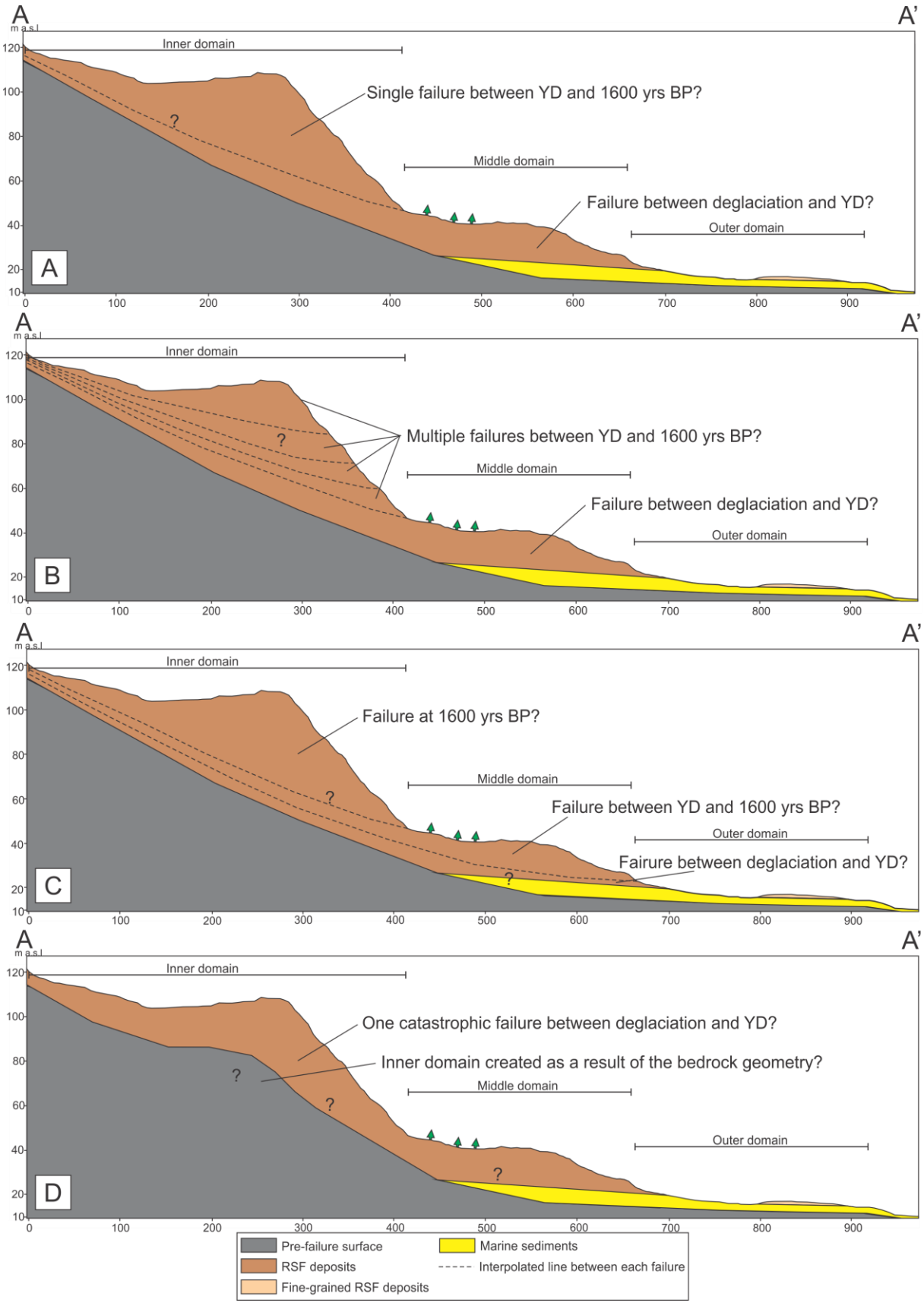

Figure 75: Elevation profiles with an exaggerated elevation profile by a factor of 2.25. The profiles illustrate discussed failure scenarios. A: Illustrating a scenario where the mid- and outer domains are deposited during a post deglaciation/pre YD failure and the inner domain at c. 1600 yrs BP. B: A scenario where the mid- and outer domains are deposited during a post deglaciation – pre YD failure, and the inner domain as multiple smaller

failures, stacking up to form the inner domain. C: A scenario where each domain is formed as a result of a failure event. D: A single catastrophic failure scenario.

4.4.5 Controlling factors

Many of the historic rock slope failures between deglaciation and YD occurred the first thousand years after deglaciation, indicating that deglaciation is one of the prime conditioning factors for large rock-slope failures (Hermanns et al., 2017). The timing suggests that glacial debutressing could support a large-scale catastrophic rock slope failure (Ballantyne, 2002). Glacial oversteepening of the rock slope during glaciations could also be an external factor. The stress release from debuttressing could have resulted in propagation of the internal network of joints and to a loss of cohesion in the existing discontinuities. The internal network of joints and shear zones are probably the most prone surfaces to weathering on Skredkallen, meaning they might play an extra role on defining the main sliding surfaces.

The downflow of cold, dense air into the deep main trench combined with little incoming sunlight decreases the local temperature. The local climate within the main trench could therefore favour sporadic permafrost. This is supported by observations during the coring trip in March 2019, where large overhanging cornices existed along the whole backscarp. The collapsing of the cornices during spring provides extra snow accumulation in the trench and is a great source of ice. In terms of possible rock-slope failures between YD and 1600 yrs BP, several historic rock slope failures have been dated in Norway by Hermanns et al. (2017) around 8.5 ka, which is close to the period as Norway was at its warmest and often referred to as the climate maximum. The warmer climate could lead to permafrost thawing, which may cause a destabilization of the URS (Christiansen et al., 2010).

As Skredkallen is located on the coast of Troms, the precipitation rates can be very high in rainfall periods. Displacement rates measured by InSAR (Appendix A) indicates that deformation is largest during in late spring (June) and early autumn (September). The heavily soliflucted surroundings indicates that water in the soil is trapped by the underlying permafrost. There are no streams or ground water seepage observed on or around the unstable area, meaning only local precipitated water and snow melt affects the slope stability. Due to the heavily fractured nature of the unstable area, it is likely to have a high secondary permeability, meaning that water percolating through the slope is likely to be channeled through the unstable part of the slope. The presence of streams beneath the talus zone indicates that groundwater seepage might be present in the lower area, supporting that water is channelized through the failure zone and out at the toe.

The potential presence of groundwater within the fractures will influence the stability of the rock mass by increasing pore pressure, lowering effective stress and the stability of the slope (Wyllie and Mah, 2014). Freezing and thawing processes also needs to be addressed as a potential controlling factor. Freezing can block drainage patterns of ground water, resulting in a build-up of groundwater and increases in pore pressure, destabilizing the rock mass (Wyllie and Mah, 2004). Volume expansion of water during freezing could lead to ice wedging. This process will expand existing fractures and contribute to breaking of rock bridges. Water and ice may therefore be one of the main controlling factors on Skredkallen.

Isostatic rebound following deglaciation of the continental shelf can lead to earthquakes which can trigger rock-slope failures or bring about the onset of a rockslide. It takes at least an earthquake of 6.0 in magnitude to trigger a rock slide according to Keefer (1984). Earthquakes above a Magnitude of 5.5 are rare in Norway (Dehls et al., 2000), but doesn't exclude the chance of a pre-historic large scale earthquake (Braathen et al., 2004). An earthquake event as a result of isostatic uplift (or tectonic processes) could have triggered the failure of Skrea, and/or could have led to the detachment of Skredkallen.

4.4.6 Volume estimation

The estimated volume of Skrea is 13 Mm^3, considerably larger than the estimated volume of the currently unstable area- 1.1 Mm^3 Trønnes (2019). This is consistent with the markedly larger assumed source area for the event, as outlined in (Figure 71). As most rock avalanches in Norway usually require larger volumes than the volumes corresponding with the best-fit curve from (Scheidegger, 1973; Blikra et al., 2001), it is likely that the volume estimate from Chapter 3.7 represents a minimum. Marine erosion could have affected the extent of the RSF deposits, and therefore the measured run-out distance today. This would change the volume calculation based on the empirical Scheidegger method. If some material has been washed away, the rock blocks mapped outside the deposit boundary could represent the original extent. As some blocks are observed outside the boundary of the RSF deposits. However it can't be excluded that wavewash has actually transported the outermost deposits further away from the rest of the deposits.

4.4.7 Timeline

Based on the collected data and observations discussed above, a suggested timeline is constrained for the study area and presented in Figure 76.

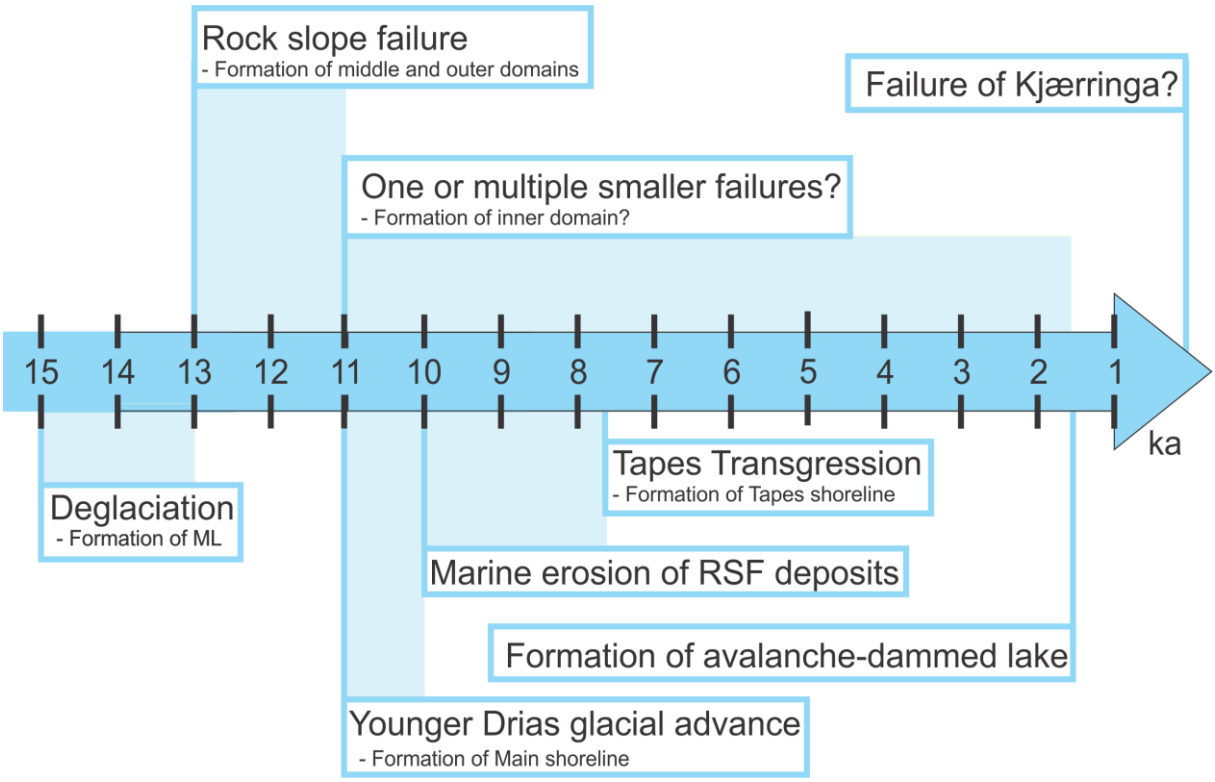

Figure 76: Timeline suggesting the evolution of the RSF at Skredkallen. Blue transparent blocks indicate window of time covered by variance in geochronology.

5 Conclusions

The main goal of this thesis has been to investigate the evolution of the URS and rock slope failure at Skredkallen. The geology and geomorphology of both the URS and the surrounding area has been investigated, and sediments have been dated in order to constrain a timeline of the study area.

The main findings of this work are:

- Based on field measurements, five geological structures have been found on Skredkallen: SF (292/14 ± 13.8), J1 (034/82 ± 16.9), J2 (203/66 ± 9.0), J3 (309/68 ± 10.5) and J4 (117/83 ± 15.5). J1, J3 and J4 are the most prominent structures on Skredkallen.
- Field observations suggest that J1 corresponds with the NE-SW striking morphostructures on Skredkallen, where an opening (toppling) sense of movement occurs.
- The NW-SE striking morphostructures is controlled by SF and J3. Sliding along both structures create step-path geometry and results in a biplanar compound slid, resulting in a horst-graben geometry of the URS.
- The column Kallen is controlled by J4 and is toppling towards the E.
- InSAR displacement rates coincides well with the mapped morphostructures and indicates that Kallen is the fastest moving area with displacement rates $\leq$12 mm a^{-1}.
- The general geomorphogy of the area indicates active erosional processes on Laikvikfjellet with steep areas of exposed bedrock, solifluction, fresh rockfall deposits and debris flow channels. The lowlands are relatively flat and dominated by peatlands and marine deposits.
- 3 marine shorelines are mapped in the lowlands. The highest (47 m asl) corresponds with the marine limit, formed during deglaciation (13 – 15 ka). The middle (22 m asl) corresponds with the Main shoreline, formed in the Younder Dryas (11 – 10 ka). The lowermost (12 m asl) corresponds with the Tapes shoreline, formed during the Tapes transgression (8 – 7 ka).
- The rock avalanche deposits stretches out for 1.4km from the unstable area and are characterized by 3 domains (inner, middle and outer) by geometry and run-out distance.

- Evidence of marine erosion and deposition are found in the RSF deposits up to elevations between the marine limit and Main shoreline, indicating a deposition of the RSF deposits between the formations of these two shorelines.
- The angle of reach of the RSF deposits corresponds to a volume of c. 13 Mm^3.
- ^{14}C dating of the lake sediments within the inner domain revealed an age of 1642 cal. yr BP.
- The most likely failure scenario is a failure of c. 13 Mm^3 between deglaciation and YD. One or multiple smaller failures have occurred after this failure, but before the formation of the dated lake 1642 cal. yr BP.

6 Future work

This study has been conducted in a poorly studied area. Future studies are necessary to fully understand the formation and current movement of the URS. To get a greater understanding of the evolution of the URS, more detailed geomorphological investigations around the RSF deposits will be advantageous. Additional ^{14}C dates from the avalanche-dammed lakes could give a better picture of when the lakes were formed. Also, cosmogenic nuclide dating of the boulders within the RSF deposits might give a more detailed picture of when they previous rock avalanche(s) occurred and how many failures. Cosmogenic nuclide dating could also be done along the backscarps and along the flanks of the unstable area to determine possible source area(s).

By using the software Flor-R, more detailed rock avalanche run-out assessment could be conducted (Oppikofer et al., 2016) in order to estimate the size(s) of previous rock avalanches. Further investigations using a drone could map the inaccessible areas in further detail and also generate high-resolution DEM's for mapping and volume estimation of the deposits and the unstable area. A detailed bedrock study of the area might be beneficial in order to better explain the lithological differences and how the regional geology could affect the URS. More detailed structural analysis could be beneficial in order as more joint sets could be present. It could also be beneficial in order to better understand the different failure mechanisms. By establishing ground-based InSAR at the base of the slope, 3D vectors of displacement could be obtained by combining the measurements with ascending and descending InSAR data (Eriksen et al., 2017).

Works cited

AGLIARDI, F., CROSTA, G. & ZANCHI, A. 2001. Structural constraints on deep-seated slope deformation kinematics. *Engineering Geology,* 59**,** 83-102.

AGLIARDI, F., CROSTA, G. B. & FRATTINI, P. 2012. 18 Slow rock-slope deformation. *Landslides: Types, mechanisms and modeling***,** 207.

ALLABY, M. 2013. *A dictionary of geology and earth sciences*, Oxford University Press.

AMBROSI, C. & CROSTA, G. B. 2006. Large sackung along major tectonic features in the Central Italian Alps. *Engineering Geology,* 83**,** 183-200.

ANDERSEN, B. 1968. Glacial geology of western Troms, north Norway: Geological Survey of Norway (NGU), v. 256.

ANDREASSEN, K., VORREN, T. O. & JOHANSEN, K. B. 1985. Pre-Late Weichselian glacimarine sediments at Arnøy, North Norway. *Geological Society of Sweden,* 107**,** 63-70.

ANDRESEN, A. & FORSLUND, T. 1987. Post-Caledonian brittle faults in Troms: geometry, age and tectonic significance. *The Caledonian and Related Geology of Scandinavia*.

ARCTICDEM. DigitalGlobe constellation. Available: https://www.pgc.umn.edu/data/arcticdem/ [Accessed 10.09.2019].

AUGUSTINUS, P. Rock mass strength and the stability of some glacial valley slopes. International Journal of Rock Mechanics and Mining Sciences and Geomechanics Abstracts, 1996. 28A-29A.

AUGUSTINUS, P. C. 1995. Glacial valley cross-profile development: the influence of in situ rock stress and rock mass strength, with examples from the Southern Alps, New Zealand. *Geomorphology,* 14**,** 87-97.

BAKKHAUG, I. 2015. *Undersøkelse av ustabilt fjellparti ved Adjet, Storfjord, Troms. Betydningen av ulike kategorier av glideplan i berggrunnen og mekanismer for utglidning.* Thesis from UiT The Arctic University of Norway.

BALLANTYNE, C. K. 2002. Paraglacial geomorphology. *Quaternary Science Reviews,* 21**,** 1935-2017.

BALLANTYNE, C. K. 2003. A Scottish sturzstrom: the Beinn Alligin rock avalanche, Wester Ross. *Scottish Geographical Journal,* 119**,** 159-167.

BALLANTYNE, C. K., SANDEMAN, G. F., STONE, J. O. & WILSON, P. 2014. Rock-slope failure following Late Pleistocene deglaciation on tectonically stable mountainous terrain. *Quaternary Science Reviews,* 86**,** 144-157.

BERGH, S. G., KULLERUD, K., ARMITAGE, P. E., BOUKE ZWAAN, K., CORFU, F., RAVNA, E. J. & INGE MYHRE, P. 2010. Neoarchaean to Svecofennian tectono-magmatic evolution of the West Troms Basement Complex, North Norway. *Norwegian Journal of Geology,* 90.

BERGH, S. G., KULLERUD, K., CORFU, F., ARMITAGE, P. E., DAVIDSEN, B., JOHANSEN, H. W., PETTERSEN, T. & KNUDSEN, S. 2007. Low-grade sedimentary rocks on Vanna, North Norway: a new occurrence of a Palaeoproterozoic (2.4-2.2 Ga) cover succession in northern Fennoscandia. *Norwegian Journal of Geology,* 87.

BINNS, R., CHROSTON, P. & MATHEWS, D. 1981. Low-grade sedi ments on Precambrian gneiss on Vanna. *Geological Survey of Norway (NGU)*.

BJØRKLID, E. 2017. *Strukturgeologisk og geomorfologisk studium av fjellskred ved Skredan, Tromsø kommune.* Thesis from UiT The Arctic University of Norway.

BLAAUW, M. & CHRISTEN, J. A. 2011. Flexible paleoclimate age-depth models using an autoregressive gamma process. *Bayesian analysis,* 6**,** 457-474.

BLIKRA, L., BRAATHEN, A. & SKURTVEIT, E. 2001. Hazard evaluation of rock avalanches; the Baraldsnes–Oterøya area. *Geological Survey of Norway (NGU), Report.*

BLIKRA, L., LONGVA, O., BRAATHEN, A., ANDA, E., DEHLS, J. & STALSBERG, K. 2006. Rock slope failures in Norwegian fjord areas: examples, spatial distribution and temporal pattern. *Landslides from massive rock slope failure.* Springer.

BLIKRA, L. H. & CHRISTIANSEN, H. H. 2014. A field-based model of permafrost-controlled rockslide deformation in northern Norway. *Geomorphology,* 208**,** 34-49.

BLIKRA, L. H., CHRISTIANSEN, H. H., KRISTENSEN, L. & LOVISOLO, M. 2015. Characterization, geometry, temporal evolution and controlling mechanisms of the Jettan Rock-Slide, Northern Norway. *Engineering Geology for Society and Territory-Volume 2.* Springer.

BLYSTAD, P. 1995. Structural elements of the Norwegian continental shelf. Part 2: The Norwegian Sea region. *NPD Bull.,* 8.

BRAATHEN, A., BLIKRA, L. H., BERG, S. S. & KARLSEN, F. 2004. Rock-slope failures in Norway; type, geometry, deformation mechanisms and stability. *Norwegian Journal of Geology,* 84.

BREDAL, M. 2016. *A structural, geomorphological and InSAR study of the unstable rock slope in Oksfjellet, Kåfjord, Troms.* Thesis from UiT The Arctic University of Norway.

BRIDEAU, M.-A. & STEAD, D. 2010. Controls on Block Toppling Using a Three-Dimensional Distinct Element Approach. *Rock Mechanics and Rock Engineering,* 43**,** 241-260.

BRONK RAMSEY, C. 2013. OxCal version 4.2. 4. *University of Oxford Radiocarbon Accelerator Unit. Computer Program. Available online at: http://c14.arch.ox.ac.uk/embed.php*.

BROWN, J., SIDLAUSKAS, F. J. & DELINSKI, G. 1997. *International permafrost association circum-Arctic map of permafrost and ground ice conditions,* The Survey.

BUNKHOLT, H., NORDAHL, B., HERMANNS, R. L., OPPIKOFER, T., FISCHER, L., BLIKRA, L. H., ANDA, E., DAHLE, H. & SÆTRE, S. 2013a. Database of unstable rock slopes of Norway. *Landslide science and practice.* Springer.

BUNKHOLT, H., OSMUNDSEN, P., REDFIELD, T., OPPIKOFER, T., EIKEN, T., L'HEUREUX, J., HERMANNS, R. & LAUKNES, T. 2011. ROS Fjellskred i Troms: status og analyser etter feltarbeid 2010. *Geological Survey of Norway (NGU) report,* 135.

BUNKHOLT, H., REDFIELD, T., OSMUNDSEN, P., OPPIKOFER, T., HERMANNS, R. & DEHLS, J. 2012. Landslide processes in hard rock in Troms, Norway. *Landslides and Engineered Slopes: Protecting Society through Improved Understanding. Taylor & Francis Group, London***,** 855-861.

BUNKHOLT, H., REDFIELD, T., OSMUNDSEN, P. T., OPPIKOFER, T., HERMANNS, R. L. & DEHLS, J. 2013b. The role of inherited structures in deep seated slope failures in Kåfjorden, Norway. *Landslide Science and Practice.* Springer.

CHRISTIANSEN, H. H., ETZELMÜLLER, B., ISAKSEN, K., JULIUSSEN, H., FARBROT, H., HUMLUM, O., JOHANSSON, M., INGEMAN‐NIELSEN, T., KRISTENSEN, L. & HJORT, J. 2010. The thermal state of permafrost in the Nordic area during the International Polar Year 2007–2009. *Permafrost and Periglacial Processes,* 21**,** 156-181.

CORNER, G. & EILERTSEN, R. 2008. Raised beaches, falling-stage deltas, river terraces and postglacial fjord-valley fill, arctic Norway. Excursion guide.

CORNER, G. D. 1980. Preboreal deglaciation chronology and marine limits of the Lyngen - Storfjord area, Troms, North Norway. *Boreas,* 9**,** 239-249.
CORNER, G. D. 2005. Atlantic coast and fjords. *The physical geography of Fennoscandia,* 5**,** 203-228.
CORNER, G. D. 2006. A transgressive-regressive model of fjord-valley fill: stratigraphy, facies and depositional controls.
CORNER, G. D. & HAUGANE, E. 1993. Marine-lacustrine stratigraphy of raised coastal basins and postglacial sea-level change at Lyngen and Vanna, Troms, northern Norway. *Norwegian Journal of Geology,* 73**,** 175-197.
COROMINAS, J. 1996. The angle of reach as a mobility index for small and large landslides. *Canadian Geotechnical Journal,* 33**,** 260-271.
CRUDEN, D. & HU, X. 1993. Exhaustion and steady state models for predicting landslide hazards in the Canadian Rocky Mountains. *Geomorphology,* 8**,** 279-285.
CUNDALL, P. A. A computer model for simulating progressive, large-scale movement in blocky rock system. Proceedings of the International Symposium on Rock Mechanics, 1971, 1971.
DEHLS, J. F., OLESEN, O., OLSEN, L. & BLIKRA, L. H. 2000. Neotectonic faulting in northern Norway; the Stuoragurra and Nordmannvikdalen postglacial faults. *Quaternary science reviews,* 19**,** 1447-1460.
ERIKSEN, H., ROUYET, L., LAUKNES, T., BERTHLING, I., ISAKSEN, K., HINDBERG, H., LARSEN, Y. & CORNER, G. 2018. Recent acceleration of a rock glacier complex, Adjet, Norway, documented by 62 years of remote sensing observations. *Geophysical Research Letters,* 45**,** 8314-8323.
ERIKSEN, H. Ø. 2013. *Slope displacement patterns observed using satellite InSAR data in the Storfjord-Kåfjord-Lyngen region, Troms.* Thesis from UiT The Arctic University of Norway.
ERIKSEN, H. Ø., BERGH, S. G., LARSEN, Y., SKREDE, I., KRISTENSEN, L., LAUKNES, T. R., BLIKRA, L. H. & KIERULF, H. P. 2017. Relating 3D surface displacement from satellite-and ground-based InSAR to structures and geomorphology of the Jettan rockslide, northern Norway.
FORSLUND, T. 1988. Post-Kaledonske forkastninger i Vest-Troms, med vekt på Kvaløyslettaforkastningen, Kvaløya. *Unpublished master thesis, University of Tromsø.*
GIARDINO, J. R., SHRODER, J. F. & VITEK, J. D. 1987. *Rock glaciers*, Allen & Unwin London.
GISNÅS, K., ETZELMÜLLER, B., LUSSANA, C., HJORT, J., SANNEL, A. B. K., ISAKSEN, K., WESTERMANN, S., KUHRY, P., CHRISTIANSEN, H. H. & FRAMPTON, A. 2017. Permafrost map for Norway, Sweden and Finland. *Permafrost and Periglacial Processes,* 28**,** 359-378.
GLASTONBURY, J. & FELL, R. 2008. Geotechnical characteristics of large slow, very slow, and extremely slow landslides. *Canadian Geotechnical Journal,* 45**,** 984-1005.
GLASTONBURY, J. & FELL, R. 2010. Geotechnical characteristics of large rapid rock slides. *Canadian Geotechnical Journal,* 47**,** 116-132.
GOODMAN, R. E. Toppling of rock slopes. Proc. Speciality Conference on Rock Engineering for Foundation and Slopes, 1976. ASCE, 201-234.
GRIMSTAD, E. 2006. The Loen rock slide–an analysis of the stability. *Mitochondrial Medicine***,** 129.
HANNUS, M. 2012. *Structural geometry and controlling factors for a rock slope failure area at Hompen/Váráš, Signaldalen, Troms, North Norway.* Thesis from UiT The Arctic University of Norway.

HANSEN, J.-A. & BERGH, S. G. 2012. Origin and reactivation of fracture systems adjacent to the Mid-Norwegian continental margin on Hamarøya, North Norway: use of digital geological mapping and morphotectonic lineament analysis. *Norwegian Journal of Geology*, 92.
HARRIS, S. A., FRENCH, H. M., HEGINBOTTOM, J. A., JOHNSTON, G. H., LADANYI, B., SEGO, D. C. & EVERDINGEN, R. O. V. 1988. Glossary of permafrost and related ground-ice terms. *Associate Committee on Geotechnical Research, National Research Council of Canada, Ottawa*, 156.
HERMANNS, R. L. & LONGVA, O. 2012. Rapid rock-slope failures. *Landslides: types, mechanisms and modeling***,** 59-70.
HERMANNS, R. L., SCHLEIER, M., BÖHME, M., BLIKRA, L. H., GOSSE, J., IVY-OCHS, S. & HILGER, P. Rock-avalanche activity in W and S Norway peaks after the retreat of the Scandinavian Ice Sheet. Workshop on World Landslide Forum, 2017. Springer, 331-338.
HERNES, I. 2014. *Fjellskred ved Indre Nordnes, Nordnesfjellet, Lyngen, Troms-Berggrunnens indre struktur og bevegelsesmekanismer basert på strukturell analyse og overvakingsdata.* Thesis from UiT The Arctic University of Norway.
HIGHLAND, L. & BOBROWSKY, P. T. 2008. *The landslide handbook: a guide to understanding landslides*, US Geological Survey Reston.
HUNGR, O., LEROUEIL, S. & PICARELLI, L. 2014. The Varnes classification of landslide types, an update. *Landslides*, 11**,** 167-194.
HUSBY, E. D. 2011. *Fjellskred i Nomedalstinden: en strukturstyrt masseutglidning på et underliggende storskala glideplan.* Thesis from UiT The Arctic University of Norway.
HØGAAS, F., HANSEN, L., RINDSTAD, B., SVEIAN, H. & OLSEN, L. 2012. Database for registrering av marine grense (MG) i Norge. *Geological Survey of Norway (NGU) report*.
INDREVÆR, K., BERGH, S. G., KOEHL, J.-B., HANSEN, J.-A., SCHERMER, E. R. & INGEBRIGTSEN, A. 2013. Post-Caledonian brittle fault zones on the hyperextended SW Barents Sea margin: New insights into onshore and offshore margin architecture. *Norwegian Journal of Geology*, 93.
JARMAN, D. 2006. Large rock slope failures in the Highlands of Scotland: characterisation, causes and spatial distribution. *Engineering Geology*, 83**,** 161-182.
JØRGENSEN, P., SØRENSEN, R. & HALDORSEN, S. 1997. *Kvartærgeologi*, Norges landbrukshøgskole, Tun Forlag.
KARTVERKET. 2019. *Kartverket* [Online]. Kartverket. Available: www.kartverket.no [Accessed 15.01.2019].
KEEFER, D. K. 1984. Landslides caused by earthquakes. *Geological Society of America Bulletin*, 95**,** 406-421.
KING, L. 1986. Zonation and ecology of high mountain permafrost in Scandinavia. *Geografiska Annaler: Series A, Physical Geography*, 68**,** 131-139.
KJELLMAN, S. E., AXELSSON, P. E., ETZELMÜLLER, B., WESTERMANN, S. & SANNEL, A. B. K. 2018. Holocene development of subarctic permafrost peatlands in Finnmark, northern Norway. *The Holocene*, 28**,** 1855-1869.
KLIMASERVICESENTER, N. 2019. *Norsk Klimaservicesenter* [Online]. Available: https://seklima.met.no/observations/ [Accessed 23.10.2019].
LAUKNES, T. R. 2011. Rockslide mapping in Norway by means of interferometric SAR time series analysis.
MANGERUD, J., GYLLENCREUTZ, R., LOHNE, Ø. & SVENDSEN, J. I. 2011. Glacial history of Norway. *Developments in Quaternary Sciences.* Elsevier.

NESJE, A., SJØSTRØM, K. & BJØRSETH, E. 2012. *Brelære: bre, landskap, klimaendringer og datering*, Kristiansand, Høyskoleforlag.
NGU. 2019a. *InSAR Norway* [Online]. NGU. Available: https://insar.ngu.no/ [Accessed 15.09.2019].
NGU. 2019b. *Løsmasser og marin grense* [Online]. Geological Survey of Norway. Available: http://geo.ngu.no/kart/losmasse_mobil/ [Accessed 11.09.2019].
NGU. 2019c. *Ustabile fjellparti - Nasjonal database for ustabile fjellparti* [Online]. Available: http://geo.ngu.no/kart/ustabilefjellparti_mobil/ [Accessed 18.01.2019].
NOPPER, H. 2015. *Geomorphological study of the rock-slope failure at Adjet, Storfjord, Troms.* Thesis from UiT The Arctic University of Norway.
OLESEN, O., PASCAL KIERULF, H., BRÖNNER, M., DALSEGG, E., FREDIN, O. & SOLBAKK, T. 2013. Deep weathering, neotectonics and strandflat formation in Nordland, northern Norway. *Norwegian Journal of Geology*, 93.
OLESEN, O., TORSVIK, T. H. & TVETEN, E. 1997. Basement structure of the continental margin in the Lofoten-Lopphavet area, northern Norway: constraints from potential field data, on-land structural mapping and palaeomagnetic data. *Oceanographic Literature Review*, 12**,** 1478.
OPHEIM, J. & ANDRESEN, A. 1989. Basement-cover relationships on northern Vanna, Troms, Norway. *Norwegian Journal of Geology*, 69**,** 67-81.
OPPIKOFER, T., HERMANNS, R. L., SANDØY, G., BÖHME, M., JABOYEDOFF, M., HORTON, P., ROBERTS, N. J. & FUCHS, H. 2016. Quantification of casualties from potential rock-slope failures in Norway. *Landslides and Engineered Slopes: Experience, Theory and Practice***,** 1537-1544.
OPPIKOFER, T., SAINTOT, A., HERMANNS, R., BÖHME, M., SCHEIBER, T., GOSSE, J. & DREIÅS, G. 2017. From incipient slope instability through slope deformation to catastrophic failure—Different stages of failure development on the Ivasnasen and Vollan rock slopes (western Norway). *Geomorphology*, 289**,** 96-116.
OTTESEN, D., DOWDESWELL, J. & RISE, L. 2005. Submarine landforms and the reconstruction of fast-flowing ice streams within a large Quaternary ice sheet: the 2500-km-long Norwegian-Svalbard margin (57–80 N). *Geological Society of America Bulletin*, 117**,** 1033-1050.
PETTERSEN, K. 1887. *Den nord-norske fjeldbygning*, Tyrkt i Tromsøposten bogtrykkeri ved M. Astad.
RADBRUCH-HALL, D., VARNES, D. & SAVAGE, W. 1976. Gravitational spreading of steep-sided ridges ("sackung") in Western United States. *Bulletin of the International Association of Engineering Geology-Bulletin de l'Association Internationale de Géologie de l'Ingénieur*, 13**,** 23-35.
RAMSEY, C. B. 2009. Bayesian analysis of radiocarbon dates. *Radiocarbon*, 51**,** 337-360.
RASMUSSEN, E. 2011. *Fjellskred i Laksvatnfjellet, Balsfjord, Troms: indre struktur, morfologi og skredmekanismer.* Thesis from UiT The Arctic University of Norway.
REIMER, P. J., BARD, E., BAYLISS, A., BECK, J. W., BLACKWELL, P. G., RAMSEY, C. B., BUCK, C. E., CHENG, H., EDWARDS, R. L. & FRIEDRICH, M. 2013. IntCal13 and Marine13 radiocarbon age calibration curves 0–50,000 years cal BP. *Radiocarbon*, 55**,** 1869-1887.
REUSCH, H. 1894. Strandflaten, et nytt træck i Norges geografi: Norges Geologiske Undersøkelser, v. 14. Norwegian.
ROBERTS, D. & LIPPARD, S. J. 2005. Inferred Mesozoic faulting in Finnmark: current status and offshore links. *Geological Survey of Norway (NGU)*, 443.

ROSEN, P. A., HENSLEY, S., JOUGHIN, I. R., LI, F., MADSEN, S. N., RODRIGUEZ, E. & GOLDSTEIN, R. M. 1998. Synthetic aperture radar interferometry. *Proceedings of The IEEE*.

SANDNES, G. H. 2017. *Geomorfologisk og strukturgeologisk undersøking av ustabile skråningar og skredavsettingar. Regional analyse av fjellområdet mellom Tromsøysundet og Ullsfjorden-Troms, Norge.* Thesis from UiT The Arctic University of Norway.

SCHEIDEGGER, A. E. 1973. On the prediction of the reach and velocity of catastrophic landslides. *Rock Mechanics and Rock Engineering,* 5**,** 231-236.

SIKVELAND, G. 2019. *A structural, geomorphological and InSAR study of the unstable rock slopes at Mellomfjellet, Nordreisa.* Thesis from UiT The Arctic University of Norway.

SKREDE, I. 2013. *Jettan, Nordnesfjellet, Kåfjord, Troms–indre geometri og struktur, kinematikk og styrande faktorar av eit ustabilt fjellparti, basert på strukturellanalyse, geomorfologi og overvakingsdata.* Thesis from UiT The Arctic University of Norway.

SVENDSEN, J. I. & MANGERUD, J. 1987. Late Weichselian and Holocene sea‐level history for a cross‐section of western Norway. *Journal of Quaternary Science,* 2**,** 113-132.

TEAM, R. C. 2017. R Core Team (2017). R: A language and environment for statistical computing. *R Found. Stat. Comput. Vienna, Austria. URL http://www. R-project. org/., page R Foundation for Statistical Computing*.

TRØNNES, L. 2019. *Structural assessment and characterisation of the rock slope failure at Skredkallen, Vannøya. Structural analysis using field and desktop methods.* Thesis from UiT The Arctic University of Norway.

VARNES, D., RADBRUCH-HALL, D., VARNES, K., SMITH, W. & SAVAGE, W. 1990. Measurement of ridge-spreading movements (Sackungen) at Bald Eagle Mountain, Lake County, Colorado, 1975-1989. Dept. of the Interior, US Geological Survey.

VIK, B. K. F. 2019. *Structural assessment and characterization of the unstable rock slopes at Mellomfjellet, Nordreisa.* Thesis from UiT The Arctic University of Norway.

WYLLIE, D. C. & MAH, C. 2004. Rock slope engineering: civil and mining. *Spon Press, New York*.

WYLLIE, D. C. & MAH, C. 2014. *Rock slope engineering*, CRC Press.

WYRWOLL, K.-H. 1977. Causes of rock-slope failure in a cold area: Labrador-Ungava. *Geological Society of America Reviews in Engineering Geology,* 3**,** 59-67.

YR. 2019. *yr.no* [Online]. Available: https://www.yr.no/ [Accessed 02.05.2019].

ZWAAN, K. 1995. Geology of the West Troms Basement Complex, northern Norway, with emphasis on the Senja Shear Belt: a preliminary account. *Geological Survey of Norway Bulletin,* 427**,** 33-36.

Appendix

Appendix A: InSAR displacement rates

A: Average displacement rates of the different polygons marked on Skredkaillen.

Displacement rates are based on InSAR satellite data from insar.ngu.no.

Area 1

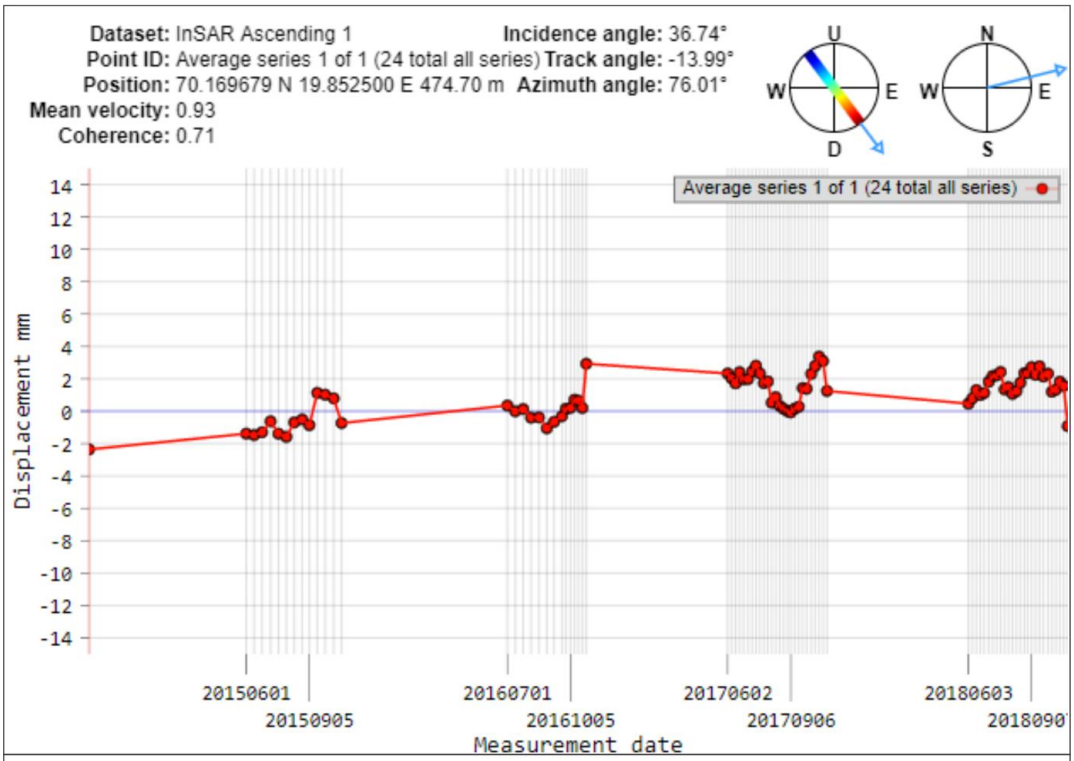

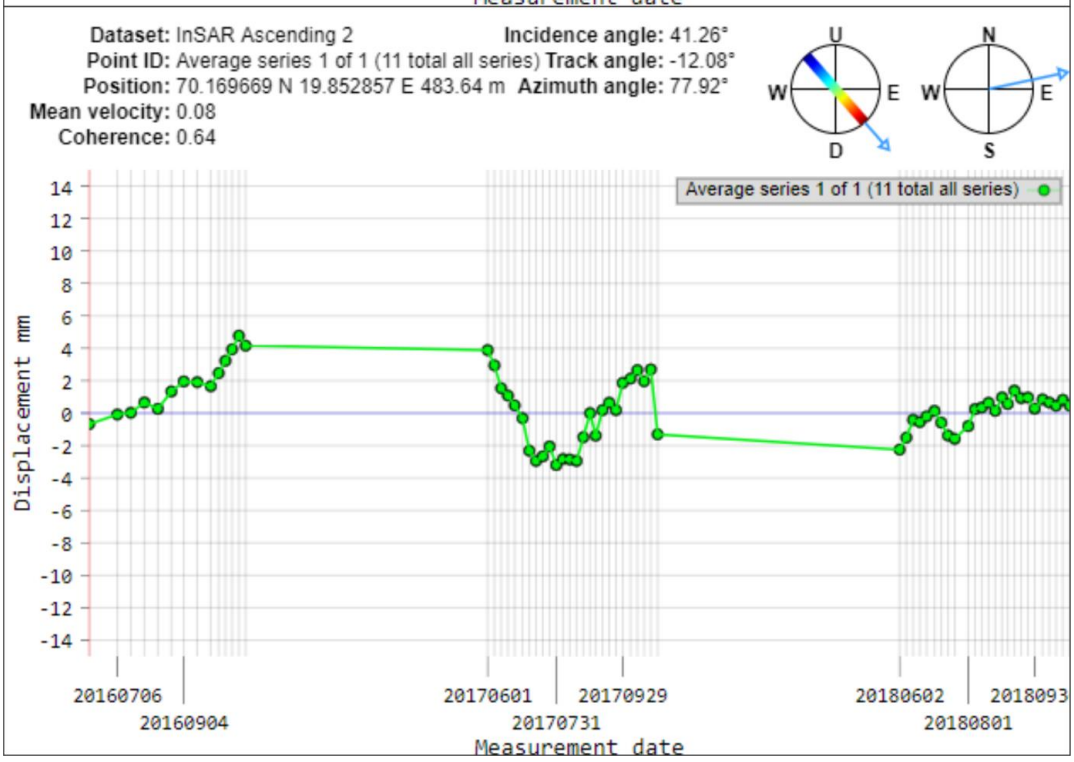

Area 2

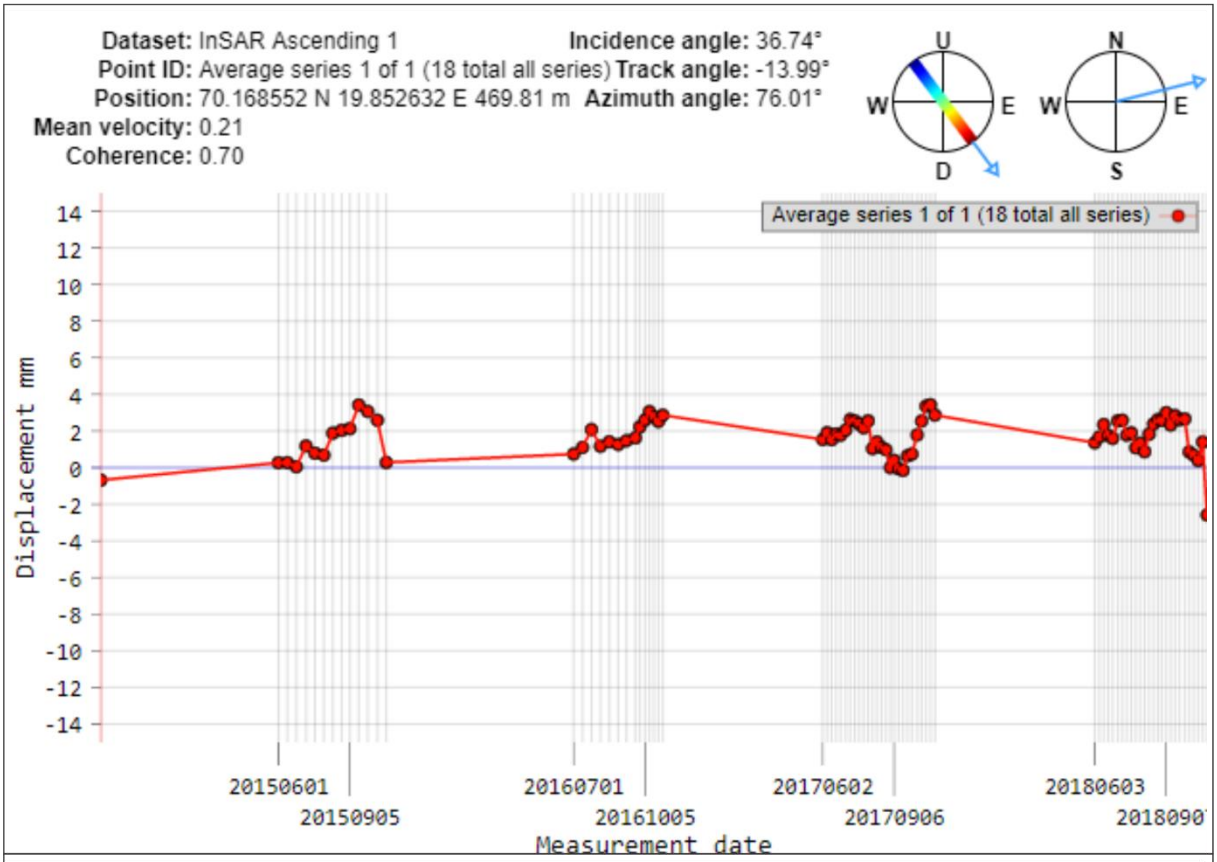
Dataset: InSAR Ascending 1
Incidence angle: 36.74°
Point ID: Average series 1 of 1 (18 total all series)
Track angle: -13.99°
Position: 70.168552 N 19.852632 E 469.81 m
Azimuth angle: 76.01°
Mean velocity: 0.21
Coherence: 0.70
U
W
E
D
N
W
E
S
Average series 1 of 1 (18 total all series)
Displacement mm
14
12
10
8
6
4
2
0
-2
-4
-6
-8
-10
-12
-14
20150601
20150905
20160701
20161005
20170602
20170906
20180603
Measurement date

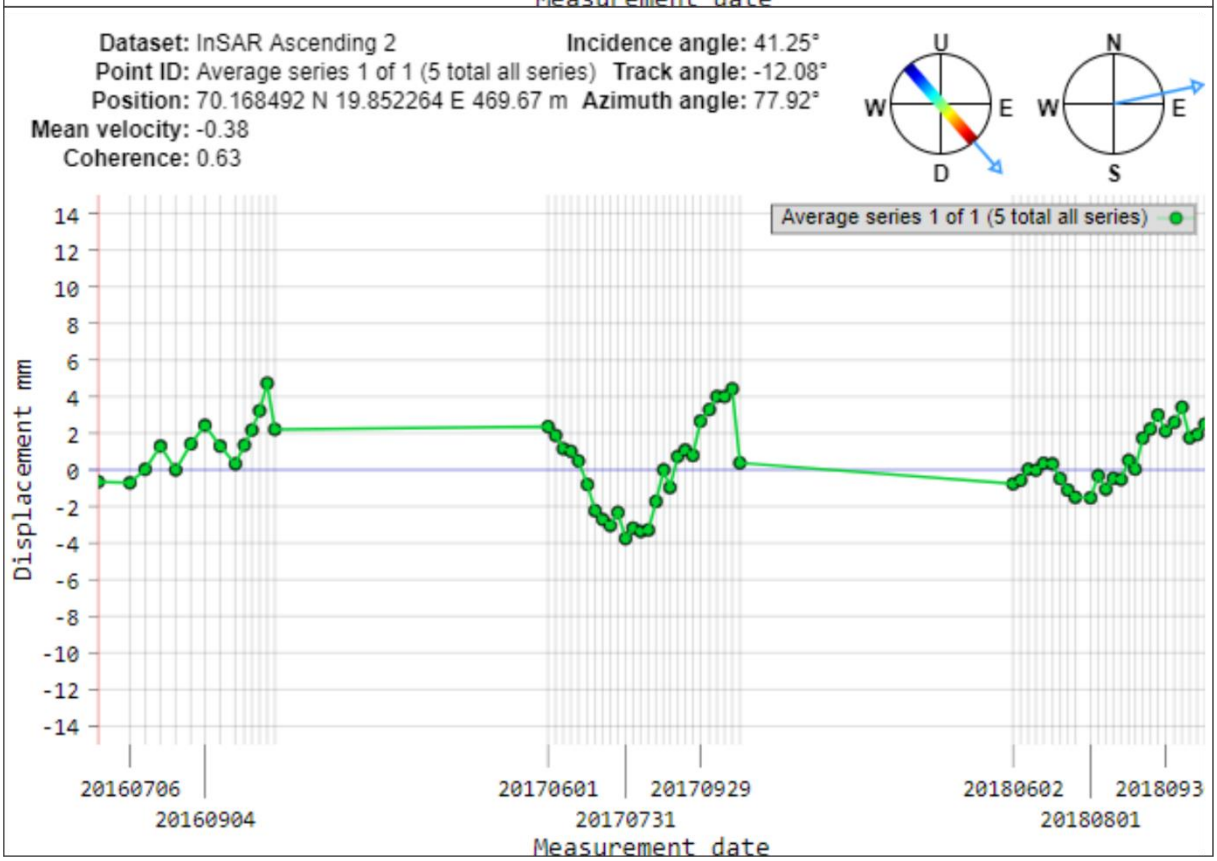
Dataset: InSAR Ascending 2
Incidence angle: 41.25°
Point ID: Average series 1 of 1 (5 total all series)
Track angle: -12.08°
Position: 70.168492 N 19.852264 E 469.67 m
Azimuth angle: 77.92°
Mean velocity: -0.38
Coherence: 0.63
U
W
E
D
N
W
E
S
Average series 1 of 1 (5 total all series)
Displacement mm
14
12
10
8
6
4
2
0
-2
-4
-6
-8
-10
-12
-14
20160706
20160904
20170601
20170731
20170929
20180602
20180801
Measurement date

Area 3

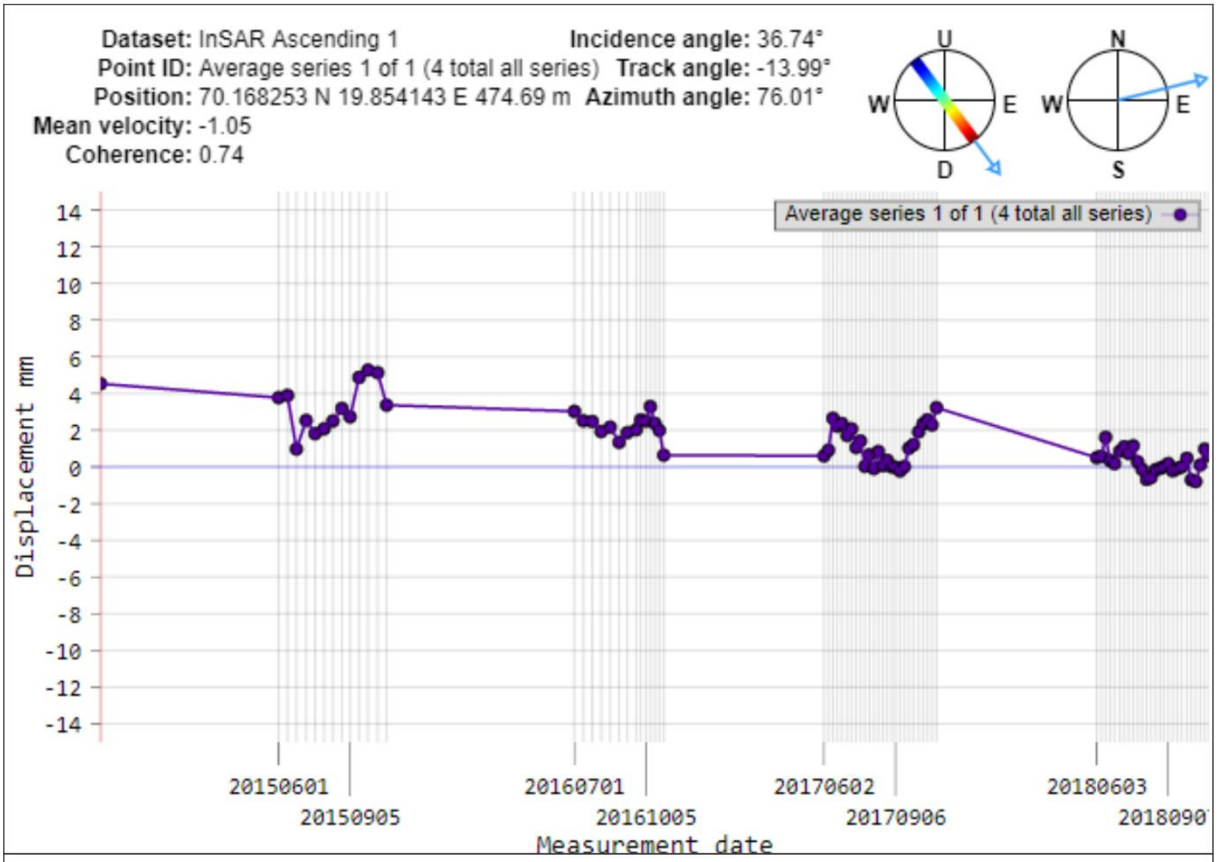
Dataset: InSAR Ascending 1
Incidence angle: 36.74°
Point ID: Average series 1 of 1 (4 total all series)
Track angle: -13.99°
Position: 70.168253 N 19.854143 E 474.69 m
Azimuth angle: 76.01°
Mean velocity: -1.05
Coherence: 0.74
U
W
E
D
N
W
E
S
Average series 1 of 1 (4 total all series)
Displacement mm
14
12
10
8
6
4
2
0
-2
-4
-6
-8
-10
-12
-14
20150601
20150905
20160701
20161005
20170602
20170906
20180603
Measurement date

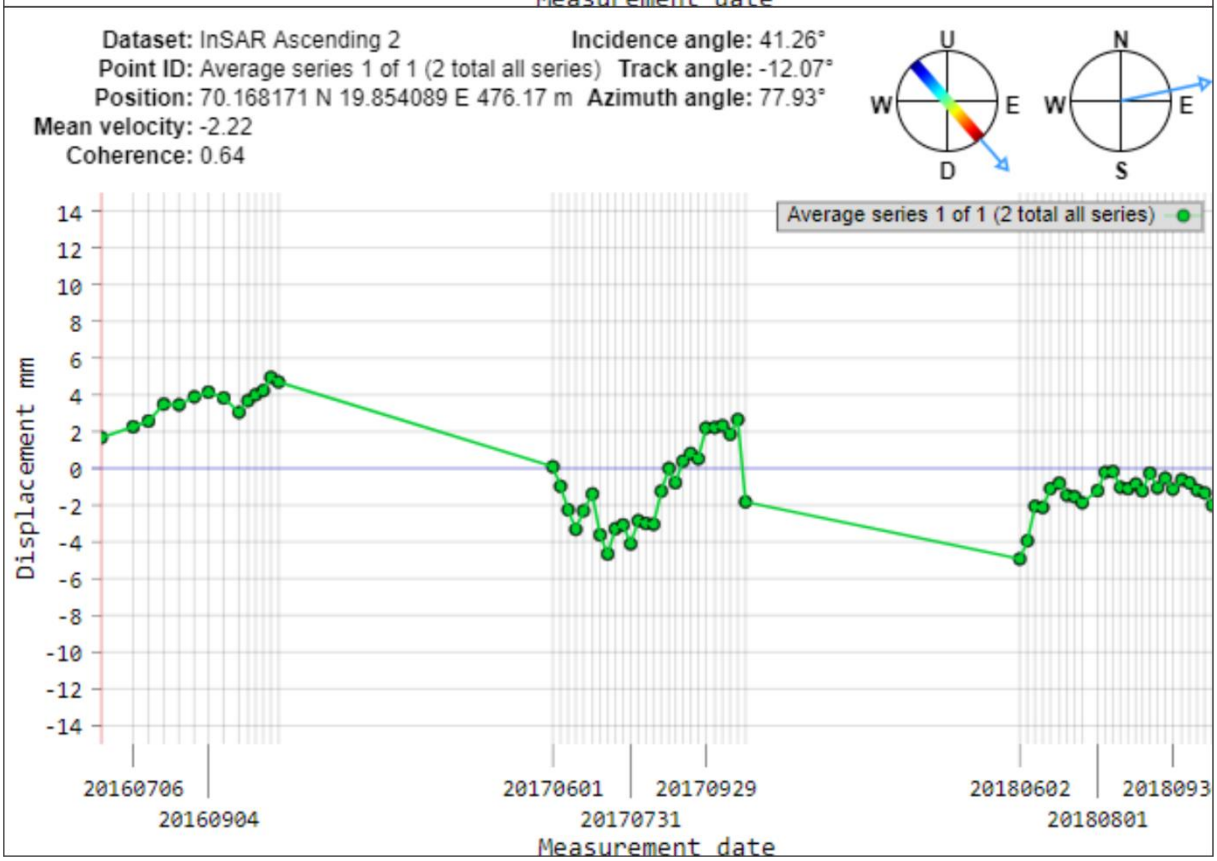
Dataset: InSAR Ascending 2
Incidence angle: 41.26°
Point ID: Average series 1 of 1 (2 total all series)
Track angle: -12.07°
Position: 70.168171 N 19.854089 E 476.17 m
Azimuth angle: 77.93°
Mean velocity: -2.22
Coherence: 0.64
U
W
E
D
N
W
E
S
Average series 1 of 1 (2 total all series)
Displacement mm
14
12
10
8
6
4
2
0
-2
-4
-6
-8
-10
-12
-14
20160706
20160904
20170601
20170731
20170929
20180602
20180801
Measurement date

Area 4

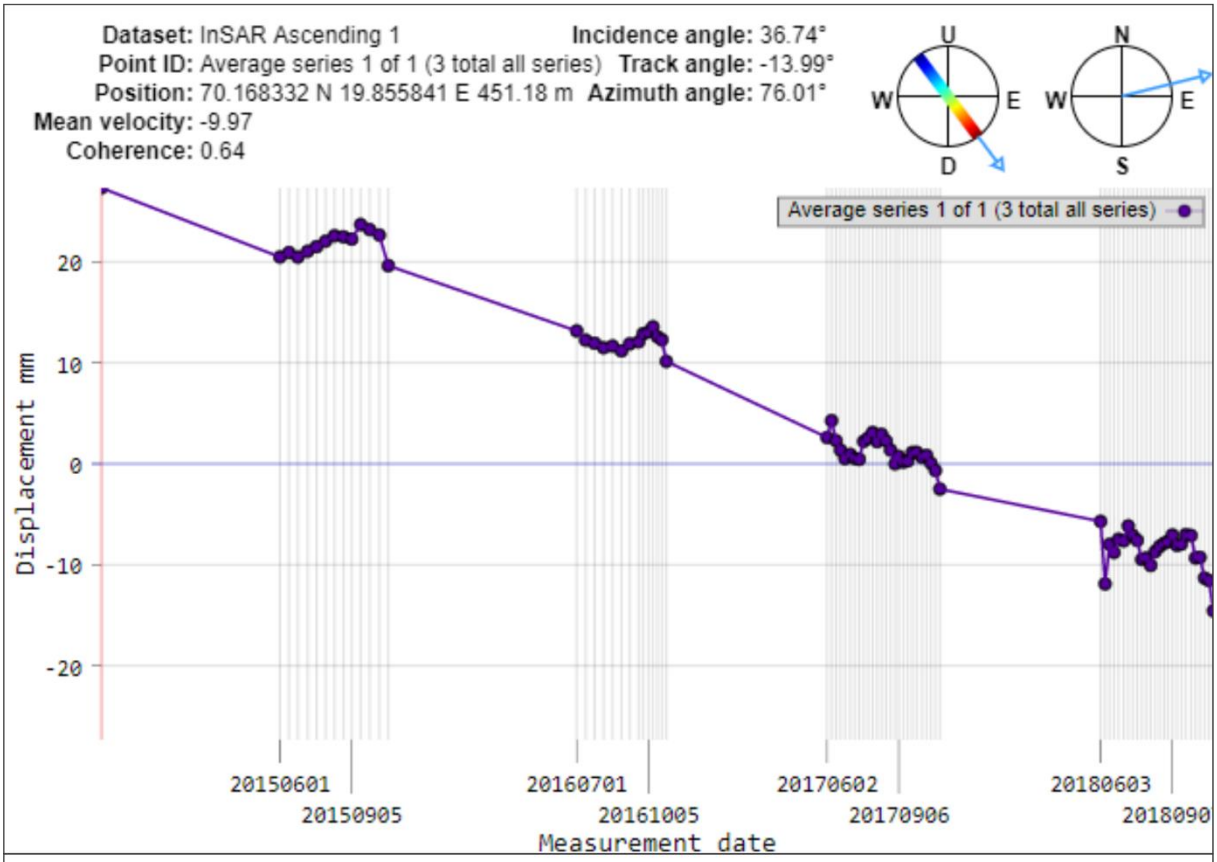
Dataset: InSAR Ascending 1
Incidence angle: 36.74°
Point ID: Average series 1 of 1 (3 total all series)
Track angle: -13.99°
Position: 70.168332 N 19.855841 E 451.18 m
Azimuth angle: 76.01°
Mean velocity: -9.97
Coherence: 0.64
U
W
E
D
N
W
E
S
Average series 1 of 1 (3 total all series)
Displacement mm
20
10
0
-10
-20
20150601
20150905
20160701
20161005
20170602
20170906
20180603
2018090
Measurement date

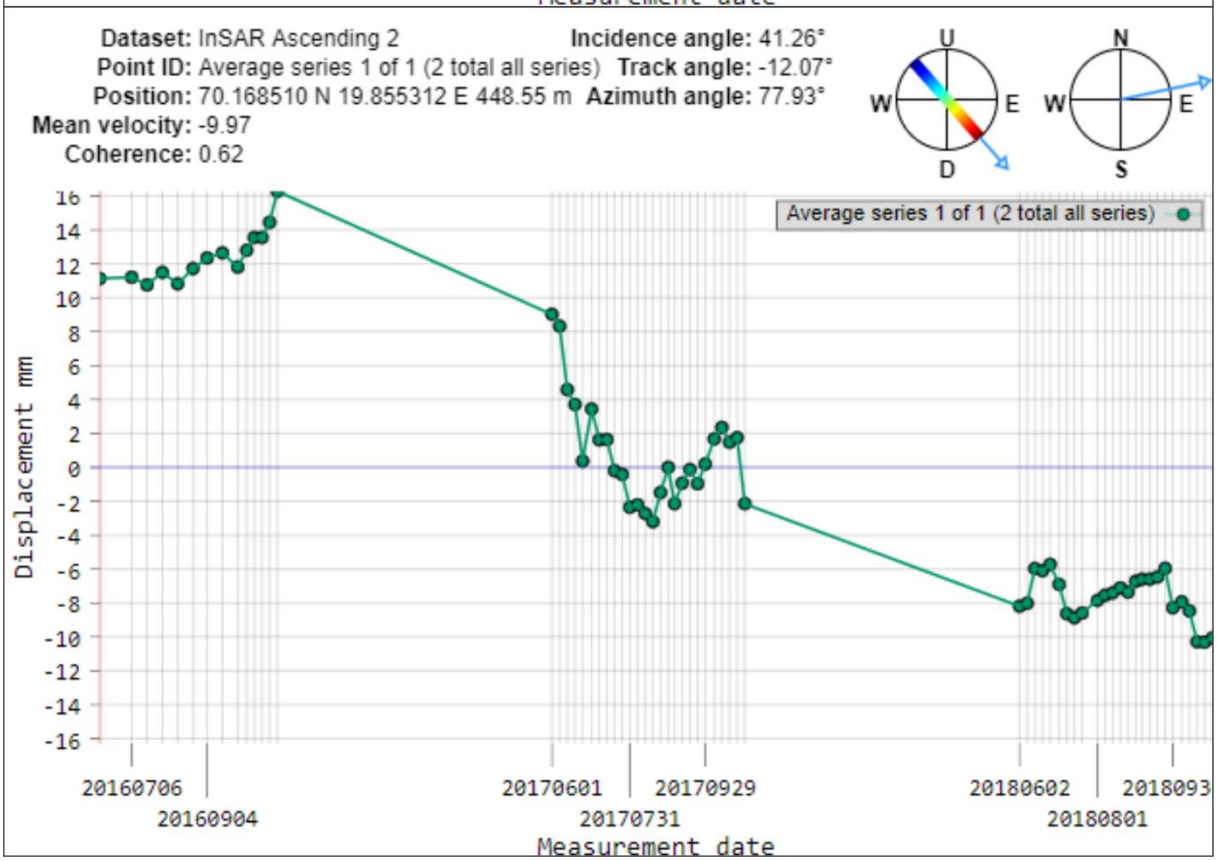
Dataset: InSAR Ascending 2
Incidence angle: 41.26°
Point ID: Average series 1 of 1 (2 total all series)
Track angle: -12.07°
Position: 70.168510 N 19.855312 E 448.55 m
Azimuth angle: 77.93°
Mean velocity: -9.97
Coherence: 0.62
U
W
E
D
N
W
E
S
Average series 1 of 1 (2 total all series)
Displacement mm
16
14
12
10
8
6
4
2
0
-2
-4
-6
-8
-10
-12
-14
-16
20160706
20160904
20170601
20170731
20170929
20180602
20180801
2018093
Measurement date

Area 5

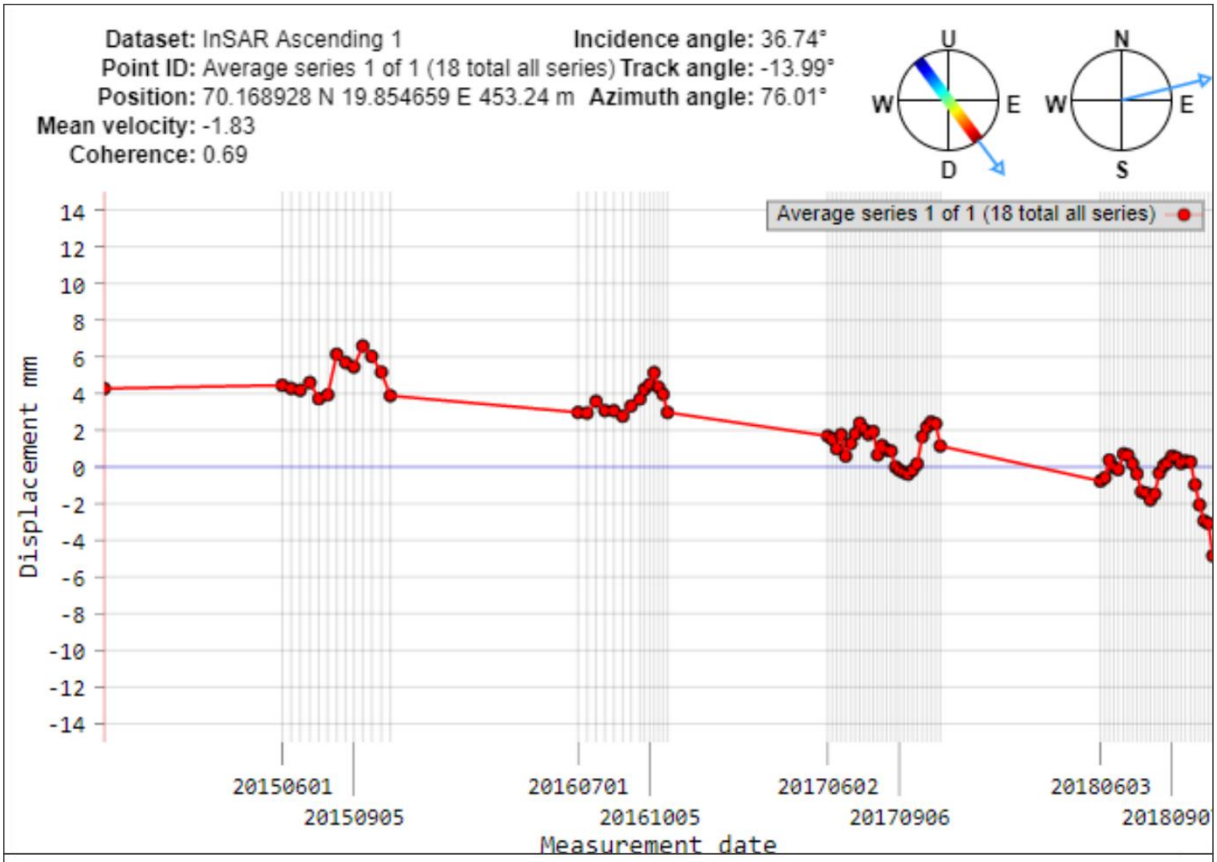
Dataset: InSAR Ascending 1
Incidence angle: 36.74°
Point ID: Average series 1 of 1 (18 total all series)
Track angle: -13.99°
Position: 70.168928 N 19.854659 E 453.24 m
Azimuth angle: 76.01°
Mean velocity: -1.83
Coherence: 0.69
U
W
E
D
N
W
E
S
Average series 1 of 1 (18 total all series)
Displacement mm
14
12
10
8
6
4
2
0
-2
-4
-6
-8
-10
-12
-14
20150601
20150905
20160701
20161005
20170602
20170906
20180603
2018090
Measurement date

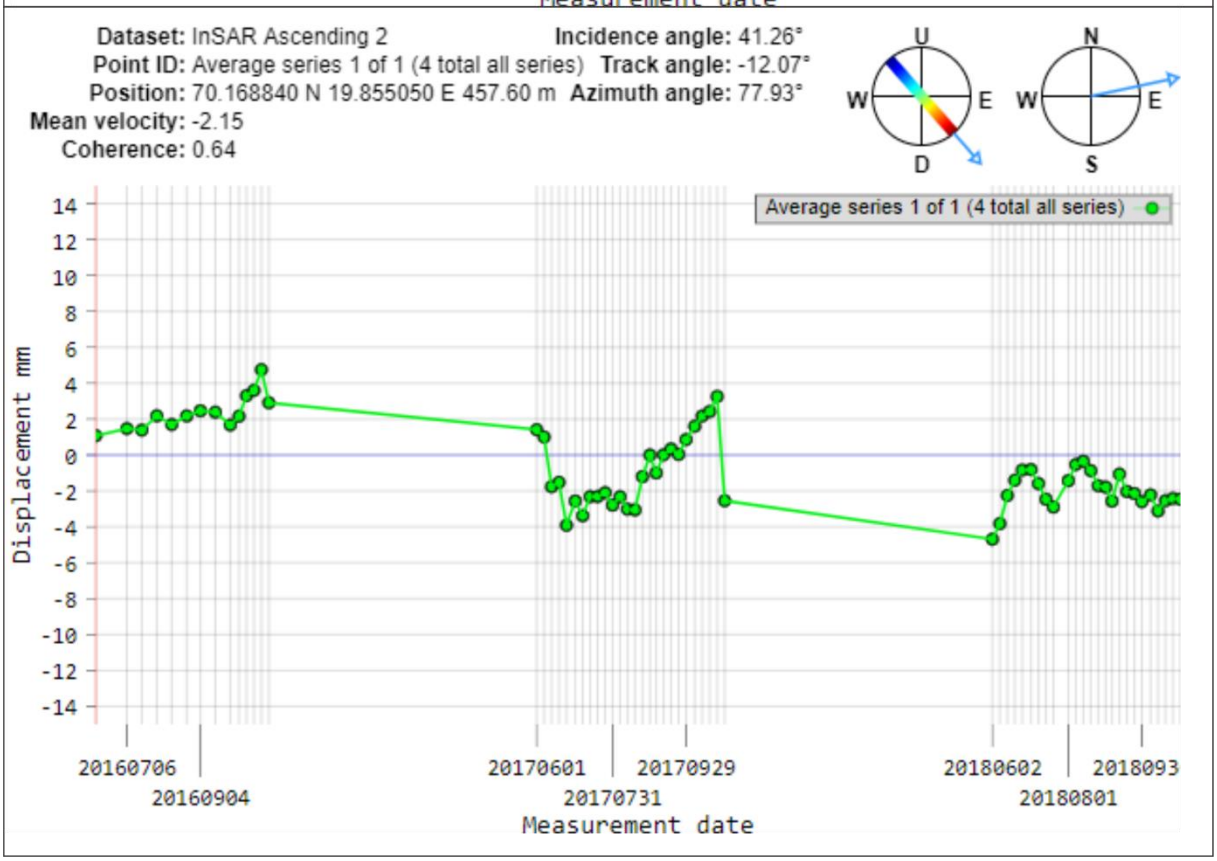
Dataset: InSAR Ascending 2
Incidence angle: 41.26°
Point ID: Average series 1 of 1 (4 total all series)
Track angle: -12.07°
Position: 70.168840 N 19.855050 E 457.60 m
Azimuth angle: 77.93°
Mean velocity: -2.15
Coherence: 0.64
U
W
E
D
N
W
E
S
Average series 1 of 1 (4 total all series)
Displacement mm
14
12
10
8
6
4
2
0
-2
-4
-6
-8
-10
-12
-14
20160706
20160904
20170601
20170731
20170929
20180602
20180801
2018093
Measurement date

Area 6

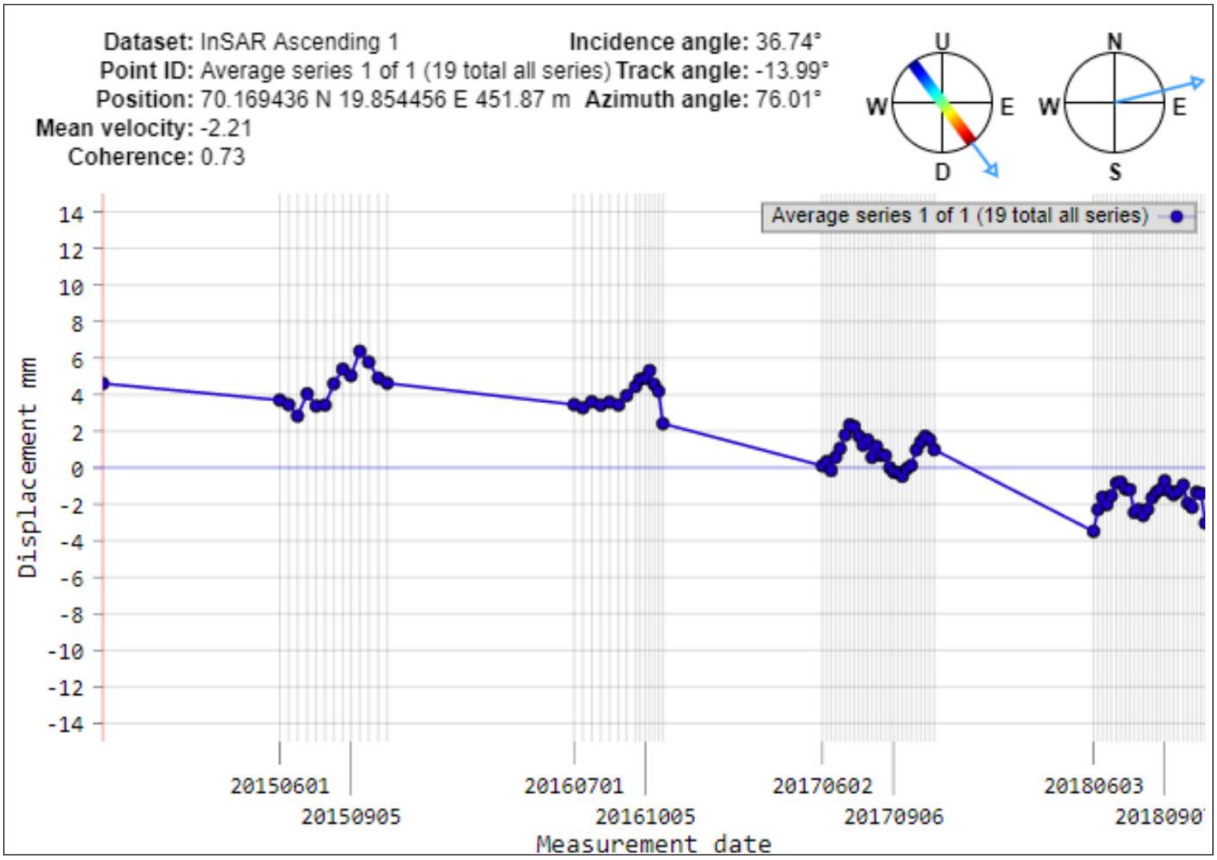
Dataset: InSAR Ascending 1
Point ID: Average series 1 of 1 (19 total all series)
Position: 70.169436 N 19.854456 E 451.87 m
Mean velocity: -2.21
Coherence: 0.73
Incidence angle: 36.74°
Track angle: -13.99°
Azimuth angle: 76.01°
U
W
E
D
N
W
E
S
Average series 1 of 1 (19 total all series)
Displacement mm
14
12
10
8
6
4
2
0
-2
-4
-6
-8
-10
-12
-14
20150601
20150905
20160701
20161005
20170602
20170906
20180603
Measurement date

Area 7

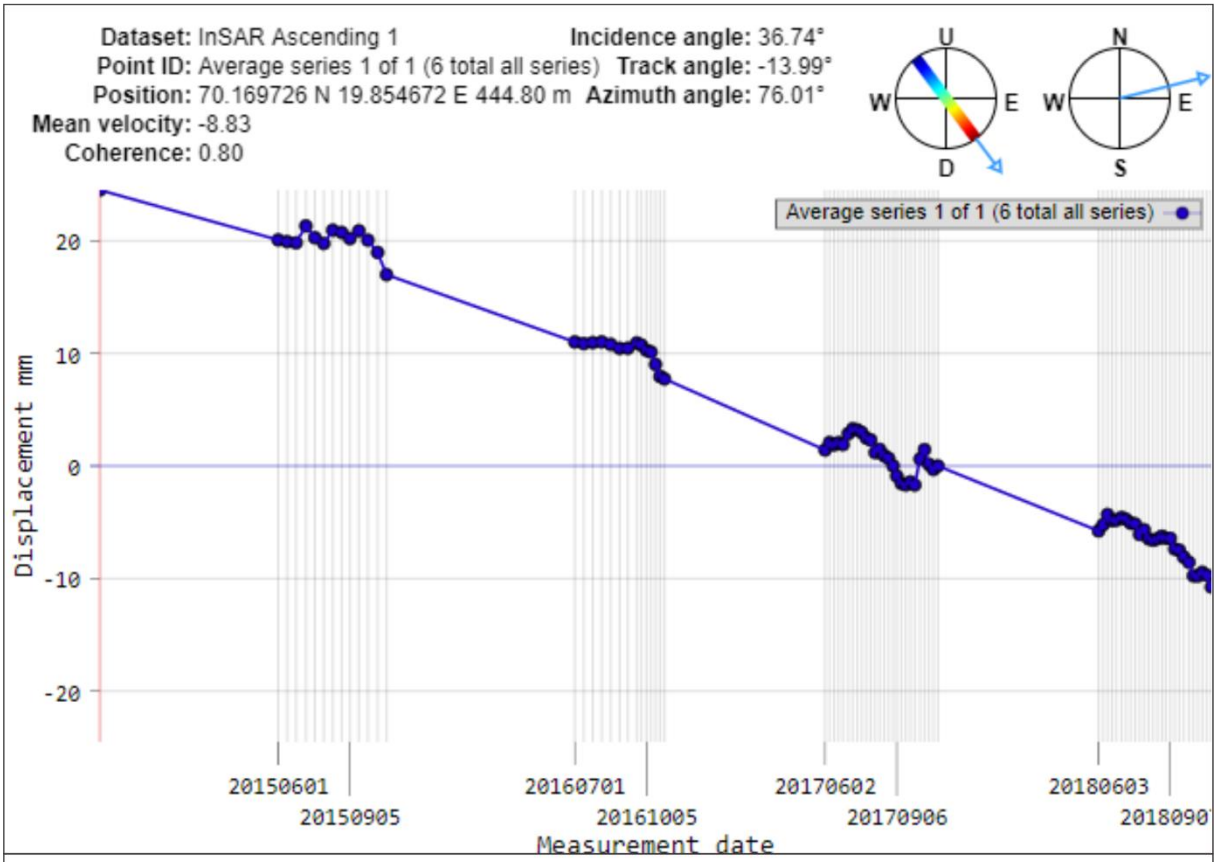
Dataset: InSAR Ascending 1
Incidence angle: 36.74°
Point ID: Average series 1 of 1 (6 total all series)
Track angle: -13.99°
Position: 70.169726 N 19.854672 E 444.80 m
Azimuth angle: 76.01°
Mean velocity: -8.83
Coherence: 0.80
U
W
E
D
N
W
E
S
Average series 1 of 1 (6 total all series)
Displacement mm
20
10
0
-10
-20
20150601
20150905
20160701
20161005
20170602
20170906
20180603
Measurement date

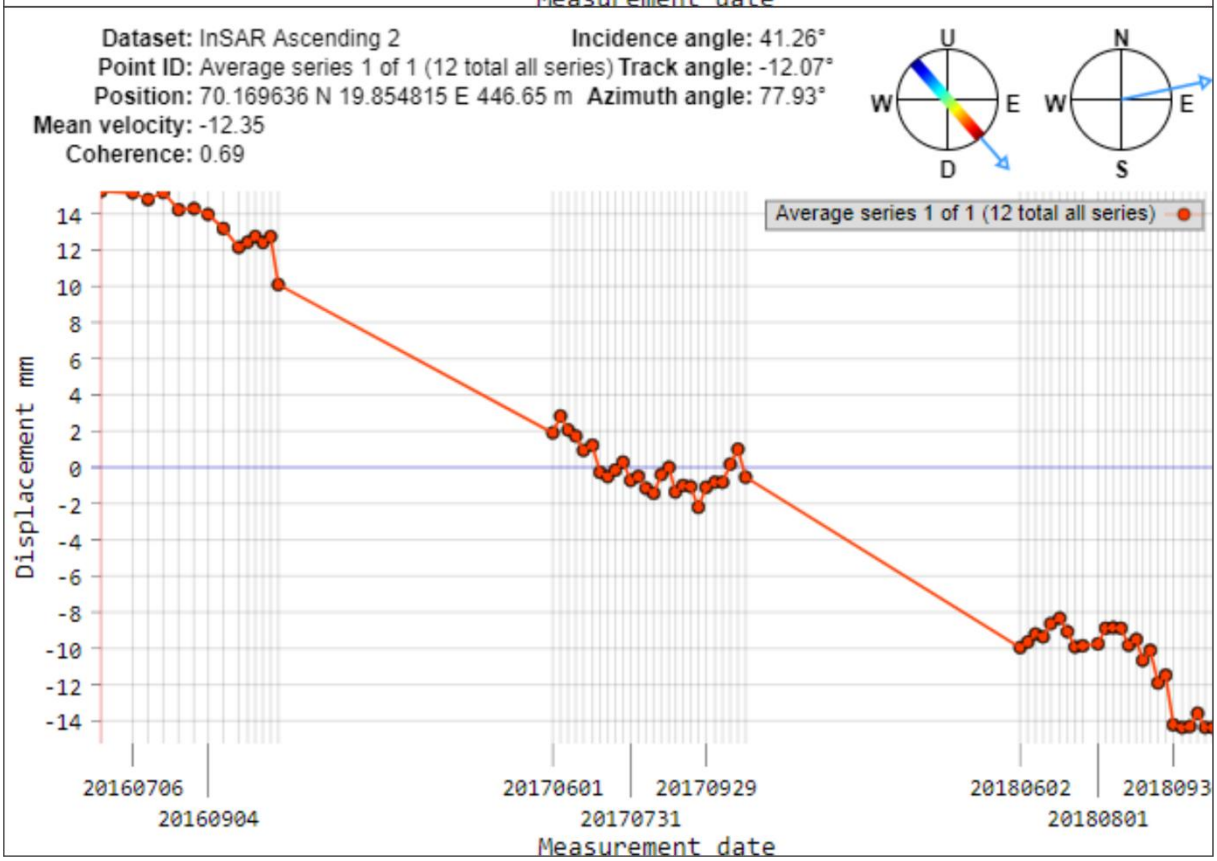
Dataset: InSAR Ascending 2
Incidence angle: 41.26°
Point ID: Average series 1 of 1 (12 total all series)
Track angle: -12.07°
Position: 70.169636 N 19.854815 E 446.65 m
Azimuth angle: 77.93°
Mean velocity: -12.35
Coherence: 0.69
U
W
E
D
N
W
E
S
Average series 1 of 1 (12 total all series)
Displacement mm
14
12
10
8
6
4
2
0
-2
-4
-6
-8
-10
-12
-14
20160706
20160904
20170601
20170731
20170929
20180602
20180801
Measurement date

Appendix B: Field guide sheet

NZ GEOTECHNICAL SOCIETY INC

ROCK > field guide sheet

FIELD DESCRIPTION OF ROCK

SEQUENCE OF TERMS – weathering – colour – fabric – rock name – strength – discontinuities – additional

SCALE OF ROCK MASS WEATHERING

Term	Grade	Abbreviation	Description
Unweathered (fresh rock)	I	UW	Rock mass shows no loss of strength, discolouration or other effects due to weathering. There may be slight discolouration on major rock mass defect surfaces or on clasts.
Slightly Weathered	II	SW	The rock mass is not significantly weaker than when fresh. Rock may be discoloured along defects, some of which may have been opened slightly.
Moderately Weathered	III	MW	The rock mass is significantly weaker than the fresh rock and part of the rock mass may have been changed to a soil. Rock material may be discoloured and defect and clast surfaces will have a greater discolouration, which also penetrates slightly into the rock material. Increase in density of defects due to physical disintegration.
Highly Weathered	IV	HW	Most of the original rock mass strength is lost. Material is discoloured and more than half the mass is changed to a soil by chemical decomposition or disintegration (increase in density of defects/fractures). Decomposition adjacent to defects and at the surface of clasts penetrates deeply into the rock material. Lithorelicts or corestones of unweathered or slightly weathered rock may be present.
Completely Weathered	V	CW	Original rock strength is lost and the rock mass changed to a soil either by decomposition (with some rock fabric preserved) or by physical disintegration.
Residual Soil	VI	RS	Rock is completely changed to a soil with the original fabric destroyed (pedological soil).

ROCK STRENGTH TERMS

Term	Field Identification of Specimen	Unconfined uniaxial compressive strength q_u (MPa)	Point load strength $I_{s(50)}$ (MPa)
Extremely strong	Can only be chipped with geological hammer	> 250	>10
Very strong	Requires many blows of geological hammer to break it	100 – 250	5 – 10
Strong	Requires more than one blow of geological hammer to fracture it	50 – 100	2 – 5
Moderately strong	Cannot be scraped or peeled with a pocket knife. Can be fractured with single firm blow of geological hammer	20 – 50	1 – 2
Weak	Can be peeled by a pocket knife with difficulty. Shallow indentations made by firm blow with point of geological hammer	5 – 20	<1
Very weak	Crumbles under firm blows with point of geological hammer. Can be peeled by a pocket knife	1 – 5	
Extremely weak (soil description required)	Indented by thumb nail or other lesser strength terms used for soils	<1	

Note: • No correlation is implied between q_u and $I_{s(50)}$

SPACING OF DEFECTS/ DISCONTINUITIES

Term	Spacing
Very widely spaced	>2 m
Widely spaced	600 mm – 2 m
Moderately widely spaced	200 mm – 600 mm
Closely spaced	60 mm – 200 mm
Very closely spaced	20 mm – 60 mm
Extremely closely spaced	<20 mm

APERTURE OF DISCONTINUITY SURFACES

Term	Aperture (mm)	Description
Tight	Nil	Closed
Very Narrow	> 0 – 2	
Narrow	2 – 6	
Moderately Narrow	6 – 20	Gapped
Moderately Wide	20 – 60	Open
Wide	60 – 200	
Very Wide	> 200	

BEDDING THICKNESS TERMS

Term	Bed Thickness
Thinly laminated	< 2 mm
Laminated	2 mm - 6 mm
Very thin	6 mm - 20 mm
Thin	20 mm - 60 mm
Moderately thin	60 mm - 200 mm
Moderately thick	0.2 m - 0.6 m
Thick	0.6 m - 2 m
Very thick	> 2 m

BEDDING INCLINATION TERMS

Term	Inclination (from horizontal)
Sub-horizontal	0° – 5°
Gently inclined	6° – 15°
Moderately inclined	16° – 30°
Steeply inclined	31° – 60°
Very steeply inclined	61° – 80°
Sub-vertical	81° – 90°

ROUGHNESS AND APERTURE

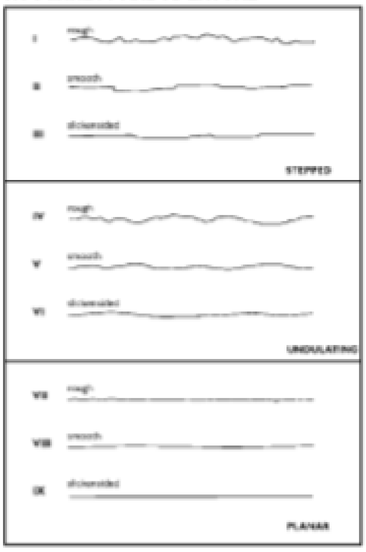

compiled by KATE WILLIAMS design KARRYN MUSCHAMP

NZ GEOTECHNICAL SOCIETY INC

This field sheet has been taken from and should be used and read with reference to the document FIELD DESCRIPTION OF SOIL AND ROCK. Guideline For the Field Classification and Description of Soil and Rock for Engineering Purposes. NZ Geotechnical Society Inc, December 2005. **www.nzgeotechsoc.org.nz**